THE DESIGN AND CONSTRUCTION OF A HOLOGRAPHIC FILM MEASURING MACHINE FOR THE HEAVY-LIQUID BUBBLE CHAMBER HOBC AND A DETERMINATION OF THE CROSS SECTION FOR CHARM PRODUCTION BY 360 GEV PROTONS

A thesis presented for the degree of Doctor of Philosophy
in the University of London

October 1984

Peter Robert Hobson

Department of Physics and Astronomy
University College London

O'er many a frozen, many a fiery alp,
Rocks, caves, lakes, bogs, dens, and shades of death,
A universe of death, which God by curse
Created evil, for evil only good,
Where all life dies, death lives, and nature breeds,
Perverse, all monstrous, all prodigious things,
Abominable inutterable, and worse
Than Fables yet have feigned, or fear conceived,
Gorgons and Hydras and Chimeras dire.

Milton J. Paradise Lost, Book II

ABSTRACT

A heavy-liquid, rapid cycling bubble chamber, using in-line holography, with a typical bubble diameter of 10 microns, has been used to measure the total cross-section for charm particle production by 360 GeV/c protons.

The experiment NA25 in the H2 beam line at CERN, comprising the bubble chamber HOBC and an associated muon detector, is described. The operating conditions of the chamber, the holographic recording system, and the multiplicity and muon triggers are discussed.

The theory of holographic recording and replay is considered in detail. The effects on the recorded image of laser coherence, the limitations of real film and the object structure are discussed, as are the aberrations of the reconstructed image. The effects of spatial filtering on the observed image are considered.

The design and construction of a computer controlled film scanning machine "CHIMAERA" is described. The design principles are outlined, the mechanical stages and their controlling microcomputer are discussed. Particular emphasis is placed on the design of the optical system and the choice of video camera tubes.

The software, running in a PDP 11/44 minicomputer, providing the guidance and data acquisition for CHIMAERA is described in detail and the software driving the stages, running in an 8085 microprocessor, is briefly mentioned.

The analysis of the data from film exposed with 360 GeV/c protons is presented. The backgrounds in each topology are considered, and the effects of the cuts which were made to enhance the signal to background ratio are decribed. The scanning efficiency and decay visibilities

are calculated. Finally the charm production cross-section is evaluated.

CONTENTS

CORRIGENDA

Page	Line			
44	16	moun	Change To	muon
59	27	relay	Change To	replay
65	9	asssuming	Change To	assuming
67	14	arrising	Change To	arising
67	27	RAL (1981)	Change To	Sekulin (1981)
82	2	activted	Change To	activated
83	29	greater	Change To	smaller
84	18	arrising	Change To	arising
91	31	allignment	Change To	alignment
122	28	elliminate	Change To	eliminate
127	4	unifrom	Change To	uniform
134	32	dissapear	Change To	disappear
139	11	paricle	Change To	particle
156	22	loose	Change To	lose
157	16	$\overline{V} = 0.618$	Change To	$V\infty \times \overline{V} = 0.618$
168	13	simlple	Change To	simple

LIST OF FIGURES

LIST OF TABLES

INTRODUCTION

The study of heavy flavour production is more amenable to theoretical calculation than the production of light flavours because of the large mass of the c-quark. Various theoretical models give very different predictions for the charm production cross sections. Both the magnitude and the energy dependence are strongly dependent on the mechanisms involved. Therefore it was of considerable interest to measure in the same experimental apparatus the charm production cross section at different energies.

The observation of charmed particle production in hadron-hadron interactions is difficult if purely electronic techniques are used. This is due to the small cross section, the large number of decay modes and a large combinatorial background. Particles with the quantum numbers charm or beauty have proper lifetimes of the order of 10^{-13} s. Even at high energies these particles travel only a few millimetres in the laboratory before decaying. In a conventional bubble chamber, with bubble diameters of around 300 microns, such tracks would not be seen. To record 10 micron bubbles using conventional photography presents a serious problem. The depth of field becomes very small at such resolutions, considerably less than the interaction volume. The NA25 collaboration (Bari-BrusselsCERN-Mons-Paris-Strasbourg-UCL-Vienna) solved this problem by designing a rapid-cycling heavy-liquid bubble chamber (HOBC) that used in-line holography to record the interactions. The camera was triggered by a downstream muon detector resulting in a considerable enrichment of the charm content of the holograms.

The NA25 experiment recorded 40000 in-line holograms at incident hadron energies of 360 GeV and 200 GeV. The analysis of these holograms required the design and construction of new film scanning machines. This thesis describes the design of the "CHIMAERA" (Computerised Holographic Image Measuring And Event Reconstruction Apparatus) film scanning and measuring machine at UCL.

CHAPTER 1 THEORY OF CHARM PRODUCTION AND DECAY

1.1 Strong Production of Charm

The processes considered below all relate to the process p + N --> C + $\overline{C}$ + anything, where N is a nucleon. There are five major models of charmed particle production in the strong interaction. Two recent reviews (Bellini (1984), Kernan (1984)) discuss most of the material presented in sections 1.1.1 to 1.5.1 .

1.1.1 Phenomenological Approach of Bourquin and Gaillard

Bourquin and Gaillard (1975) proposed the following empirical model for non-leading production of π ,p, ω and ψ in p-p collisions:

$$\text{E 101} \qquad \frac{Ed^3\sigma}{d^3p_T} = \frac{A}{(E_T+2.7)^{16.5}} f(y) \exp[-\frac{25p_T}{\sqrt{s}}]$$

where y is the rapidity and $E_T \cong \sqrt{(p_T{}^2 + M^2)}$, E_T is in GeV, p_T in GeV/c and A is a normalisation constant.

They found that this parameterisation fitted the data better than one using the variables x_F and p_T .

This model was later extended (Bourquin and Gaillard (1976)) to include particles produced in pairs. They assumed that due to local conservation of quantum numbers, particle pairs such as D D come from the decay R --> D $\overline{D}$ of a "single" particle R with a mass about 100 MeV/c² greater than the combined pair mass. The three main features of this model were:

1) Predominantly central production with a constant $\frac{d\sigma}{dy}$ for low y

2) The total $D\bar{D}$ cross section rises by a factor of 2.5 over the centre of mass energy range 27 - 63 GeV

3) The $D\bar{D}$ have a low relative momentum in their centre of mass system, implying a close correlation between the two particles.

1.1.2 Central Production Models

Combridge (1979) considered the following lowest order QCD processes (Fig.1.1):

Fusion, $qq \to c\bar{c}$, $gg \to c\bar{c}$
Flavour Excitation, $qc \to qc$, $gc \to gc$

central production is expected to lead to a value of 5 in the exponent of (1-x) in the inclusive cross section (Halzen (1982):

$$\text{E 102} \qquad \frac{d^3\sigma}{dx_F\,dp_T^2} \simeq (1-x_F)^5 \exp(-bp_T^2)$$

The fusion model only populates the region $x_F \simeq 0$ with charm. The main features of this model are:

1) The charm production cross section is predicted to rise by a factor of 10 to a value around 100 microbarns over the centre of mass energy range 20 - 60 GeV.

2) The flavour excitation cross sections are typically one order of magnitude lower than those for flavour creation (fusion).

3) Production is central

4) Gluon processes dominate at large values of $\sqrt{s}$

1.1.3 Forward Production

Barger, Halzen, and Keung (1979) suggested that forward produced charm could be explained as a flavour excitation process, provided that the QCD evolved charm distribution had a hard Feynman x dependence. Forward Λ_c^+ production then occurs through the combination of a spectator charm quark with two valence quarks. The Λ_c^+ is assumed to carry off all of the momentum of the struck quark in the nucleon. This process is shown in Fig.1.2 . The model has the following predictions:

1) Λ_c^+ production will have the same nuclear dependence as central production; that is the exponent α in A^{α} should equal 1. A non-perturbative or true diffractive model suggests that α =0.67, this factor arises from the dependence of the nuclear radius on $\sqrt{A}$, and thus the area on $A^{0.67}$.

2) At centre of mass energies of 500 GeV the proportion of diffractive production is higher for heavy (top etc.) quarks than for bottom or charm, due to the domination of the diffractive component at low energies.

Barger et al(1979) emphasise that their cross section estimates are strongly dependent on the value chosen for t, the minimum momentum transfer in the process qc -> qc , gc -> gc. They chose a value $t \geq -m_c$ with m_c = 1.5 GeV/c²

Odorico (1981) followed Barger et al(1979) but with more rigour. The principal additions were:

1) A QCD Monte Carlo calculation was used to estimate the charm sea distribution

2) Set $Q^2 = -t(\text{min}) = 0.25m_c$ with m_c = 1.5 GeV/c² This was obtained from measured momentum distribution of D mesons

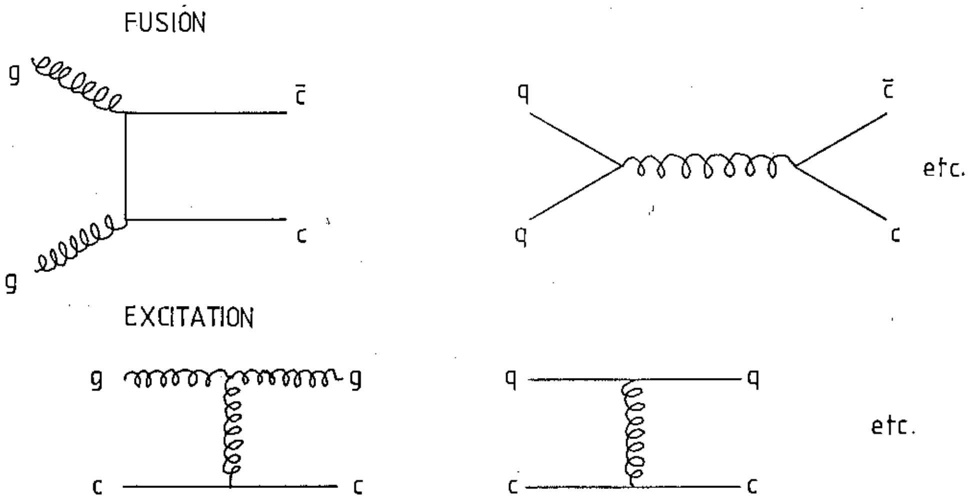

Figure 1.1 Central Production QCD Processes

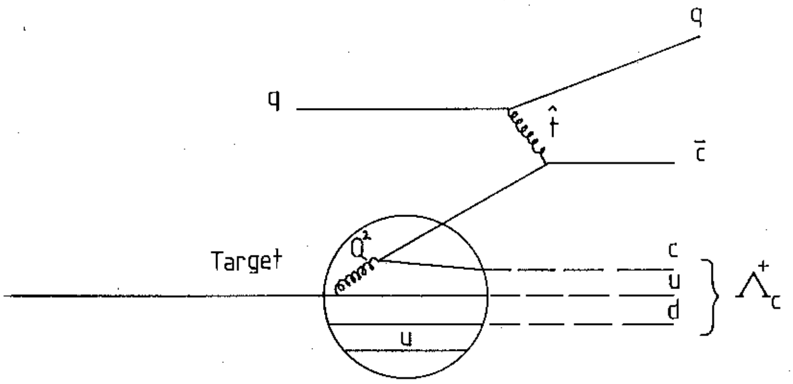

Figure 1.2 Forward Λ_c^+ Production

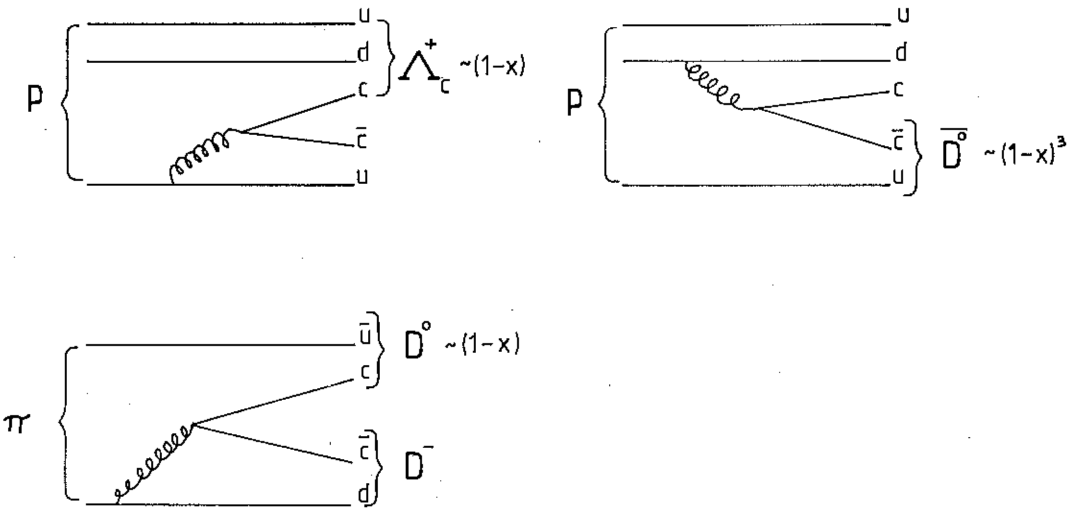

Figure 1.3 Diffractive Charmed Particle Production

3) A recombination Monte Carlo was used to generate the x distribution for Λ_c^+ and $\overline{D}$ particles

This predicts that at $\sqrt{s}$ 540 GeV, fast baryons will be generated almost exclusively by the spectator quark, at 62 GeV the struck c-quark is dominant.

1.1.4 Intrinsic Charm Model

This model, due to Brodsky et al.(1981), postulates the existance of Fock states in the proton containing intrinsic charm, for example $|uudc\bar{c}\rangle$. It was suggested that these might exist at around the 1% level. By intrinsic it was meant that such states are present in the proton independently of any external interaction, as opposed to extrinsic c-quarks which are generated in association with a large transverse momentum reaction by standard bremsstrahlung and qq pair production processes. The predictions of this model were:

1) For the production of heavy quarks on nuclear targets one expects an A dependence with an exponent α =0.67, this is in contrast to perturbative QCD hard-scattering cross sections which predict a value of α =1

2) Fast Λ_c^+ production is predicted

3) The probability for a hadron to contain an intrinsic heavy quark pair $Q\overline{Q}$ varies as $1/M^2_{Q\overline{Q}}$

1.1.5 Large Feynman x Counting rules

The study of fast particle fragmentation in perturbative QCD leads to "counting rules" which were first derived by Blankenbeckler (1974) and Gunion (1979). These rules are applicable to particles produced at large Feynman

x. The inclusive production cross section given in E102 contains an integer (in theory) exponent, n, in the factor (1-x). Gunion (1979) showed how n could be derived from a consideration of the spectator quarks. Summarising his paper, one can divide the spectator quarks into those arising from the hadron Fock state (n_H in number), and those participating in the point-like pair creation process (n_P in number). The value of the exponent n is given by:

E103 $$n = 2\times n_H + n_P - 1$$

The fast sea quark, created in a point-like manner, does not interact with the other components of the proton and the bound state momentum is not redistributed. Figure 1.3 illustrates this diffractive process for baryons and mesons. The meson is predicted to have a softer Feynman x distribution as it contains one and not two valence quarks from the proton.

1.2 Decays of Charmed Mesons and Baryons

The decays of charmed particles can be conveniently divided into two groups; those containing a lepton and those decays which are purely hadronic. The purely leptonic decays are highly suppressed, and will not be considered in detail here. The decays can also be split into two subgroups according to the mechanisms involved.

The simplest scheme is the spectator model in which the non-charmed quark plays no role in the decay. in this model the lifetimes of all the charmed mesons and baryons with one c-quark are predicited to be more or less equal. Spectator model decays of mesons are shown in Fig.1.4. In this model an estimate of the lifetime of a charmed meson can be obtained by comparing the processes in Fig.1.5. If the assumptions of the spectator model are correct, then the total decay width to electrons can be estimated naively

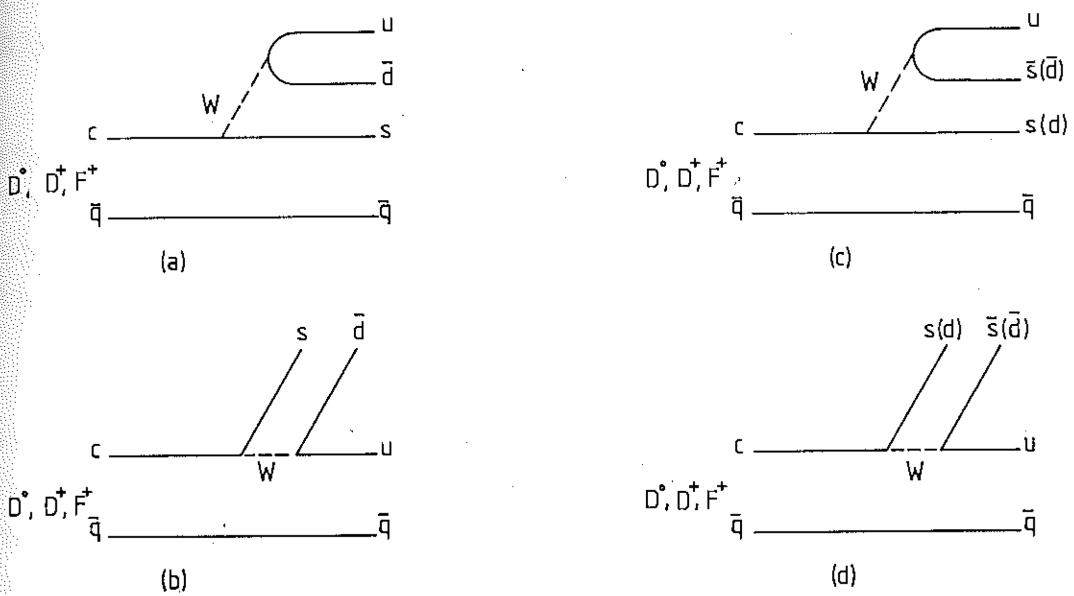

Figure 1.4 Spectator Model Decays of Charmed Mesons

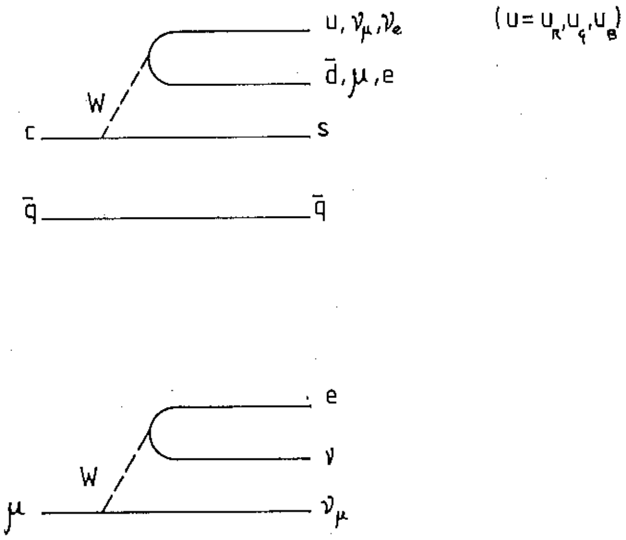

Figure 1.5 Comparison of Charmed Meson and Muon Decay

to be given by:

E104 $$\Gamma(e) = 5\left(\frac{m_c}{m_\mu}\right)^5\Gamma(\mu \to e\nu\bar{\nu})$$

where the factor 5 arises from the three colours plus two leptons into which the W can decay. Taking the mass of the c-quark (m_c) to be about half of the mass of the $\psi(3770)$, the estimated D^+ lifetime (Kalmus (1982)) is 3.5×10^{-13} s.

In the non-spectator model W-exchange and W-annihilation diagrams are also allowed. There is no non-spectator model diagram for the D^+ decay because there is no W-exchange process for the $(c\bar{d})$ quark combination. Thus the ratio of D^+ to D^0 lifetime is a measure of the relative strengths of the spectator and non-spectator amplitudes.

1.2.1 Cabbibo-Allowed and Cabbibo-Suppressed Decays

The doublet partner of the c-quark is an eigen-quark of weak isospin, and is a mixture of s and d quarks (the eigen-quarks of the strong interaction), with a mixing angle (θ_c). Thus:

E105 $$s_\theta = s.\cos(\theta_c) - d.\sin(\theta_c)$$

where θ is the Cabbibo angle $\simeq 0.23$ radians.

The $\cos(\theta_c)$ amplitude can be referred to as Cabbibo-allowed, and the $\sin(\theta_c)$ amplitude as Cabbibo-suppressed. The relative rates will differ by a ratio $\tan^2(\theta_c) \simeq 0.05$. The hadronic selection rules for these two processes are:

E106 Cabbibo-allowed $c \to s$
$$\Delta Q = -\Delta S = \Delta C \; ; \; \Delta I = 0$$

Cabbibo-suppressed $c \rightarrow d$
$\Delta Q = \Delta C$; $\Delta S = 0$; $\Delta I = 1/2$

Thus the dominant decay product of charmed particles are strange particles.

1.2.2 Semi-leptonic Decays

Figure 1.6 illustrates the semi-leptonic decays of the D and F mesons. Gaillard et al.(1975) give estimates of the inclusive semi-leptonic branching ratio. They viewed semi-leptonic decays as the process $c \rightarrow s + l^{+} + \nu$ and $c \rightarrow d + l^{+} + \nu$ followed by de-excitation. Summing over all possible final states the semi-leptonic rate should be essentially that of the elementary process, if the mass of the c-quark is large enough to allow the resulting hadronic state to decay entirely to hadrons. If this is true then in an analogy to muon decay (Bjorken and Drell (1964) section 10.13):

E107 $\Gamma\ (c \rightarrow l^{+} + \nu + \text{hadrons}) = G_F^2 m_c^5 192\pi^3$

A similar estimate was made for purely hadronic decays:

E108 $\Gamma\ (c \rightarrow \text{hadrons}) = (G_F A\cos^2(\theta_c))^2 m_c^5 192\pi^3$

where A is an enhancement factor resulting from the mesonic width, such that $A\cos(\theta_c)\sin(\theta_c) \simeq 1$

Combining E107 and E108 a crude estimate for the semi-leptonic branching ratio is found:

E109 $$\frac{\Gamma\ (c \rightarrow l^{+} + \nu + \text{hadrons})}{\Gamma\ (c \rightarrow \text{hadrons})} \simeq \tan^2(\theta_c)$$

which is around 5% of the total branching ratio. Gaillard et al.(1975) also discuss the totally leptonic decay rate, assuming a close analogy with kaon decay and that SU(4) is

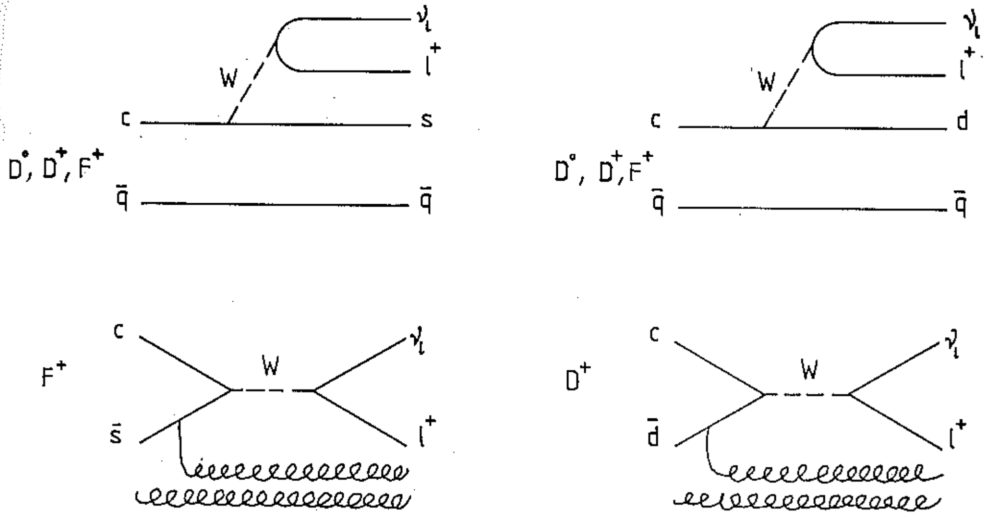

Figure 1.6 Semi-leptonic Decays of D and F Mesons

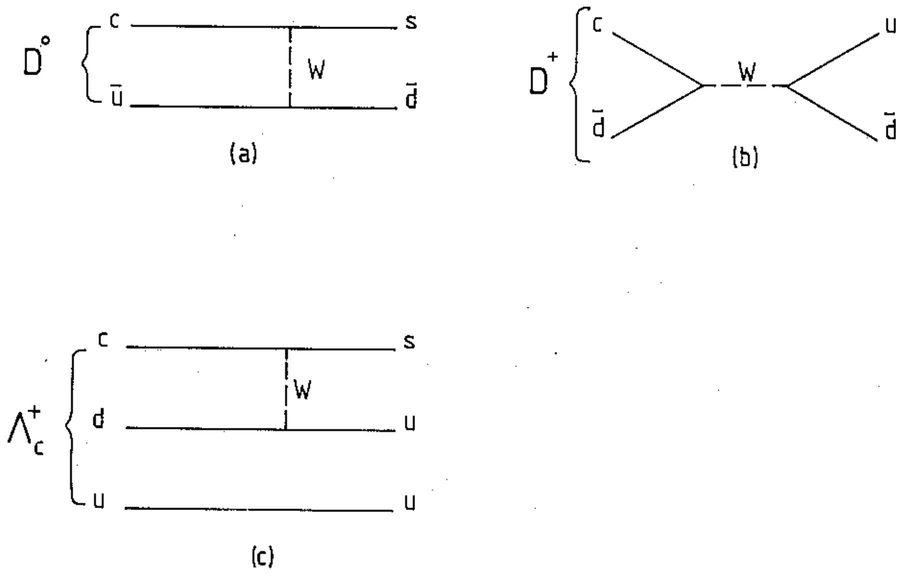

(a) (b) (c)

Figure 1.7 Non-spectator Diagrams for D and Λ_c^+ Decays not a spontaneously broken symmetry:

E110 $$\frac{\Gamma(D^+ \dashrightarrow \mu^+ + \nu)}{\Gamma(K^+ \dashrightarrow \mu^+ + \nu)} \simeq \frac{m_D}{m_K} \simeq \frac{1870}{494}$$

Putting in a value for the rate of kaon decay they estimated:

E111 $$\Gamma(D^+ \dashrightarrow \mu^+ + \nu) \simeq 3.8\times5\times10^7 \text{ s}^{-1}$$

this is to be compared to the total semi-leptonic rate which is of the order of 1×10^{12} s^{-1}.

Thus the purely leptonic decays of charmed mesons are predicted to be very rare indeed.

1.2.3 Hadronic Decays

Maiani (1982) discusses corrections to the parton model predictions for the inclusive hadronic decay rates of D mesons and the Λ_c^+ baryon. Figure 1.7 illustrates the diagrams leading to these corrections due to the interaction of the c-quark with the spectator quark. This process is Cabbibo allowed for the D° and Λ_c^+ and Cabbibo suppressed for the D^+, thus it will decrease the D° and Λ_c^+ lifetimes. The interaction must take place in a J=1 state to avoid the helicity suppression factor due to the small final state quark masses. The D° ($c\bar{u}$) is a J=0 state, and thus requires mixing with states containing valence gluons.

Chau (1982) discusses the relevant quark diagrams for inclusive, non-leptonic decays of heavy quarks. The graph (a) in Fig.1.4 is the most important, as the others are suppressed by helicity conservation (compare the process ($\pi^+ \dashrightarrow e^+ + \nu$). Graph (c) in Fig.1.7 does not contribute to D^+ or F^+decay; the corresponding graph for these are the W-annihilation graphs. At least two gluons must also be emitted to conserve colour. Chau (1982) concludes that the leading order QCD preferred W-emission graphs fail to explain many aspects of the experimentally observed charm decays, the W-exchange and W-annihilation graphs are also required. The assumption that in D° decay the W-exchange graph dominates by a factor of two or three over the W-emission graph fits the decay D° --> two pseudo-scalars well. This dominance also accounts for the D° lifetime being less than the D^+ lifetime, since the W-exchange graph does not contribute to D^+ decay.

1.3 Charmed Particle Lifetimes

Nine experiments have contributed significant numbers of events to the world data on charmed particle lifetimes, they are briefly reviewed below.

Experiment E531 (Ushida (1982), Ushida (1983a), (1983b))

This was a hybrid emulsion experiment in the single horn focussed neutrino beam at Fermilab. The interaction vertex was recorded in emulsion, and the identification of the decay products was performed by an electronic detector downstream. Momentum analysis was provided by drift chambers in a magnetic field, and pions, kaons, and protons were separated by a time-of-flight system. Electromagnetic showers were identified by their passage through various thicknesses of steel. Hadronic energy was recorded in a conventional calorimeter. A high efficiency and low background were claimed for this experiment. Detection losses were estimated using gamma conversions (Niu (1981)), and the use of emulsion allowed a spatial resolution of around 1 micron.

Experiment WA58 (Adamovich (1984a), (1984b))

This was an emulsion experiment in the CERN tagged photon beam. Vertex predictions were obtained from the OMEGA spectrometer located downstream. An efficiency of around 50% for finding the primary vertex was quoted, along with a low background.

Experiment NA16 (Aguilar-Benitez, et al.(1983))

This experiment used the small rapid-cycling hydrogen bubble chamber LEBC in front of the European Hybrid Spectrometer (EHS) at CERN. The chamber was exposed to 360 GeV/c proton and π^- beams. A high resolution image with a resolved bubble diameter of 40 microns was achieved. Only a part of EHS was operational during this experiment, but π detection and magnetic analysis of the charged tracks in the spectrometer were available.

Experiment NA18 (Bedertscher, et al.(1983))

This experiment used the small Freon bubble chamber BIBC upstream of a large streamer chamber. The apparatus was exposed to a 340 GeV/c π^- beam. There was no gammma detection or charged particle identification. Due to the presence of neutrons as well as protons in the chamber the background was considerable.

Experiment NA27

This experiment, following on from NA16, used the hydrogen bubble chamber LEBC II (formerly known as HOLEBC) in an upgraded version of EHS that provided momentum measurement to an accuracy of 1% over the range of interest. As in NA16 the chamber was exposed to proton and π^- beams.

Experiment BC72/73 (Abe, et al.(1984))

In this experiment at SLAC the 40 inch hydrogen bubble chamber, modified to contain one early triggered high resolution camera, was exposed to a monoenergetic beam of 20 GeV/c photons. The chamber was followed by multi-wire proportional chambers, Cerenkov counters, and a lead-glass wall. A scanning efficiency of 94% was claimed for finding charm events.

Experiment MARK II

This experiment at PEP used the MARK II vertex detector surrounding the e^+e^- collision region. A particle spectrometer using a large solenoidal magnetic field allowed charged particles to be identified over about half of the solid angle. The D^0 lifetime was determined from decays of charged D*, and a clean, though small, sample was obtained.

Experiment NA1 (Albini, et al.(1982))

This was an experiment using an active silicon target exposed to a tagged photon beam. Fast decay products were analysed in the FRAMM spectrometer. Pion/kaon separation was achieved by Cerenkov counters downstream, and photon detection by lead-glass absorbers or lead scintillator hodoscopes. In this experiment it was not possible to assign tracks to a particular decay vertex. This experiment provided a large number of identified decays, but the background was quite high.

Experiment NA11

This was the first experiment to use silicon microstrip vertex detectors, with a resolution in each plane of 5 microns. Downstream was the ACCMOR spectrometer and proportional counters providing an on-line effective mass trigger. Although the overall efficiency was low the background was reduced compared to the NA1 experiment and it was possible to reconstruct secondary vertices.

1.3.1 D Meson Lifetimes

Table 1.1 lists the current published values of D^0 and

$D^{\pm}$ lifetimes obtained from the experiments reviewed in section 1.3. The current published world average (Particle Data Group (1984)) is also shown. This average does not include the NA27 result, and is based on 116 events in total. Two results stand out as being rather distant from the avarage. For the D^{o} meson the high value of 0.68 ps from the BC72/73 experiment, and for the D^{+} meson the low value of 0.391 ps from the WA58 experiment. The latter value is possibly due to considerable contamination from F^{+} mesons and Λ_c^+ baryons.

TABLE 1.1
D^{o} AND D^{+} LIFETIMES

Experiment	$\tau(D^{o})$ $(10^{-13}s)$	Events	$\tau(D^{+})$ $(10^{-13}s)$	Events
E531	$2.3^{+0.8}_{-0.5}$	19	$11.5^{+7.5}_{-3.5}$	11
WA58	$2.11^{+1.21}_{-0.63}$	22	$3.91^{+2.35}_{-1.25}$	10
NA16	$4.1^{+2.6}_{-1.3}$	16	$8.4^{+3.5}_{-2.2}$	15
NA18	$4.1^{+2.6}_{-1.4}$	9	$6.3^{+5.0}_{-2.7}$	7
NA27	$3.9^{+1.6}_{-1.0}$	11	$12.2^{+4.5}_{-2.3}$	35
BC72/73	$6.8^{+2.3}_{-1.8}$	22	$7.2^{+2.3}_{-2.0}$	21
MARK II	$4.2^{+1.3}_{-1.0}$	27	---	---
NA1	---	---	$9.5^{+3.1}_{-1.9}$	98
NA11	4.2 ± 1.0	23	8.8 ± 2.7	13
P.D.G (1984)	$4.4^{+0.8}_{-0.6}$		$9.2^{+1.7}_{-1.2}$	

At the recent Leipzig conference Klanner (1984) presented new world averages, excluding these two results:

$\tau(D^{o}) = 3.7^{+0.5}_{-0.4} \times 10^{-13}$s
$\tau(D^{+}) = 8.9^{+1.4}_{-1.0} \times 10^{-13}$s

1.3.2 Λ_c^+ and F^+Lifetimes

The current situaution regarding the lifetimes of the Λ_c^+ baryon and $F^{\pm}$ mesons is unclear. Firstly the statistics are low for these particles, around 20 published events for each, and secondly there is some confusion over the F mass (Bellini (1984)). The Particle Data Group Values (1984) are:

$\tau(F) = 1.9^{+1.3}_{-0.7} \times 10^{-13}$s
$\tau(\Lambda_c^+) = 2.3^{+1.0}_{-0.6} \times 10^{-13}$s

It is possible that the F lifetime may change considerably when the mass discrepancy is resolved.

In general the values given by the Particle Data Group are probably close to the true lifetimes, except perheps in the case of the F meson whose identification is less clear. In this thesis the values given by the Particle Data Group (1984) will be assumed.

1.4 Charmed Particle Decays

The decays of charmed particles are discussed in sections 1.4.1 and 1.4.2. The semi-leptonic decays have an additional importance in the NA25 experiment as the prompt muon arising from such decays was used as a "charm" trigger.

1.4.1 Semi-leptonic Decays

Trilling (1981) discussed the evidence for D^+ semi-leptonic branching ratios, he proposed a value of 19 % assuming a ratio of charged to neutral D meson lifetimes in the range 3-10. In the light of recent results, with a ratio now in the range 2-3, perhaps the slightly lower value of 18% should be taken. The value of the D^o branching ratio is much less certain, Trilling (1981) calculated it from the semi-electronic D^+ branching ratio and assumed a lifetime ratio of 5 giving a semi-electronic D^o branching ratio of 4%. Given the recent measurements of charged/neutral lifetime ratio this seems too low. A direct measurement of the neutral branching ratio of 5.5 ± 3.7% was made by MARK II.

The semi-muonic branching ratio has been measured by the experiments CELLO, MARK J, MAC, and MARK III (Schneider (1983)). The results agree with each other within errors, and the average (omitting the MAC result which has large assymetric errors) is:

$B(\mu)$ = 10.3 ± 1.4% (average of D^+ and D^o over all energies)

The MARK III experiment has measured both the electronic and muonic branching ratios, and both are equal within their statistical and systematic errors (Hanson (1983)).

1.4.2 Hadronic Decays

For the hadronic decays of the D mesons, Trilling (1981) is the most complete source of information. Recent results are given by Bellini (1984). Four experiments, MARK-I-LGW, MARK II, NA16, and the Tagged Photon Spectrometer (TPS) have contributed most to the statistics of the neutral and charged D decay modes. Table 1.2 summarises the data for the D meson branching ratios.

TABLE 1.2

D MESON HADRONIC BRANCHING RATIOS

Channel	Branching Ratio (%)			
	MARK II	LGW	NA16	TPS
$K^- \pi^+$	3.0 ± 0.6	2.2 ± 0.6	13^{+11}_{-7}	---
$\overline{K^0} \pi^0$	2.2 ± 1.1	---	---	---
$\overline{K^0} \pi^+ \pi^-$	3.8 ± 1.2	4.0 ± 1.3	---	---
$K^- \pi^0 \pi^+$	8.5 ± 3.2	12.0 ± 6.0	---	10.0 ± 3.7
$K^- \pi^+ \pi^- \pi^+$	8.5 ± 2.1	3.2 ± 1.1	10 ± 4	---
$\overline{K^0} \pi^+$	2.3 ± 0.7	1.5 ± 0.6	---	---
$K^- \pi^+ \pi^+$	6.3 ± 1.5	3.9 ± 1.0	14^{+6}_{-5}	---
$\overline{K^0} \pi^0 \pi^+$	12.9 ± 8.4	---	---	---
$\overline{K^0} \pi^+ \pi^- \pi^+$	8.4 ± 3.5	---	---	---
$K^- \pi^+ \pi^+ \pi^+ \pi^-$	< 4.1	---	---	---
$K^- \rho^+$	7.2 ± 3.0	---	---	$3.2^{+2.3}_{-1.8}$
$\overline{K^{*0}} \pi^0$	$1.4^{+2.3}_{-1.4}$	---	---	$0.9^{+1.4}_{-0.9}$
$K^{*-} \pi^+$	$3.6^{+0.6}_{-0.1}$	---	---	$3.4^{+3.9}_{-2.8}$
$\overline{K^0} \rho^0$	$0.1^{+0.6}_{-0.1}$	---	---	---
$\overline{K^{*0}} \pi^+$	< 3.7			

TABLE 1.3
CHARGED MULTIPLICITIES IN D MESON DECAYS

	D^0		D^+	
Charged Multiplicity	MARK II	LGW	MARK II	LGW
0	9.6±2.5	8.5±3.0		
1			47.6±5.6	37±10
2	63.0±5.4	73±10		
3			46.8±5.6	60±12
4	22.2±4.7	16±4.0		
5			5.6±2.4	3.0±3.0
6	5.2±3.1	2.5±1.5		
Average	2.46±0.14	2.3±0.3	2.16±0.16	2.3±0.3

1.5 Charm Production Cross-Sections

Kernan and VanDalen (1984) provide the most recent review of charm production cross sections in strong interactions. A brief summary of the major experimental determinations is given below.

1.5.1 Experiment CERN-Saclay-ETH at the ISR

This experiment was performed at a centre of mass energy of 53 GeV. The apparatus consisted of two electron and two muon spectrometers. The correction for the acceptance of the apparatus was very model dependent, the authors assumed uncorrelated D $\overline{D}$ production with the following functional cross section dependence:

E112 $$\frac{Ed^3\sigma}{d^3p} \approx (1-x)^n e^{-bm}$$

Taking values of 5 for n and 2.5 GeV^{-1} for b the resulting cross section was 70 ± 36 microbarns. The acceptance changes by 50% for a ± 1 GeV change in b, and by 15% for change of ± 1 in the exponent n. Refining their analysis by using the electron-positron pair data they found:

$$\sigma(tot) = 21.9 \pm 5.0\ \mu b$$

1.5.2 Beam Dump Experiments

At CERN the bubble chambers BEBC and Gargamelle, and the neutrino detectors CDHS and CHARM have been used to search for prompt neutrinos arising from leptonically decaying charmed particles. At Fermilab a similar search was made by the E613 collaboration. All these experiments used 400 GeV/c protons, and assumed that all the prompt neutrinos had arisen from D $\overline{D}$ decay, and that the muonic branching ratio for D mesons (averaged) was 8%. They also assumed an invariant cross section of the form:

E113 $\sigma \approx s^{1.3}A^{1}(1-x_F)^{3}e^{-2p_T}$

The results from the CERN experiments were:

CHARM $\sigma(D\overline{D}) = 19.6 \pm 6\ \mu b$

BEBC $\sigma(D\overline{D}) = 30 \pm 10\ \mu b$ for muon neutrinos
$\sigma(D\overline{D}) = 17 \pm 4\ \mu b$ for electron neutrinos

Both results are valid for $x_F > 0.5$

Experiment E613 (FFMOW) at Fermilab had a much larger acceptance than the CERN experiments and assuming linear A dependence they found a cross section of:

$$\sigma(pN \dashrightarrow D\overline{D}+X) = 17.1 \pm 4.7\ \mu b$$

The Caltech-Stanford beam dump experiment studied single and double muon production from protons incident upon an iron target. Two experimental runs were made, one with 400 GeV/c protons analysing data with $p_T > 0.8$ GeV/c and $x_F > 0.1$, and one with 350 GeV/c protons and $p_T < 0.6$ GeV/c at $x_F \simeq 0$. Assuming a cross section dependence as E112 with p_T rather than m_T as the variable in the exponent, they found:

$p_T > 0.8 \quad \sigma(D\bar{D}+X) = 31\ \mu b/\text{nucleon}$

$p_T < 0.6 \quad \sigma(D\bar{D}+X) = 22 \pm 9\ \mu b/\text{nucleon}$

The E595 (CCFRS) experiment at Fermilab studied p-Fe and π-Fe interactions with a 20 GeV/c muon trigger. Assuming the intrinsic charm model (see section 1.1.4) they found diffractive cross sections of 2.5 microbarns for protons and 1.9 microbarns for pions. This would imply an intrinsic charm component of 0.012% in the proton and 0.021% in the pion. The proton energy was 350 GeV and the pion energy was 278 GeV. For diffractive charm production with incident pions they found a cross section of:

$$\sigma(D\bar{D}+X) = 17.8 \quad \mu b/\text{nucleon}$$

for $x_F > 0$ and assuming linear A dependence. For the protons they found:

$$\sigma(D\bar{D}+X) = 22.8 \pm 2.1 \pm 3.6\ \mu b/\text{nucleon}$$

for $-1 < x_F < 1$.

1.5.3 Other Experimental Data

Experiment NA11 at CERN used a hadron spectrometer with a large acceptance and three multicell Cerenkov counters for pion/kaon/proton separation. The apparatus was triggered by a prompt electron. Unfortunately although this trigger considerably increased the signal to background ratio, it also increased the uncertainty in the cross section. Assuming uncorrelated $D\,\overline{D}$ production and a cross section dependence given by E112 with the variable p_T rather than m_T they found:

$$\sigma(\pi\ \mathrm{Be} \dashrightarrow D\overline{D}+X) = 48 \pm 15 \pm 50\%\ \mu b$$

for $n = 0.8$, and $b = 1.1\ \mathrm{GeV}^{-1}$ at 175/200 GeV/c

A shorter run at 120 GeV/c gave the following ratio of cross sections:

$$\frac{\sigma(D\overline{D})(\text{at 120 GeV/c})}{\sigma(D\overline{D})(\text{at 175/200 GeV/c})} = 0.62 \pm 0.34$$

Two recent experiments in the bubble chamber LEBC have measured the cross section for pions and protons at 360 GeV/c. For negative pions only 13 decays were to states with known branching ratios, and these showed a considerable difference between those mesons with a quark from the pion ($\overline{u}d$) and the others:

$$\sigma(c\overline{u}/\overline{c}d) = 31\quad \mu b\quad (9\ \text{events})$$

$$\sigma(c\overline{d}/\overline{c}u) = 9\quad \mu b\quad (4\ \text{events})$$

For $x_F > 0$ the inclusive single charm cross section was found to be:

$$\sigma(D/\overline{D}) = 2\sigma(D\overline{D}+X) = 40\quad \mu b$$

For the proton data (leading mesons $\overline{D^\circ}$, D^-) they had 9 events giving cross sections as follows:

$$\sigma(D^-/\overline{D^\circ}) = 42^{+23}_{-8}\ \mu b\quad (7\ \text{events})$$

$$\sigma(D^+/D^\circ) = 14^{+18}_{-8}\ \mu b\quad (2\ \text{events})$$

Both of these results for pion and proton production suggest that beam fragmentation is important in D meson production. Assuming that the observed difference in C and $\overline{C}$ was due to $\Lambda_c^+ \overline{D}$ producion with missing Λ_c^+ they found:

$$\sigma(D\overline{D}) = 14^{+18}_{-4}\ \mu b, \quad \sigma(\Lambda_c^+\overline{D}) = 28^{+21}_{-12}\ \mu b$$

Using all the 29 decays found, they calculated the following cross sections with the ratio $D/\overline{D} = 1.3 \pm 0.5$:

$$\sigma(D\overline{D}) = 24 \pm 7\ \mu b, \quad \sigma(\Lambda_c^+\overline{D}) = 8^{+10}_{-8}\ \mu b$$

The inclusive single $D,\overline{D}$ cross section was:

$$\sigma(D,\overline{D}) = 56^{+25}_{-12}\ \mu b \quad \text{for all } x_F$$

Experiment NA18, using the bubble chamber BIBC measured the production cross section in C_3F_8 for 340 GeV/c pions. Using a central production model they found:

$$\sigma(D\overline{D}+X) = 73.2 \pm 27.4\ \mu b \quad (A^{0.67})$$

$$\sigma(D\overline{D}+X) = 28.2 \pm 10.5\ \mu b \quad (A^{1})$$

Comparing this data (A = 17.1) with the LEBC data (A = 1) favours the linear A dependence of the charm production cross section.

Three of the proton experiments discussd in the previous sections have the desirable features of large acceptance, low background, and the absence of trigger bias. These are CCFRS, FFMOW and LEBC-EHS (NA16). Table 1.4 summarises the results from these experiments.

TABLE 1.4
pN CHARM PRODUCTION CROSS SECTIONS

$\sigma(pN \dashrightarrow D\bar{D}+X)$

Experiment	Cross section (μb)	A Dependence
CCFRS	22.8 ± 2.1 ± 3.6	1
	87 ± 8 ± 14	2/3
FFMOW	17.1 ± 4.7	1
	97 ± 27	2/3
LEBC-EHS	24 ± 7 (29 Decays)	(Hydrogen)
	14^{+18}_{-4} (9 Decays)	(Hydrogen)

NA 16 also estimate the $\Lambda_c^+ \bar{D}$ cross section. Using all 29 decays they find a cross section of:

$\sigma(pp \dashrightarrow \Lambda_c^+\bar{D}X) = 8^{+10}_{-8}$ microbarns

Bellini (1984) gives the new cross section obtained when the LEBC data is combined with the recently measured LEBC branching fractions (larger than MARK II, see table 1.2):

$$\sigma(p+N \dashrightarrow D\bar{D}+X) = 15.5^{+8.2}_{-4.6}\ \mu b$$

NA11 calculated a D* cross section at 120 and 175/200 GeV/c (for incident π^-) of:

$$\frac{\sigma(D^*)}{\sigma(D)} = 0.9$$

CHAPTER 2 THE EXPERIMENTAL APPARATUS

The apparatus used in the experiment NA25 consisted of a small heavy-liquid bubble chamber equipped with a holographic recording system, a muon detector and a system of scintillators for detecting the occurrence of an interaction in the bubble chamber.

The relative positions of the apparatus are shown in Fig.2.1. Two CEDAR's (Cerenkov Differential Counter with Achromatic Ring focus) were positioned further upstream. These were used to identify pions and protons in the beam. Downstream of the CEDAR's were two standard SPS multiwire proportional chambers (MWPC's). These were used to determine the trajectory of a particle incident upon the bubble chamber, which, with its array of scintillation counters, was placed immediately downstream. Following HOBC and the counter S3 was a tungsten and iron beam dump. Following this hadron absorber was the muon detector which consisted of a sandwich of iron plates, MWPC's, and scintillator hodoscopes. In the absence of any magnetic fields in the muon detector muons were identified solely by range.

2.1 The Beam Line

The experiment was situated in the H2 beam line in the CERN North Area. The H2 beam was a high energy high resolution hadron beam giving particles with momenta up to 400 GeV/c. In NA25 the beam was used to deliver positive hadrons at energies of 360 GeV/c and 200 GeV/c. At 360 GeV/c almost all the particles in the beam were protons, with less than 1% of the total flux coming from other particles. At 200 GeV/c the flux consisted of 77% protons, 21% pions, and about 2% kaons.

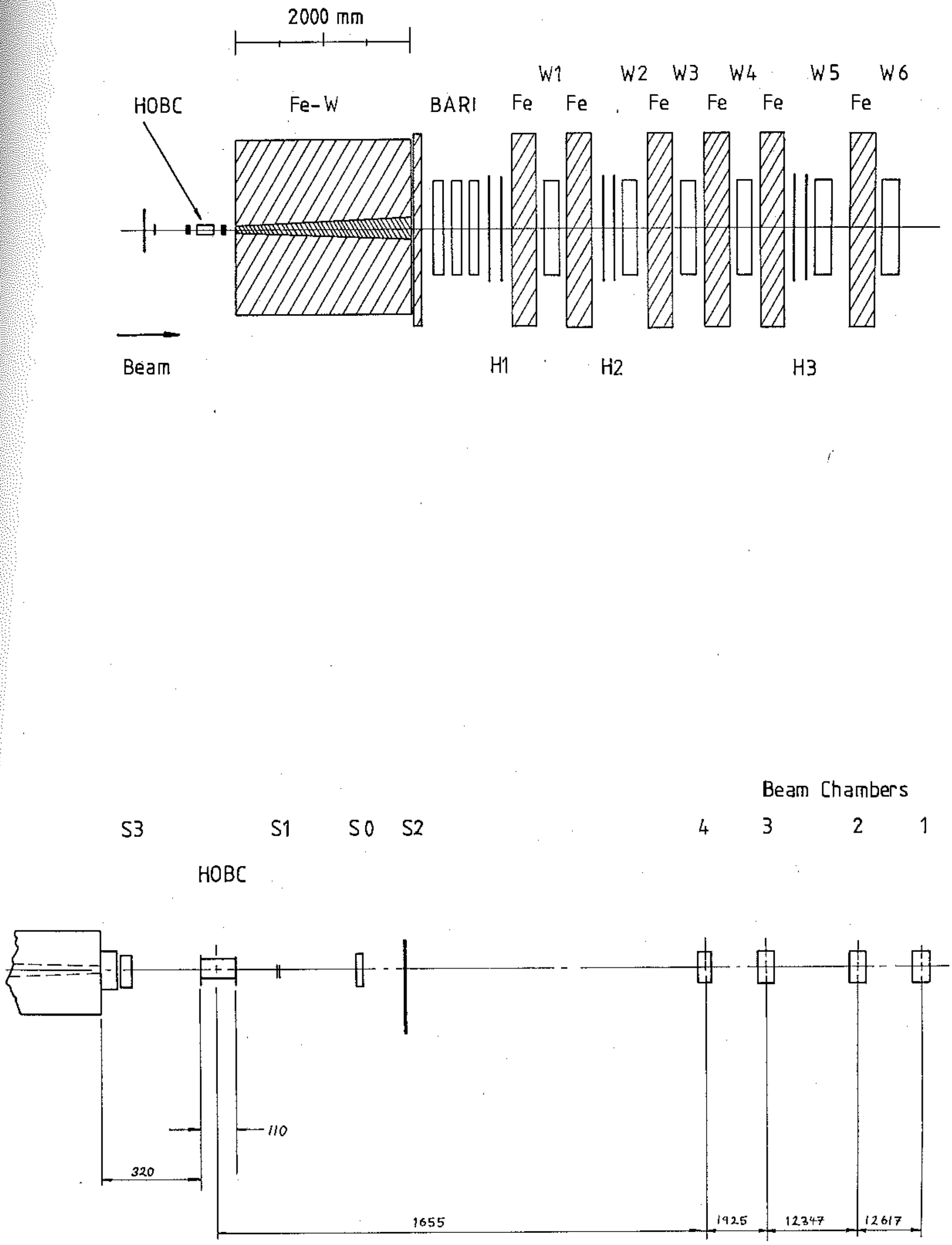

Figure 2.1 Layout of the NA 25 Experiment

In the North Area the SPS provided only a slow extracted beam, with a uniform spill of around two seconds. This would have lead to an undesirable situation with particles passing through HOBC during all of its sensitive period, resulting in large bubbles from the older tracks obscuring the tracks from in-time particles. A fast kicker magnet had been installed in the beam to deflect the primary beam vertically downwards for a short interval during the spill. This magnet was used to suppress the beam except for a short "beam window" of a few microseconds. The kicker magnet was not totaly efficient, and some protons might have reached the production target even when the kicker was energised, thus a few particles could arrive at the bubble chamber before the beam window but during the sensitive period of the chamber. To minimse this effect a rotating collimator was also placed in the beam (see Coet (1982) Fig.6), and this was used to suppress the beam in advance of, or following, the beam window . The rotating collimator was unable to reduce the kicker magnet leakage at times very close to the beam window. In spite of these both these precautions it was still possible for a few particles to arrive during the sensitive period of HOBC, but outside the beam window. These unwanted tracks were an important factor in the choice of operating conditions for the chamber. More details of the H2 beam line can be found in Coet (1982).

2.2 The CEDAR's and Beam Chambers

A CEDAR counter (Boret (1975)) is a Cerenkov detector which can be tuned to allow the detection of any particle whose velocity lies within a narrow range. In a beam with a small momentum spread a CEDAR can be used to tag particles with a given mass, and thus identify them.

Two N-type CEDAR's were used in NA25, they were well suited for the identification of pions and protons over the range of incident beam momenta used in the experiment.

At a beam momentum of 360 GeV/c it was unnecessary to use the CEDAR's during data taking since the beam contained essentially 100% protons. At 200 GeV/c, where the mixture of protons and pions was different, CEDAR 1 flagged incident protons and CEDAR 2 pions.

The two beam chambers, B1 and B2, were standard SPS MWPC's each consisting of two planes of wires spaced at 1 mm. One plane in each chamber was vertical and the other horizontal. The active area of each chamber was 100 mm by 100 mm. These chambers were used to estimate the trajectories of incident particles, this enabled an estimate of the entry point to HOBC of an incident particle to be made.

2.3 The Scintillation Counters

Four groups of scintillation counters, S0, S1, S2, S3, surrounded the bubble chamber as shown in Fig.2.1 . All the counters were constructed from NE110 scintillator. The four S0 counters, S0A, S0B, S0C, S0D, are shown in Fig. 2.2 . These were used to veto incident particles in the beam halo, and to assist in steering the beam during setting up of the experiment. The S1A and S1B counters are shown in Fig.2.3 . A coincidence between these counters determined whether there was a particle incident on the bubble chamber. The S2 counter is shown in Fig. 2.4 . This was a single piece of scintillator with light guides at either end and photomultipliers connected in logical OR. The presence of the central hole would have resulted in unacceptable inefficiencies if only one photomultiplier had been used. This counter was used to veto particles which were accompanied by a beam halo particle. The four S3 counters, immediately downstream of HOBC, were used to determine whether an incident particle had interacted in the chamber. Each counter consisted of a square piece of scintillator 100 mm by 100 mm by 5 mm thick.

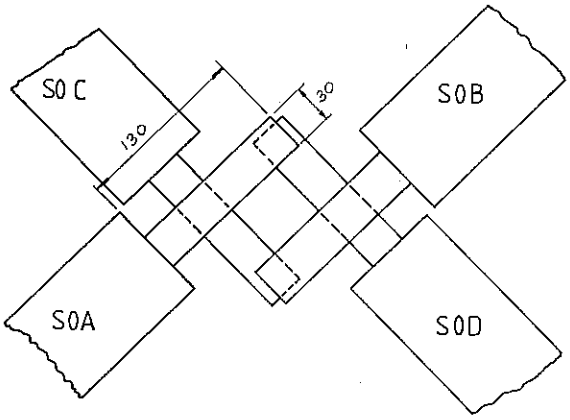

Figure 2.2 The S0 Scintillation Counters

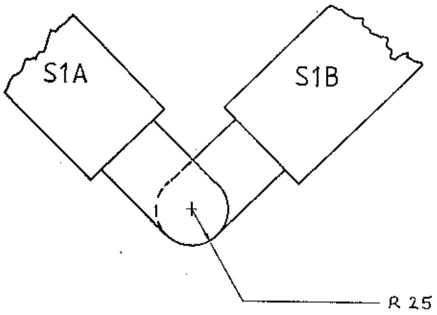

Figure 2.3 The S1 Scintillation Counters

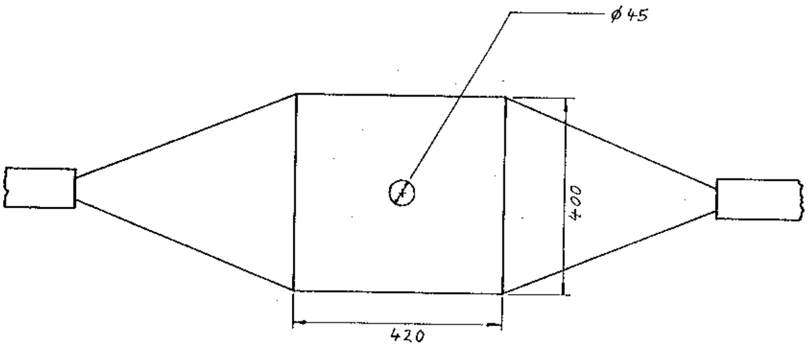

Figure 2.4 The S2 Scintillation Counter

2.4 The Muon Detector

The muon detector, consisting of a 2.0 metre iron and tungsten beam dump followed by a sandwich of iron, MWPC's and scintillation counter hodoscopes, was placed as close as possible to HOBC in order to reduce the possibility of pions decaying into muons. The dump was thick enough (11.7 absorption lengths of iron, 19.4 of tungsten) to absorb the majority of hadrons created in the proton-nucleon interaction at 360 GeV/c, but thin enough to allow prompt muons with momenta > 5 GeV/c to escape from its downstream end.

The hodoscopes, H1, H2, and H3, were used by the fast triggered logic to decide whether a muon had penetrated through the dump. The hodoscope planes were separated by lengths of absorbing material, mainly iron, and by requiring hits in H1 or H2 or H3 it was possible to increase the length of absorber through which a moun had to pass. Each hodoscope consisted of a pair of scintillation counter planes. Each plane consisted of twenty four counters, each with dimensions 1200 by 50 by 15 mm, resulting in an active area of 1200 by 1200 mm. Each pair of planes had one plane with strips vertical and the other with strips horizontal.

The MWPC's were divided into two groups, known as the Bari and EMI chambers. Both of these sets of chambers were used by the offline analysis program to reconstruct the tracks of possible muons.

The three Bari chambers were positioned immediately downstream of the dump. These chambers had originally been used in the Single Arm Spectrometer at Fermilab (Anelli (1978)). Each chamber had three sense planes, with hexagonal geometry, enclosed in a single gas volume. One plane had its wires vertical the other two were at $\pm{}^{\circ}60$ to the vertical. Each plane consisted of 288 20-micron gold plated tungsten wires. These were spaced at 2 mm intervals. The gas mixture used contained 67% argon, 31% isobutane, 0.3% Freon 13B and approximately 2% methylal. The voltage plateau was 5.7 - 6.3 kV, and the efficiency of each plane was typically 98%.

The six MWPC's, W1 to W6, were originally used in the external muon identifier of the Gargamelle bubble chamber at CERN (Brand et al.(1976) and Beuselinck et al.(1978)). Each chamber contained two independent planes of anode wires oriented at ± 30° to the vertical, and two cathode strip planes oriented vertically and horizontally. The wire diameter was 20 microns and the wire spacing 4 mm. To obtain different spatial resolutions groups of 2, 4, or 8 wires were joined together to one electronics channel. The cathodes were fabricated from painted silver strips, 14 mm wide, with 2 mm spacing. The active area used in NA25 was a rectangle 1000 mm (horizontally) by 1200 mm (vertically). In this region the wires were joined in pairs. The gas mixture used consisted of 55% argon, 40% isobutane, and 5% methylal. The efficiency of each chamber was greater than 99%.

The on-line muon trigger, which provided a twenty-fold increase in the charm content of the holograms, used hits in hodoscope H1 combined with an interaction trigger obtained from the scintillation counters. The required hits in the counters and hodoscopes were:

	Scintillator				Hodoscope		
	S0	S1	S2	S3	H1	H2	H3
Hits:	0	1	0	>3	1	--	--

2.5 The Bubble Chamber HOBC

The bubble chamber HOBC was a small rapid-cycling heavy-liquid chamber using in-line holography as the recording technique. The visible volume was 110 by 50 by 60 mm^3 the longest dimension being parallel to the particle beam. At the top of the chamber were the heat exchanger coils, the valves and the pressure gauge. The piston was joined to the body by stainless steel bellows. Separating the active liquid from the piston assembly was a rubber membrane made of 1.5 mm VULKOLAN. This membrane reduced parasitic boiling in the chamber. The chamber pressure was regulated by a feedback loop on the LEBC type expansion motor. The chamber body was machined from stainless steel, and incorporated two rectangular optical quality windows made from BK7 glass. These contained the chamber fiducial marks, eight on each window.

The chamber temperature was controlled by two water loops, one located in the chamber body and the other in the piston. The water was drawn from a common reservoir which was stabilised to a few 10^{-2} °C. As the chamber was run hot, typically 53 °C, the whole chamber was surrounded by an aluminium tank which was heated by electrical heating strips to the same temperature as the chamber body. The chamber was used with the Freons C_3F_8 and C_2F_5Cl.

The effects of various operating conditions on bubble size, growth rate, bubble density, and heat dispersion have been considered in detail by Benichou et al.(1983) and Williams (1984). Table 2.1 summarises the operating conditions for the two data taking runs of Autumn 1981 and Autumn 1982. Figure 2.5 shows the main features of HOBC in 1982.

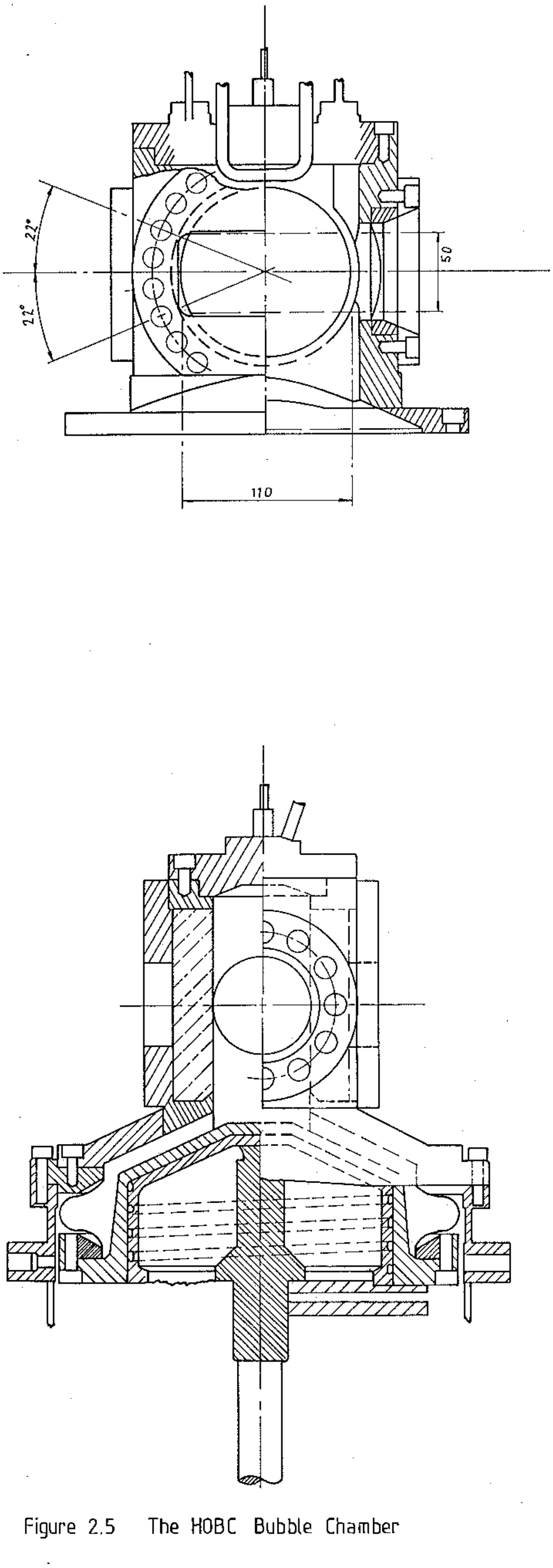

Figure 2.5 The HOBC Bubble Chamber

TABLE 2.1

OPERATING CONDITIONS OF HOBC

	Autumn 1981	Autumn 1982
Filling	C_2F_5Cl	C_3F_8
Operating Temperature	48°C	53°C
Static Pressure	26 bar	26 bar
Liquid Density	1.25 g cm^{-3}	1.25 g cm^{-3}
Expansion Cycle Duration	5 ms	5 ms
Bubble Density	200 cm^{-1}	95 cm^{-1}
Bubble Size	10 μm	12 μm
Repetition Rate	1 - 2 Hz	10 Hz
Tracks per Expansion	40	80

2.6 Holographic Recording in HOBC

Two different schemes of holographic recording were considered, and both were tested using HOBC under real operating conditions.

2.6.1 The Choice of Holographic Recording Scheme

The simplest scheme, that of in-line holography, is illustrated in Fig.2.6 . An expanded laser beam provides colinear object and reference beams recording onto a plane film surface normal to the beam. There are two main requirements for this to work satisfactorily. Firstly, in order to adequately separate the real and virtual images, the recording must occur in the Fraunhofer diffraction region of the bubbles, while remaining in the near field of the reference beam. Secondly the bubbles must not obscure the reference beam by more than 1% of the region being recorded. There is no angle between the object and reference beams and this minimises the resolution requirements of the film. The in-line scheme requires very simple recording and replay arrangements and minimises the laser power and coherence length requirements.

The other scheme, that of two-beam holograhy is shown in Fig.2.7 . Compared with in-line holography it required a more complex recording and replay system, but it did offer some advantages.

1) The virtual and real images are separated both laterally and in depth; this reduces the interference from the virtual image compared with the in-line scheme. This is the major advantage of double beam holography.

2) The ratio of the object beam intensity to the reference beam intensity can be accurately controlled for optimum recording.

3) Dark field illumination is used, and potentially this offers a better signal to noise ratio upon reconstruction.

4) The reference beam can bypass the chamber and thus need not be affected by the turbulent liquid of the chamber.

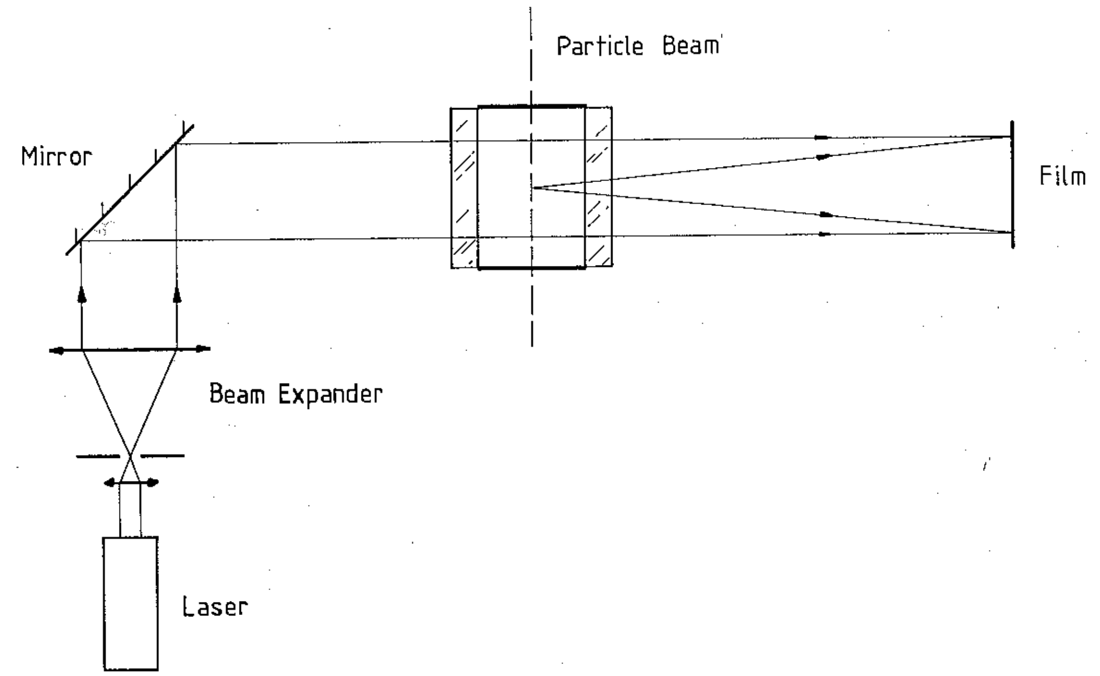

Figure 2.6 Recording Arrangement for In-line Holography

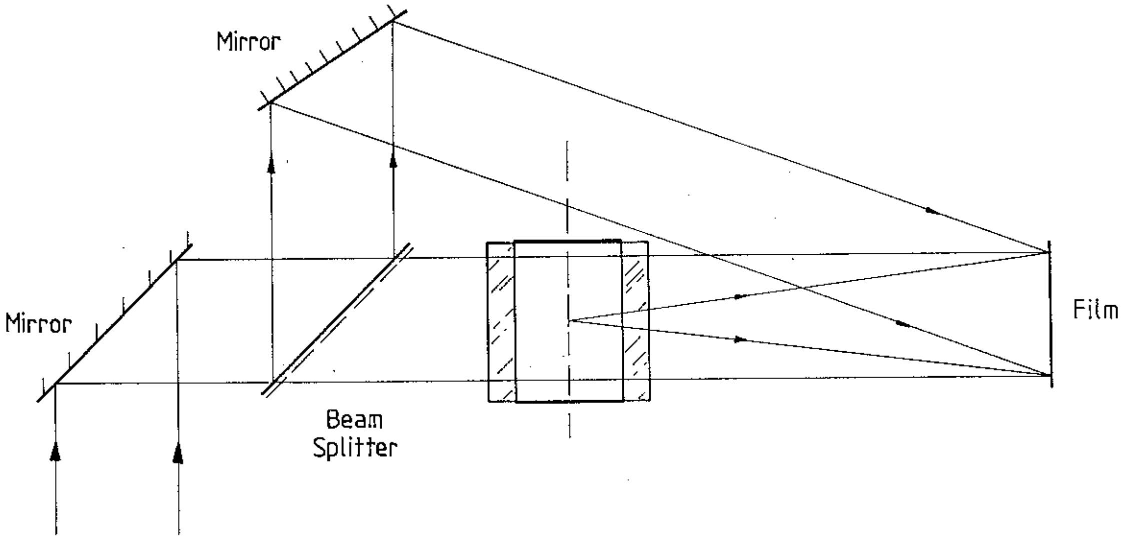

Figure 2.7 Recording Arrangement for Two-Beam Holography

One serious disadvantage of the side-band Fresnel hologram (which is what the double beam hologram would be in the HOBC recording arrangement) is that it requires a higher film resolution to record a given maximum object frequency than does the in-line Fraunhofer hologram. It can be shown (Collier et al.(1971)) that to avoid any angular overlap of the waves forming the image with the zero-order waves, the maximum spatial frequency that must be recorded by the film is four times the maximum spatial frequency of the object.

Tests carried out in HOBC (Benichou et al.(1983)) showed that under actual operating conditions the difference between the two schemes was minimal in terms of the quality of the replayed image. The in-line arrangement was chosen for the data taking runs because of its greater simplicity.

2.6.2 The Laser, Camera, and Optical System

The pulsed laser used was the Lambda Physik EMG101 excimer laser. This laser could be randomly fired at rates up to 30 Hz with a time delay jitter of less than 5 ns. This was filled with XeCl and produced 10 ns pulses at a wavelength of 308 nm. The ultraviolet beam from the excimer laser was used to pump a dye laser so that a visible beam could be produced. The dye laser was a Lambda Physik FL2000E, used with Coumarin 307 dye. The dye laser was tuned to 514 nm to match the strong green laser line of the CW argon-ion laser, and was used with an intercavity etalon to narrow the single mode bandwidth to around 1 GHz. This would correspond to a coherence length of about 250 mm. Tests carried out at CERN by Dykes et al.(1980), using the similar FL2002 dye laser, showed that a coherence length of around 140 mm could be obtained with a 4mm Fabry-Perot etalon in the oscillator cavity. The dye laser was obscured so that its output was 3 mJ, this was enough to expose the film to a density of 1.3 which was very close to the maximum contrast exposure (Royer (1981)).

Considerations of resolution made it desirable to locate the recording plane as close to the bubbles as possible, once the far-field condition (E301) had been satisfied. The problems of locating a camera system close to HOBC and its aluminium heat shield led to an image of the chamber being holographically recorded rather than the chamber itself. The optical problems of turbulence in the bubble chamber could also be reduced by minimising the distance between the object and the hologram plane. The useful information in the diffracted wave lies in the modulating envelope due to the finite extent of the object. If the extent of this envelope can be made small with respect to the mean turbulence size then both the diffracted wave and the reference wave suffer similar distortions. A high quality relay lens (ERASME type, f= 300 mm, f-number = 2.8) was used with a three element field lens (f= 330 mm) at the rear image point of the first lens. This field lens was made of three converging elements with large radii of curvature to minimise the aberrations. With this lens system the centre of HOBC was situated at a distance of 40 mm from the hologram. The optical system used in NA25 is shown in figure 2.8.

The camera and film transport were capable of working at speeds of up to six frames per second. The film used was Agfa Holotest 10E56 on a 170 micron polyester base with an anti-halo coating. The cut off frequency for this emulsion was around 1500 lines/mm. Each film reel held enough film for about 2100 HOBC frames.

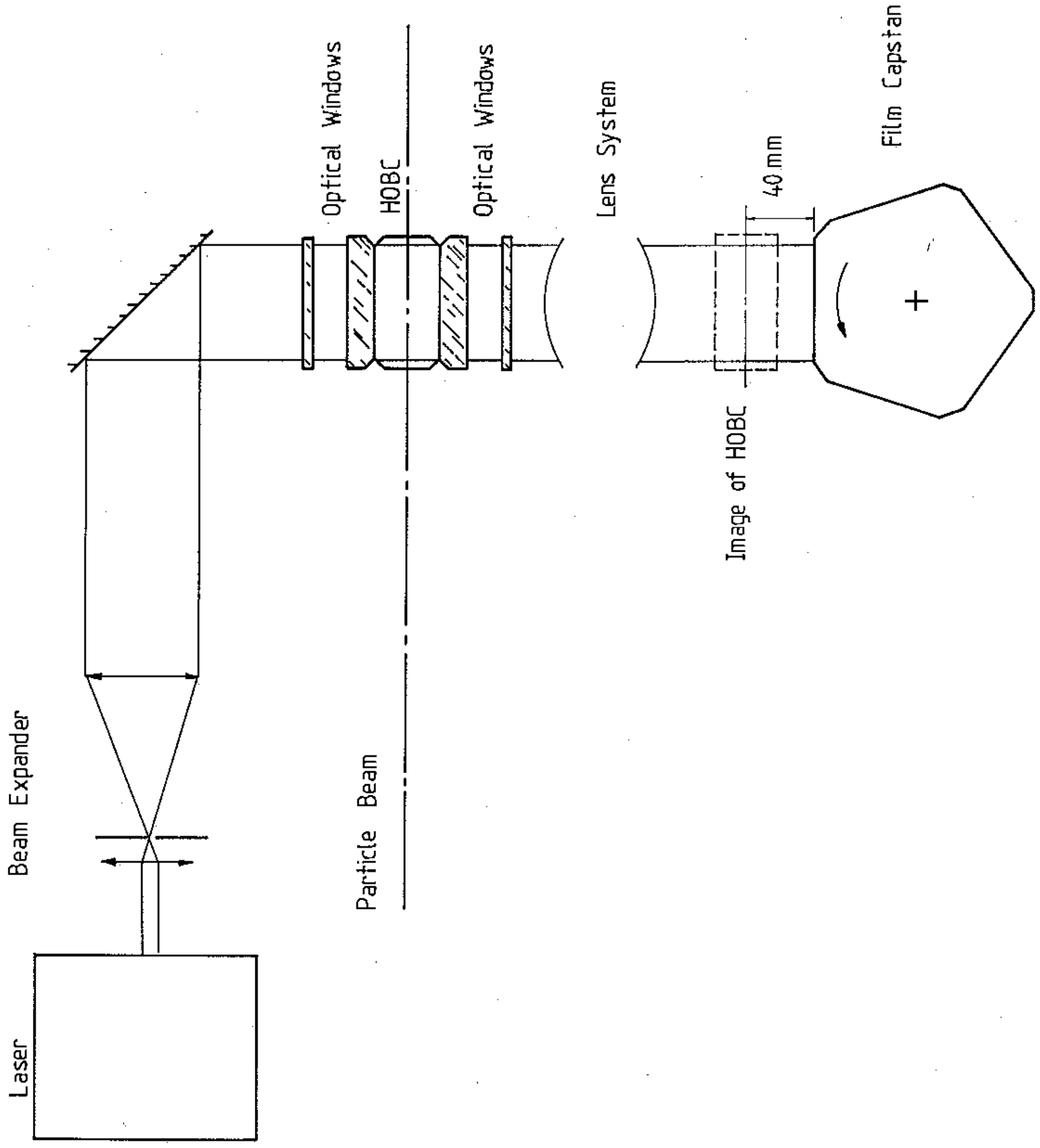

Figure 2.8 Recording Arrangement used in NA 25

CHAPTER 3 HOLOGRAPHIC RECORDING AND REPLAY

In this chapter the formation and replay of holograms recorded in the Fraunhofer diffraction region of the object, with a colinear reference beam whose diameter is such that the film lies in its near-field, are discussed. The effects of object shape, coherence, and film limitations are considered. An analysis of the three-dimensional image structure from the hologram of an opaque circular disc is presented.

3.1 The Formation of a Fraunhofer Hologram

The discussion is limited to the case of a collimated reference beam, and applying a far-field condition in the object space (ξ , η)

E301 $$\frac{\pi \ (\xi^2 + \eta^2)_{MAX}}{\lambda \ z} \ll 1$$

where the object distribution is A(ξ , η) , λ is the recording beam wavelength, and z is the distance between the object and the recording plane. The hologram can be regarded as an interference process between the incident plane wave and the diffracted field propagating from the object. This interference pattern is recorded on photographic film whose development is controlled such that the amplitude transmittance is equal to the intensity of the interference pattern. As will be shown the interference pattern consists of a linear superposition of zone lenses, whose amplitude is modulated by the Fourier Transform of the object amplitude distribution.

Following Tyler and Thompson (1976), consider an object with a distribution A as above, illuminated by a plane wave of infinite extent, with a wavelength λ and an amplitude B. The field distribution, $\psi(x,y)$, at the hologram plane, which is located at a distance z from the object, is given by:

$$\text{E302} \quad \psi(x,y) = \frac{-iB}{\lambda z} e^{ikz} \iint_{-\infty}^{+\infty} [1-A(\xi\ ,\ \eta)\exp[\frac{ik}{2z}((x-\xi)^2 + (y-\eta)^2)]\ d\xi d\eta$$

$$I(x,y) = \psi(x,y)\psi^*(x,y)$$

Applying the far field condition the quadratic terms can be neglected. Evaluating the integral in E302 yields:

$$\text{E303} \quad I(x,y) = B^2\left\{1-\frac{2}{\lambda z}[\sin(\frac{\pi r^2}{\lambda z})\mathcal{R}_e\tilde{A}(\frac{x}{\lambda z},\frac{y}{\lambda z}) + \cos(\frac{\pi r^2}{\lambda z})\mathcal{I}_m\tilde{A}(\frac{x}{\lambda z},\frac{y}{\lambda z})] + \frac{1}{\lambda^2 z^2}\tilde{A}(\frac{x}{\lambda z},\frac{y}{\lambda z})\tilde{A}^*(\frac{x}{\lambda z},\frac{y}{\lambda z})\right\}$$

where $r^2 = x^2 + y^2$

and $A(\frac{x}{\lambda z},\frac{y}{\lambda z})$ is the Fourier Transform of $A(\xi,\eta)$

3.2 The Reconstructed Field

Before considering the effects of object shape, film size, noise, and partial coherence, the reconstructed field amplitude will be discussed for the case of an infinite hologram with infinite film resolution in the coherent limit. Tyler and Thompson (1976) derive the following expression for the field amplitude:

$$\text{E304} \quad \psi(\mu,\nu) = CB^2 e^{ikz}\left\{1-A^*(\mu,\nu) - \frac{1}{2\lambda z}\exp[i(\frac{\pi R^2}{2\lambda z}-\frac{\pi}{2})] \times A(\frac{\mu}{2\lambda z},\frac{\nu}{2\lambda z}) + \frac{1}{\lambda^2 z^2}A(\frac{\mu}{\lambda z},\frac{\nu}{\lambda z})A^*(\frac{\mu}{\lambda z},\frac{\nu}{\lambda z})\right\}$$

where $R^2 = \mu^2 + \nu^2$ and C is the amplitude of the replay beam.

The second term represents the reconstructed image, the fourth term is small and is the intermodulation term. The third term gives the field propagating from the virtual image. When this is combined with the first term (and their complex conjugates) they yield a contribution identical with that of the image from a hologram made at a distance 2z. For an entirely real object the resulting intensity is:

$$\text{E305} \quad I(\mu,\nu) = C^2B^4\left\{1 - \frac{1}{\lambda z}\left[\sin\left(\frac{\pi R^2}{2\lambda z}\right)\breve{A}\left(\frac{\mu}{2\lambda z},\frac{\nu}{2\lambda z}\right)\right] + \frac{1}{4\lambda^2 z^2}\left(\breve{A}\left(\frac{\mu}{2\lambda z},\frac{\nu}{2\lambda z}\right)\right)^2 + A(\mu,\nu)^2\right\}$$

Evaluating E302 for an opaque disc of radius a yields:

$$\text{E 306} \quad I(x) = 1 - \frac{ka^2}{z}\sin\left(\frac{x^2k}{2z}\right)2\Lambda_1\left(\frac{kax}{z}\right) + \frac{k^2a^4}{z^2}\left[\Lambda_1\left(\frac{kax}{z}\right)\right]^2$$

where $\Lambda_1(x) = \frac{J_1(x)}{x}$

3.2.1 Limitations of Real Film

Using real film imposes two limitations on the recording, and hence the reconstructed image, of the hologram. Firstly the film size is finite and secondly it is an imperfect recording medium.

The finite aperture of the hologram imposes a limit to the maximum spatial frequency that can be recorded. Belz and Shofner (1972) considered the effect on the replayed image of the limited aperture of the hologram. They assumed an ideal film with a recording Modulation Transfer Function (MTF) of unity up to the limiting aperture of the hologram. Consider the geometry in figure 3.1; For a hologram of radius H, a circular opaque object of radius α, and wavelength λ, the intensity normalised to that at the

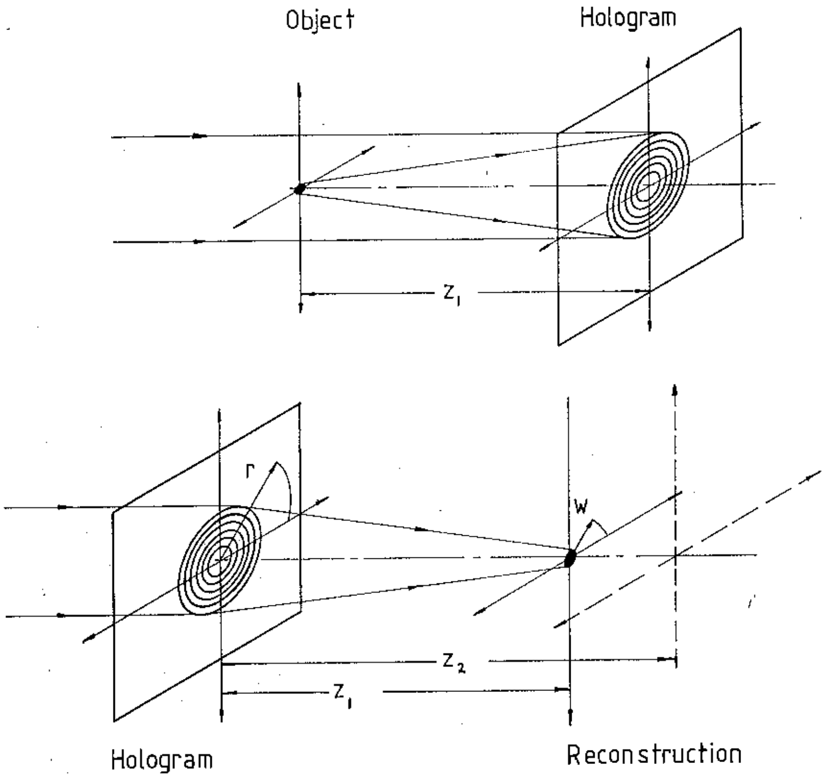

Figure 3.1 Recording and Replay Geometry after Belz and Shofner

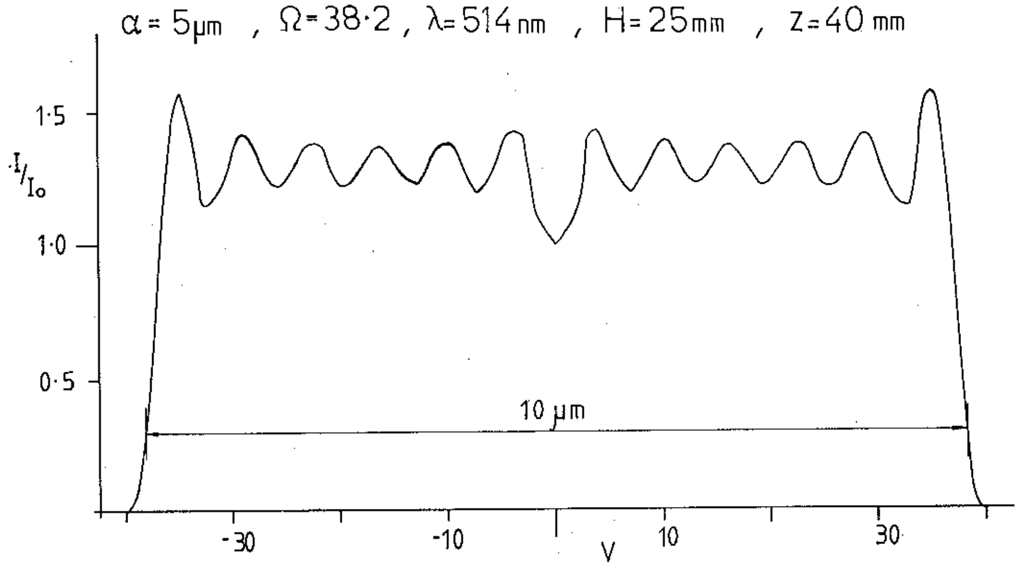

Figure 3.2 Focal Plane Intensity of a Reconstructed 10μm Disc

centre of the in-focus image is given by:

$$\text{E307} \quad I = \frac{\Omega^2}{[1-J_0(\Omega)]^2}\left[\int_0^1 J_1(\Omega\rho)J_0(V\rho)\cos\left(\frac{U\rho^2}{2}\right)d\rho\right]^2 + \left[\int_0^1 J_1(\Omega\rho)J_0(V\rho)\sin\left(\frac{U\rho^2}{2}\right)d\rho\right]^2$$

where $\Omega = \frac{k\alpha H}{z_1}$, $U = \left(\frac{kH^2}{2}\right)\left[\frac{1}{z_1} - \frac{1}{z_2}\right]$, $V = \frac{kwH}{z_1}$, $k=\frac{2\pi}{\lambda}$

Ω is the argument of the Bessel function at the upper limit of recording, thus it is indicative of the maximum amount of particle information recorded.

Equation E307 was evaluated for typical HOBC values of α, λ, H, and z. The results are illustrated in figure 3.2.

If the film is assumed to have an MTF of the form:

$$\text{E308} \quad \begin{array}{l} \text{MTF} = 1 \ , \ f < f(\text{cut-off}) \\ \text{MTF} = 0 \ , \ f > f(\text{cut-off}) \end{array}$$

then it can be seen that this has the same effect on the reconstructed image as a limited hologram aperture, thus (Tyler and Thompson (1976):

$$\text{E309} \quad f = \frac{r}{\lambda z} \qquad r(\max) = f(\max)\lambda z$$

Following DeVelis and Reynolds (1967), and considering a real film transfer function with an impulse response $s\,(\underset{\sim}{\beta})$ then the film records:

$$\text{E310} \quad I'(\underline{x}) = \int s(\underset{\sim}{\beta})\,I(\underset{\sim}{x}-\underset{\sim}{\beta})\,d\underset{\sim}{\beta}$$

In the case of a Fraunhofer hologram of an object $D\ (\xi)$ the image field becomes:

$$\text{E311} \quad \Psi(\alpha) = K\int D^*(\xi)\,s(\alpha-\xi)\,d\xi$$

taking the Fourier Transform of both sides (K is a constant):

E312 $$\widetilde{\Psi}(\mu) = K\widetilde{D}^{*}(\mu)\widetilde{s}(\mu)$$

that is to say the transfer function of the process is the transfer function of the film itself. DeVelis and Reynolds (1967) show that for the naive film MTF given in E308, and considering two point particles, the closest separation that they may have and still be separately resolved is:

E313 $$\xi \simeq 1/N$$

where N is the maximum number of lines per unit length that the film can record. The single point resolution can be defined as the reciprocal of the spot size from the zone lens in the plane wave limit, this is 1.64×N.

A major limitation in recording Fraunhofer Holograms is the low signal to noise ratio. As can be seen from E307 the contrast of the fringes decreases with increasing far-field distance, at some reference point the modulation is:

E314 $$M = \frac{2ka^2}{z_1}\Lambda_1\left(\frac{ka\,|x|}{z_1}\right)$$

$$M \simeq \frac{a^2}{z_1} \qquad \text{thus } a(\text{min}) \propto \sqrt{z_1}$$

In section 3.4.1 the differences in the recording of circular as opposed to linear objects will be discussed in terms of fringe visibility.

3.2.2 Coherence Effects in Holographic Recording

In the cases discussed above the recording and relay beams have regarded as ideal. That is they have been assumed to be totaly spatially and temporally coherent.

The effects of partial temporal and spatial coherence are considered in this section

3.2.2.1 Partial Spatial Coherence

In general it is extremely difficult to analytically determine the precise effects of partial spatial coherence as the relevant integrals cannot be solved for most coherence functions. The effect of partial spatial coherence is to reduce the size of the effective hologram from that given by the case of total coherence; it was shown in section 3.2.1 that this leads to a reduction in resolution.

3.2.2.2 Partial Temporal Coherence

DeVelis and Reynolds (1967) derive an expression for the intensity distribution at the hologram plane, neglecting terms quadratic in (λz), for the case of a source with a finite bandwidth approximated by the function:

E315 $$f(\nu) = \frac{1}{2\Delta\nu}\mathrm{rect}\left(\frac{\nu_0 - \nu}{2\Delta\nu}\right)$$

They showed that if $a\Delta\nu < \pi/18$ the expression became eqivalent to that obtained for totally monochromatic light, thus:

E316 $$\frac{\pi x^2}{cz} < \pi/18$$

Defining the coherence length $\Delta l \cong c/\Delta\nu$ then:

E317 $$x^2 < z\Delta l/18$$

Equation E317 defines the region within which the finite source bandwidth has no effect on the image. The limiting radius beyond which no interference will occur, due to a complete loss of temporal coherence, can be derived from geometric considerations:

E318 $$z^2 + x^2 = (z + \Delta l)^2$$

$$x \simeq \sqrt{(2z\Delta l)}$$

Equation E317 enables the achievable depth of field in in-line holography to be calculated. For a given resolution R, the zone lens must be recorded over an area given by inverting E309 and equating it with E317 in the case of equality.

E319 $$R = \frac{\lambda z}{2x} \quad , \; x^2 = z\Delta l/18$$

$$z = \frac{4\ R^2\Delta l}{18\lambda^2}$$

Thus the depth of field depends on the coherence length of the laser. Taking typical values of 5 micron resolution, a wavelength of 514 nm, and a coherence length of 100 mm the full depth of field is just over 2 m. Contrasting this with the classical incoherent depth of field (Born and Wolf (1980) p489) in an optical system operating at unit conjugate ratio shows the great advantage of holography. The acceptable focal tolerance in an aberration free system with a focal length f and lens diameter a is:

E320 $$\Delta z = \frac{8\lambda\ f^2}{\pi a^2}$$

At unit conjugate ratio, and for focal tolerances small with respect to the focal length, the depth of field in the object space is equal to the focal tolerance. From the Rayleigh resolution limit and with a small angle approximation

E321 $$R \simeq \frac{2f\lambda}{a}$$

For a resolution R of 5 microns and λ = 514 nm, $(f/a) < 4.9$. Substituting this value in E320 gives a half depth of field of 31 microns.

The ideal situation of only one mode oscillating is rarely encountered in practice. In a laser resonator of length L, the longitudinal modes are spaced by frequencies c/2L, where c is the speed of light in the lasing medium. The number of modes that can oscillate is determined by the number that lie under the laser gain profile and above the resonator loss curve.

For the Spectra Physics 162A argon-ion laser the gain curve has a width of about 5 GHz. The mirror spacing is 300 mm resulting in a longitudinal mode spacing of 500 MHz. Thus the output of this laser will consist of more than one mode, in this case probably around 7-8. This multimode output will have a large influence on the effective coherence length of the laser. Collier et al.(1971) show that for multimode operation the degree of coherence is given by:

E322 $$\mu(\tau) = \frac{\sin(Nc\pi\tau/2L)}{N\sin(c\pi\tau/2L)}$$

where there are N modes, of equal power, oscillating in a cavity of length L. The case of seven modes is shown in figure 3.3. Demanding that the degree of coherence is greater than $1/\sqrt{2}$ and defining a coherence length in the case of equality $L_H = c\tau_H$ gives, for the 7 mode system:

$$L_H = 0.4L/\pi$$

For the 162A laser the resulting coherence length is 38 mm, resulting in a value of x(max) = 55 mm

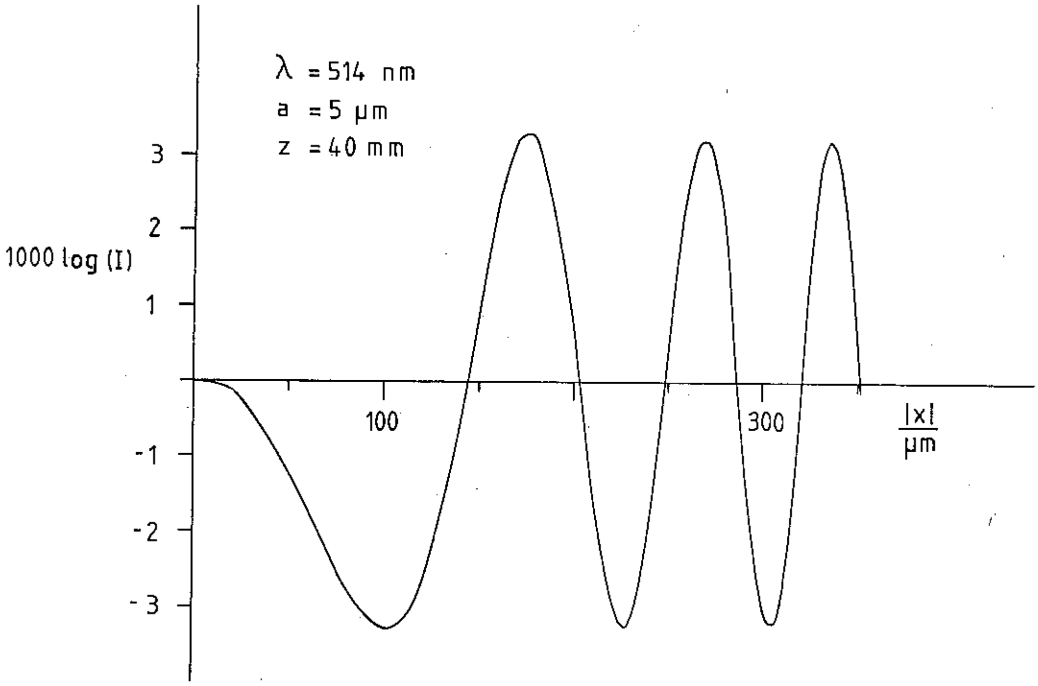

Figure 3.4 Hologram Plane Intensity Arising from a 10μm Disc

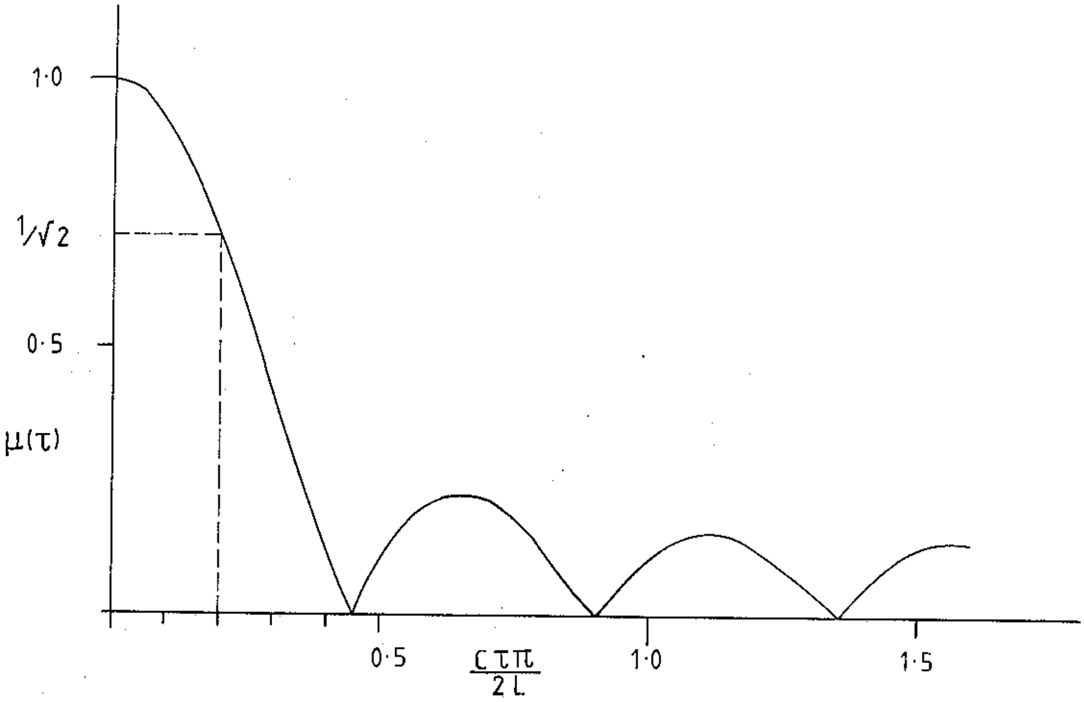

Figure 3.3 Degree of Coherence for 7 Longitudinal Laser Modes

3.2.3 The Effects of Turbulent Media

It is difficult to characterise the effects of turbulent media, the discussion by Yura (1973) suggests that in general a limiting of the useful hologram aperture can be expected, this will affect the resolution when it is greater than the aperture limiting effects of the film.

3.3 Aberrations of the Reconstructed Image.

In this section the third order aberrations of the hologram and magnification effects are briefly discussed.

3.3.1 Magnification Effects

The effects on the magnification of the reconstructed image, and their third order aberrations are discussed in the paraxial case by Meier (1965), and in the non-paraxial case by Champagne (1967). The paraxial case will be briefly discussed in this section. Defining μ as the ratio λ_2/λ_1 where λ_1 is the recording wavelength, and λ_2 is the reconstructing wavelength, the lateral magnification for a real image is shown to be:

E323 $$M = 1/[1 - \frac{(z_o)}{\mu z_c} - \frac{z_o}{z_r}]$$

where: z_r is the radius of the recording beam wavefront
z_c is the radius of the reconstructing beam wavefront
z_o is the location of an object point, $z_o < 0$

the hologram is assumed to be located in the plane $z = 0$. Thus only for collimated wavefronts will a recorded cuboid replay as a cuboid; that is, a magnification independent of z . Meier (1965) showed that the longitudinal magnification could be defined as:

E324 $M(\text{long}) = -M^2(\text{lat})/\mu$

thus if a hologram is replayed at a wavelength different from that with which it was recorded, the image space will be compressed by a factor $1/\mu = \lambda_1/\lambda_2$.

This effect puts a constraint on the collimation of the replay beam (assuming a perfectly collimated recording beam):

E325 $M = \dfrac{1}{1-z_o/\mu z_c}$ asssuming $\dfrac{z_o}{\mu z_c} \ll 1$

$M \approx 1 + z_o/\mu z_c$

Letting z be 0.1 m at most and with $\mu = 1$, if we require a maximum magnification difference between $z_o = 0.1$m and $z_o = 0$ m of 0.001, then z must be greater than 100 m.

Meier (1965) gives detailed formulae for calculating the five third-order aberrations. He showed that for one image (virtual or real) it is possible to eliminate all the aberrations by choosing collimated recording and reference beams and an appropriate off-axis reference point for the replay beam. The recording set-up used in NA25, and by those scanning machines that use the 514 nm line of the argon-ion laser, will tend to minimise the effects of these aberrations.

3.3.2 Film Effects

Yu (1973) considers the effect on the replayed image of non-linear recording of the hologram, and of the effects of emulsion thickness variation on the image aberations.

A photographic emulsion has a fairly small linear region in its TE (amplitude tranmsittance versus exposure) curve. If the reference wave amplitude is much greater than the amplitude of the object wave, Yu (1973) shows that for a point source object the bias exposure is independent of the intensity of the wave from the object. Thus the linear portion of the TE curve can be used by appropriately adjusting the magnitude of the reference wave. This situation was very closely approximated by the recording conditions in HOBC (Lecoq (1981)).

The effect of non-linear recording in in-line holography is to generate higher-order images located at focal lengths $f = R/n$ $n=2,3,4...$ where $f = R$ is the focal length of the primary real or virtual image zone lens. The irradiances of the high-order reconstructions vanish in the case of extreme linearity.

Thickness variations in the emulsion do not in general affect the recording of the hologram, however Yu (1973) discusses the effect that a non-uniform emulsion thickness would have on the replayed image. He considered an emulsion phase delay approximated by a second order polynomial in the x,y plane containing the emulsion surface:

E326 $$\Phi(x,y) \simeq b_0 + b_1 x + b_2 y + b_3 x^2 + b_4 y^2$$

where $b_0, b_1 \ldots$ are arbitrary real constants. In the case of all the coefficients higher than $b_0 =$ zero then the image reconstruction is unique. If the quadratic terms (b_3, b_4) are zero, a perfect wedge, then the reconstruction will also be unique, but the image will be laterally translated. In this simple model some astigmatism will be present in the reconstructed image if $b_3 \neq b_4$. If $b_3 = b_4$ and both are non-zero, the image will show no astigmatism, but it will be distorted with respect to the object. The emulsion then introduces a phase delay similar to that given by a thin lens, with the real lateral magnification given by:

E327 $$M(\text{lat}) = \frac{R}{R + Z(\eta - 1)}$$

where R is the radius of the emulsion surface, Z is the object-hologram distance, and η is the refractive index of the emulsion. For an emulsion surface that is not entirely flat the lateral magnification will vary with object depth.

3.4 Image Structure and Spatial Filtering

3.4.1 The Effect of Object Shape

The shape of the object to be recorded has a considerable effect on the resolution utimately obtained. For most emulsions used in holography the modulation depth of the signal is a more critical parameter than its spatial frequency. Dunn and Thompson (1982) showed the effect on resolution of object shape, and hence fringe visibility, for simple geometric shapes. The visibilty of the fringes arrising from a one-dimensional thin strip (or, in practice, a thin wire) is much greater than the visibility of the fringes from a circular object of similar diameter, except for a small object to hologram distance. In the case of HOBC, recording a 10 micron bubble at around 40 mm, the visibility of the fringes from a 10 micron wire are about a factor of 30 greater than those from a bubble at the centre of the hologram. The reconstructed hologram will show a higher resolution, and greater edge actuance, in the case of the wire. Wires, although simple test targets, are somewhat inappropriate for testing the feasibility of in-line holographic recording schemes. In the early days of holographic bubble chambers, thin wires were invariably used to assess system performance (see RAL (1981)). The reality, that of small opaque discs, has always resulted in lower resolution or poorer contrast that that expected from these tests. The form of the diffraction pattern accounts in part for this. In a well chosen recording set-up, with adequate laser coherence, film resolution, and film size,the resolution is limited by the low-contrast response of the film. For a typical HOBC recording, with bubbles of 10 micron diameter at a distance of 40 mm from the film and with a wavelength of 514 nm, the maximum fringe visibility is about 0.007. Figure 3.4 shows the diffraction pattern for this case, assuming perfect laser coherence.

Following Belz and Shofner (1972), and assuming a film MTF of the form described in E308 with a cut-off frequency of 1500 lines/mm, I have calculated the intensity in the vicinity of a replayed real image of a hologram of an opaque disc of 5 micron radius at a distance of 40 mm from the hologram, and with a wavelength of 514 nm. The results were calculated using E307, the integrals were evaluated using a 24 point Gaussian Quadrature technique; they are shown in figure 3.5.

Figure 3.5(a) shows the intensity in the focal plane of the replayed disc, and is to be compared with figure 3.2 .

It can be seen that the intensity along the bubble diameter is very different from the case of ideal (but finite) film. The value of Ω used in the calculations indicates that around two zeros of the modulating Bessel function are being recorded on the film, compared to nearly 12 zeros in the case of fig. 3.2. It is interesting to note the drop in intensity at the centre of the image, this would give the in-focus disc a distinct doughnut appearance. Figures 3.5(b) and 3.5(c) are at distances 50 and 100 microns away from the focus in a direction away from the hologram. In fig. 3.5(c) the intensity of the image at the centre of the disc is about four times that of the in-focus case. Figure 3.5 illustrates the difficulty in accurately locating the image plane of the disc. There is a natural tendency to focus on the "brightest" image, and this will almost never coincide with the true focal plane. It can also be seen that the apparant width of the bubble has not changed in going from fig. 3.5(a) to 3.5(b). In general the best indicator for accurate focussing is the apparent edge sharpness; it can be seen that the initial slope of the

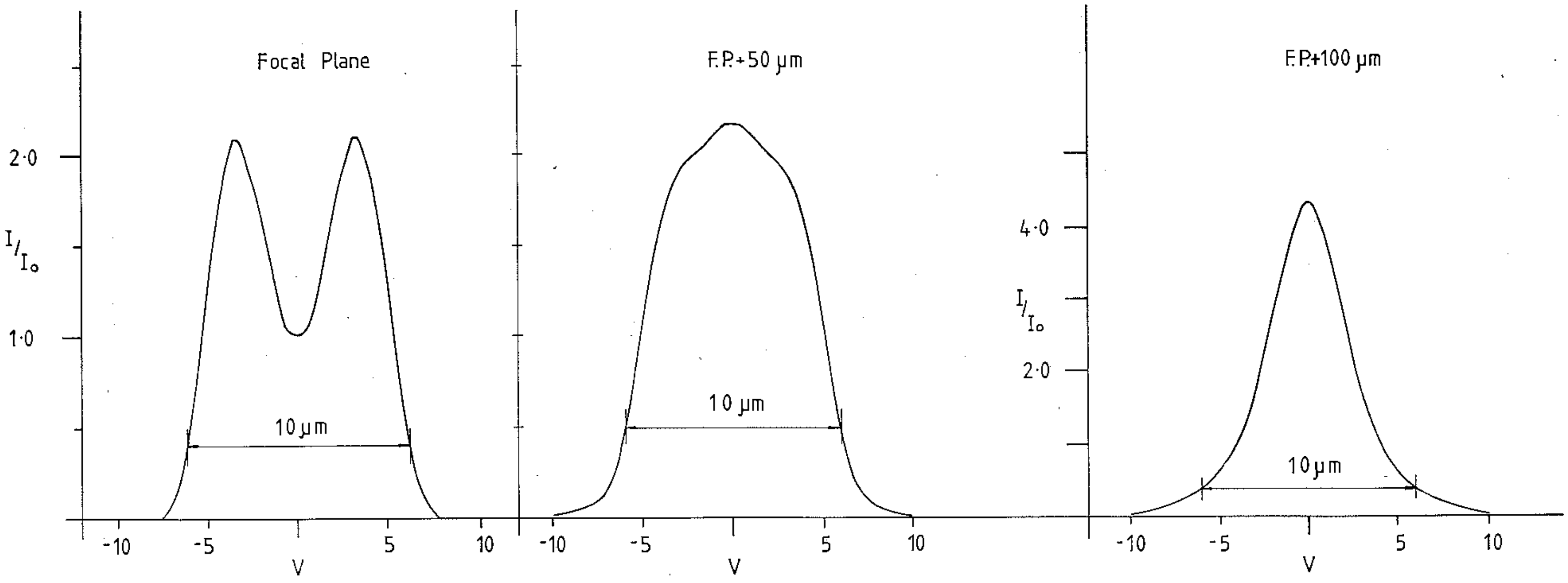

Figure 3.5 Variation of Intensity with Distance from the Focal Plane of a Reconstructed 10µm Disc

image is steepest in the case of the in-focus image. It is important to use edge sharpness rather than brightness if focussing errors are to be minimised.

In a real scanning machine the replayed images are viewed via an optical system with a finite frequency cut-off, thus the images viewed on a TV camera will be given by the convolution of the system impulse response with the image. This will reduce the visible differences in structure, and will result in even poorer depth resolution

3.4.2 The Fourier Transform Properties of a Lens

In the preceding discussion the recording and replay of the hologram has been assumed to occur directly with no intervening lens system. In discussing the use of spatial filtering, and the effect of an imaging system the Fourier Transforming properties of a lens must be considered.

It can be shown (Goodman (1968)) that a simple lens acts on a complex amplitude incident upon it, multiplying it by a quadratic phase factor. Solving the equation for the amplitude in the rear focal plane of the lens gives the important result that it is equal to the Fourier Transform of the object distribution (neglecting a constant phase factor). In the general case the Fourier Transform is preceded by a quadratic phase factor, but this vanishes for the case of an object in the front focal plane, leaving an exact Fourier Transform relationship.

3.4.3 The Effect of a Finite Lens Aperture

A lens with a finite aperture introduces a limit to the resolution obtainable in the recording of a hologram, or in the imaging system used to view the reconstructed image. In the HOBC recording system a lens system was used to transfer the image to a more accessible plane for holography.

Considering a lens with a finite aperture, Goodman (1968) defined the coherent transfer function H as the Fourier Transform of the impulse response, and showed that it is simply related to the pupil function:

E328 $$H(f_x, f_y) = P(-\lambda d_i f_x, -\lambda d_i f_y)$$

In an aberration free system P = 1, or 0 only; this implies a finite passband within which all frequencies are transmitted without phase or amplitude distortion. At the boundary the response drops to zero. The cut-off frequency is defined by:

E329 $$f_o = r/\lambda d_i$$

where r is the lens radius, and d_i is the distance from the rear surface to the plane of interest. The ERASME lens in the transfer system (f = 300mm, f-number = 2.8) when used at unit conjugate ratio has a cut-off frequency of 175 cycles/mm at 514 nm. The field lens had a frequency cut-off at around 150 cycles/mm. The combined system response cannot be obtained simply as it depends on the aberrations of the individual lenses. The overall MTF of the lens-film combination will be given by the product of the lens MTF and the film MTF, and, for a well corrected system, will be approximately the film MTF truncated at the cut-off frequency of the lens system.

3.4.4 Spatial Filtering

The existence in a coherent imaging system of fixed planes containing the Fourier Transform of the object-space distribution allows image-space spatial filtering to be performed. Various techniques can be used, they are briefly summarised below.

1) Amplitude filter: the simplest amplitude only filter is the binary filter, with a transmittance of 0 or 1. These are easily made on film, or by using opaque stops. Continous tone filters can be made with photographic film, but are much more complex to design and use.

2) Phase filters: binary phase filters are useful for realising some mathematical operations, for example Hilbert transform and differentiation.

3) Complex valued filters: this filter is capable of the greatest variety of filtering operations: matched filtering, multiplication, subtraction etc. The disadvantage is the complexity of construction and, for most filters, the result of the operation appears in an off-axis sideband. This filter is capable of very complex operations matched to the original object (Vander Lugt (1974)) but its complexity prevented any tests with this form of filter.

Early work with the HOLMES machine by Drevermann and Geissler (1982) showed that spatial filtering of the images was of considerable help in reducing the effects of old tracks. This was especially useful with holograms from the first data taking run of HOBC in 1981 as the old tracks were much larger than those in the 1982 run. Simple binary amplitude high-pass filtering removed most of the image from these large tracks, while leaving the small in-time tracks unaffected. The contrast was also enhanced due to a reduction in the intensity of the uniform background. This form of filtering has not proved to be of much benefit on CHIMAERA with film from the second run, I believe this to be due to two effects:

1) All tracks were more or less the same size, and thus old tracks do not interfere significantly with the event of interest.

2) One of the major effects of spatial filtering in HOLMES was to remove the noise generated by the many optical surfaces in the complex light imaging paths. CHIMAERA had a very simple optical layout with a minimum of surfaces, all of which were coated. The images produced in the absence of film were much cleaner than those of HOLMES, and were not much improved by filtering.

It is possible that size-selective filtering, as discussed by Hutzler (1977), or complex matched filters (Vander Lugt (1974)), might enhance the image. These filters would, however, render the fiducials invisible, thus requiring a separate unfiltered light path and increasing the complexity of the machine.

CHAPTER 4 THE CHIMAERA SCANNING TABLE

In the early stages of the holographic bubble chamber experiment NA25, considerable activity was taking place in many institutions regarding the design of suitable scanning machines.

Early work at the RAL, by Lutz in Strasbourg (Lutz (1982)), and Drevermann in CERN (Drevermann (1982)), had highlighted the major parameters to be considered. The approach at RAL and CERN was to adapt existing scanning machines possesing precision X and Y stages, modifying them to allow video imaging of the reprojected holograms with an additional Z stage. RAL chose a "Vanguard" machine and CERN a "Spiral Reader". Unfortunately the machine at RAL never progressed beyond a test set-up, and it is from the work of Drevermann and, to a lesser extent, Lutz that I derived my optical design principles.

4.1 Options for Holographic Scanning Machines

The general principles of holographic replay have been discussed in chapter 3. Once the real (or virtual) image has been reconstructed there are three basic layouts that an analysis machine can take:

1) Direct projection onto a conventional table

2) Direct ocular microscopy

3) Indirect TV camera microscopy

The first method is very simple, and existing tables with Mangiaspago (or similar) digitisers can be easily modified. It enables quite a large region of the hologram to be seen in great detail, and allows sensitive kink and multiple scattering detection. It has a high resolution, with few optical elements to degrade the image. However this method has three disadvantages. To project onto an area of 1 square meter requires a laser providing around 0.25 W at 514 nm, this is expensive and potentially highly hazardous. The speckle in the image may be unpleasant for some scanners, and cannot easily be removed. Finally there is evidence of long term damage to the retinal cones from continuous exposure to low levels of green or blue light.

The machine at Brussels (Barth et al.(1983)) in the NA25 collaboration was the only production machine to use the direct projection technique. This table used direct projection onto a large horizontal plane surface, in a manner similar to a conventional scanning machine. The hologram was held on a support mounted on a precision X-Y-Z stage assembly; each stage was digitised to a precision of 1 micron. The expanded beam from a high power argon-ion laser tuned to 514 nm was passed through the hologram, and the image was projected with a magnification of 84 onto the table. Typically a laser power of 200 mW was used for comfortable scanning. The image seen by the operator was 700 by 1800 mm in extent. The table electronics were controlled in a manner similar to the CERN Bessymatic system, using an intelligent CAMAC crate controller; the host computer was a DEC-20.

The second method has the advantage of low laser power and high resolution, but is more complex, cannot easily detect kinks, and is too hazardous.

The third method was the one used in all the other production machines in the collaboration, and was the approach chosen for the CHIMAERA machine.

4.1.1 Experience from the "HOLMES" Machine

During the early stages of design only one machine, the HOLMES (I) at CERN designed by Drevermann and Geisler, had attempted to do any significant production scanning. Considerable notice was taken of the experience gained in the HOLMES project during the design of CHIMAERA. It was clear that a basic scanning machine would require:

1) Three orthogonal stages each with a travel of greater than 100 mm , each stage digitised to better than 5 microns resolution.

2) A single point optical resolution better than 10 microns.

3) At least two co-axial views of the event with differing magnifications, showing approximately 10 by 7 mm and 1.4 by 1 mm respectively.

4) A helium-neon or, preferably, an argon-ion laser with a power of about 10 mW in a single laser line.

5) Accessible Fourier Transform planes for spatial filtering.

In addition it was clear from the nature of the interactions being studied that some form of anamorphic magnification expanding the transverse momentum direction was desirable. Drevermann and others had shown that commercially available 1" vidicon camera tubes were suitable imaging devices. From the experience I gained while using the HOLMES machine, and from my own optical bench tests, it was clear that minimising the number of optical surfaces in the light paths was beneficial. This was difficult to achieve in a modified scanning machine, as the available machines usually imposed undesirable constraints on the light path. Lecoq and Olivier (1981) had shown that the best film clamp was by vacuum hold-down onto an optical flat.

4.1.2 Existing Hardware for CHIMAERA

When I undertook the completion of CHIMAERA, parts of the machine had already been built or ordered. These imposed additional constraints to the design. In existence were:

1) A Spectra-Physics 162-08A argon-ion laser with a maximum power of 16 mW at 514 nm

2) Three Anorad ANORIDE 5-4 stages, and their electronics.

3) The film holder and film transport.

4.2 The Stages and Associated Electronics

The stages chosen for CHIMAERA were ANORIDE model 5-4 stages. These were chosen before the optical system had been designed, and their ability to rapidly move large masses was considered an important characteristic. Their main features are summarised in table 4.1

The stages were made from precision machined "Mehanite" castings, and used a precision leadscrew and crossed roller bearing slides. The stages were driven by ANORIDE motor drive cards, and controlled by high resolution axis cards. The axis cards contained phase-shifting circuitry allowing interpolation to 1 part in 20 between the grating lines, achieving a resolution of 2 microns with the ME1 encoder. Following this circuit was an Analogue-to-Digital converter, and associated data latches. This allowed the microprocessor to directly read the stage postion via a data bus.

TABLE 4.1
MAIN FEATURES OF THE ANORIDE 5-4 STAGES

Mass	8 kg	
Maximum Load	45 kg	
Accuracy	± 4 μm/25 mm	max error ± 20 μm/300 mm
Straightness	± 1.6 μm/25 mm	max error ± 10 μm/300 mm
Motor	Torque Systems C-Line Motor-Tachometer 2120 Maximum Continous Torque: 0.27 Nm Peak Torque: 1.4 Nm	
Tachometer	Voltage Linearity : at 3600 rpm ± 0.05%	
Encoder	Linear Nichrome/glass type ME1 (25 lines/mm)	

The encoder carried masks to set the two electronic stage limit positions, and to indicate the approximate Home (coordinate zero) postion. Home encoder gratings were placed every 25 mm along the linear encoder, and allowed an absolute reference point to be transmitted to the microprocessor. A unique Home position was indicated by the mask.

The speed and acceleration of each stage was set by gain and feedback potentiometers on each drive card; once set the, speed was digitally controlled via the axis card D-to-A converter. The stage speeds actually used during scanning were:

SLOW	115 μm.s^{-1}
FAST	13.8 mm.s^{-1}
COORDINATE MOVE	30 mm.s^{-1} (max)

4.2.1 The Microprocessor

All three axis cards were driven from an 8085 based microprocessor designed and built at UCL by Dr G.Lush. This used the 8-bit 8085A microprocessor to control the stages, and to transmit and receive data from the DEC PDP 11/44 minicomputer via a CAMAC crate. The microprocessor used 8255 programmable peripheral interfaces (PPI) to transmit and receive data from the CAMAC crate and the Anorad axis cards. The microprocessor contained 16 K of EPROM (2716 EPROM), and used a small amount of RAM as scratch-pad memory (HM6116 RAM). One PPI was connected to the ANORIDE crate containing the three axis cards, each of which was accessed when the appropriate control word was sent. The microprocessor was connected to four NE 9017/2 24-bit input/output drivers (Nuclear Enterprises) by the remaining four PPI's. Three of the 9017/2 units were used for coordinate and velocity data, one for each stage, the remaining 9017/2 was used to transmit control information from the PDP 11/44 computer, via the CAMAC crate, to the microprocessor. The program running in the microprocessor is discussed in chapter 5, section 5.3. The 8085 could also be accessed via a RS232 interface, allowing the stages to be directly controlled. This was very useful for testing purposes.

4.2.2 The CAMAC Crate and PDP 11/44 Computer

The CAMAC crate was controlled by a Fisher MXCTR-3 crate controller, and a GEC LG2401 LAM grader. It was directly connected to the PDP 11/44 computer backplane via a UNIBUS cable and a Fisher PTI 11D-2, PTI 11C-2 UNIBUS interface. The crate contained five NE 9017/2 I/O drivers, the fifth of which was connected to the operators keypad via a key decoder and data latch. This allowed the operator to communicate with the PDP 11/44 via the CAMAC crate,and was used to control the stage driving routines. Four switches on the keypad were used to control the film transport, and were not connected to the key decoder/latch.

The Digital Equipment Corporation PDP 11/44 minicomputer was fitted with 256 K-words of hardware memory and the FP11-F Floating Point Processor. It had two RL02 disk drives, each disk holding 10.5 M-bytes of data. The RS232 interfaces were via a DZ-11-A asynchronous multiplexer which provided eight lines at speeds up to 9600 baud.

A Cifer 2634 VDU was used by the operator to control CHIMAERA. This VDU was programmable,and could emulate a DEC VT52 or run graphics in Tektronix 4016 compatible mode. It had high-resolution graphics (1000 by 300 pixels) and eight pages of screen memory.

Figure 4.1 shows schematically the connections between the stages and their control electronics.

4.3 The Film Transport

Tests carried out by Lecoq and Olivier (1981) showed that the best film support was provided by vacuum hold-down onto an optical flat. Unfortunately this resulted in the loss of a small part of the edges of the film; in CHIMAERA two strips 5 mm wide were rendered invisible. Lecoq and Olivier (1981) also showed the necessity of minimising the tension applied to the film.

4.3.1 The Reel Tables

There were two identical reel tables, each comprising a reel holder driven by a geared down motor, a tension control arm, and two idler wheels. A DC printed circuit motor drove a reducing timing belt chain to provide the necessary torque. The tension on the film was adjusted during stage movement by an idler wheel on a movable arm

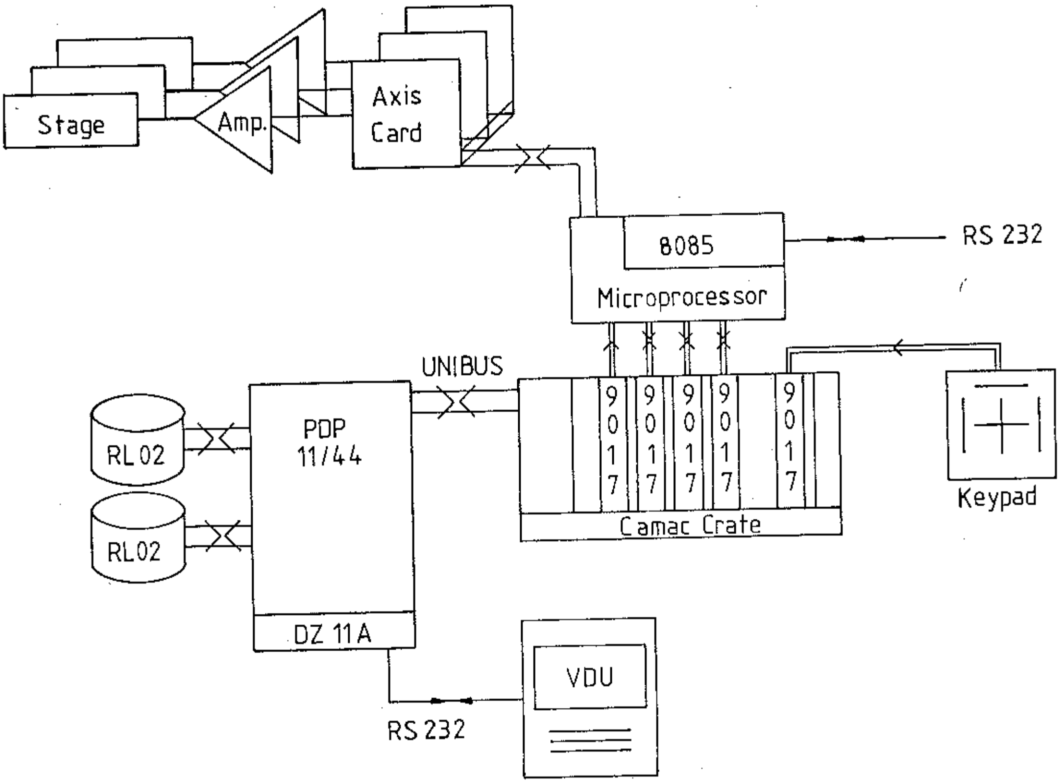

Figure 4.1 Schematic Diagram of the Computer, Microprocessor, and Stage Electronics

linked to a feedback potentiometer. At each end of its movement a shaped sector attached to the arm activted an opto-electronic limit switch. The motors were driven by identical bipolar power amplifiers, each capable of providing 100 W. The output voltage from the amplifier was determined by an analogue input to each amplifier. This voltage was derived either from the feedback potentiometer attached to the tension arm, or, during film transport, from preset film-winding voltages.

4.3.2 The Film Holder

The film was held onto an optical glass plate by vacuum along a rectangular border of 110 by 50 mm. The glass plate was coated on both sides with an anti-reflection coating of MgF_2, optimised for minimum reflectance in green light. The supporting aluminium frame was black anodised. The film holder carried two pairs of idler wheels at each end of the glass plate, these touched the film only at its edges to minimise scratching. An optical system to separately illuminate the frame number was mounted onto the film holder. The minimum film bending radius was 20 mm.

4.3.3 The Vacuum System and Control Electronics

A small oilless rotary vacuum pump (Edwards ECB1) provided the vacuum to hold down the film. When film winding was in progress a system of solenoid valves reversed the air flow and pushed air out of the holes in the film holder to provide an air cushion for the moving film. The entire assembly of pump and valves was acoustically and mechanically isolated from the main CHIMAERA table to eliminate vibration.

The film winding was controlled by four of the switches on the operators keypad. The depression of any switch reversed the air flow to the film holder releasing the film. The appropriate voltages (positive or negative and high or low) were sent to each reel table motor. When the switch was released the film was held against the plate by the vacuum, and the tension was controlled by feedback from the tension arms, this allowed the correct film tension to be maintained during movement of the X or Z stages.

4.4 The Optical System

The quality of the optical system of a holographic film analysis machine plays a major part in enabling events to be recognised and accurately measured. Certain of the five third-order (Seidel) aberrations were more important in this context than others. The polychromatic aberrations, such as longitudinal and lateral chromatic aberration, were unimportant since monochromatic illumination was used; however in commercial multi-element lens designs it was important to consider the compromises that had been made in order to minimise these chromatic aberrations.

4.4.1 Aberration Considerations

The monochromatic aberrations fall into two groups; in the first group are coma, astigmatism, and spherical aberration. These cause a deterioration of the image, making it less "clear". In the second group are Petzval field curvature and distortion; these deform the image.

Spherical aberration can be reduced by reducing the lens aperture, but this will degrade the resolution. The CHIMAERA optical system required an f-number greater than 8 in order to adequately resolve 10 micron objects. It was thus essential that the lenses used were well corrected for spherical aberration at their maximum aperture.

Coma is a distortion which is important even for object points close to the optical axis. Although relatively unimportant for measuring, which was done on-axis, it would have led to a degradation of the image away from the axis, reducing the ability to recognise important features of the image.

Astigmatism was not a great problem, as it is only significant for points away from the optical axis.

Field curvature and distortion were acceptable in small amounts.

4.4.2 The Lenses

The most important feature of any lens that was to be used in CHIMAERA was a minimum of coma and spherical aberration at large apertures. Commercial multi-element lenses with good on-axis performance at large apertures are easily obtainable. However experience gained from tests carried out with Pentax 50 mm F1.8 lenses showed that image degradation, arrising from dust and residual reflections from the many surfaces, was a considerable problem. In incoherent imaging, dust and surface reflections tend initially to reduce the overall contrast of the image. In a coherent system, large interference patterns of high contrast are generated which cause considerable interference to the primary image. These considerations lead to the design principle of minimising the number of surfaces between the hologram and the camera tubes, while maximising the on-axis performance of the system. The lenses had to be doublets at most, and all surfaces had to be anti-reflection coated.

The LAO series of computer optimised achromatic doublets from Melles Griot offered the flexibility of choice coupled with the performance that was desired. The LAO series were cemented doublets designed to maximise the polychromatic field-averaged MTF. When used at an infinite conjugate ratio, they were almost entirely free of spherical aberration and coma. Their performance was almost uniform up to a field angle of 2.5° The important parameters of the lenses used are given in table 4.2.

TABLE 4.2
LAO SERIES ACHROMATIC LENSES

General
Material: Grade A annealed flint and crown
Surface Quality: Scratch and Dig 60-40
Centration: 3' of arc
Surface accuracy: $f/D < 3.0$ $\lambda/2$ (Hg green)
$f/D > 3.0$ $\lambda/4$ (Hg green)

Coating: 0° MgF_2 at 550 nm

Lens	Focal Length	Diameter	Focal Radius	t(c)	t(e)
LAO 014	21	14	10.20	8.1	5.8
LAO 059	50	18	19.48	6.0	4.2
LAO 167	175	25	67.01	5.5	4.7
LAO 177	180	40	69.03	9.6	7.2

NOTE: All measurements are in mm; t(c) and t(e) are the centre and edge thickness, Focal Radius is the radius of the rear focal surface at infinite conjugate ratio.

4.4.3 The CHIMAERA Optical System

The LAO series achromats were designed to be used at small field angles and at infinite conjugate ratios. A finite conjugate ratio can be achieved by selecting two lenses with the desired focal lengths, orienting them with their most curved surfaces facing each other to minimise spherical aberration, and locating the object and image in the focal planes. Considering a general system of two lenses in the thin lens and paraxial approximations, the transfer matrix for the overall system is given by:

E401 $$T = \begin{pmatrix} 1 & x_3 \\ 0 & 1 \end{pmatrix} \begin{pmatrix} 1 & 0 \\ -1/f_2 & 1 \end{pmatrix} \begin{pmatrix} 1 & x_2 \\ 0 & 1 \end{pmatrix} \begin{pmatrix} 1 & 0 \\ -1/f_1 & 1 \end{pmatrix} \begin{pmatrix} 1 & x_1 \\ 0 & 1 \end{pmatrix}$$

where x_1, x_2, x_3 are the spacings between the object and lens1, lens1 and lens2, and lens2 and the image respectively. Letting $x_1 = f_1$ and $x_3 = f_2$ the product of these matrices reduces to:

E402 $$T = \begin{pmatrix} -f_2/f_1 & 0 \\ \dfrac{x_2 - f_1 + f_2}{f_1 f_2} & -f_1/f_2 \end{pmatrix}$$

Element m(12) of the matrix is zero indicating that the object and image planes are conjugate, the magnification is given by the element m(11). These results are independent of the value of x_2, the separation between the lenses. Thus, subject to the constraints of vignetting, the separation between the lenses can be varied with no change in the paraxial properties of the system.

4.4.3.1 The Laser Beam Expander

The laser beam produced by the Spectra Physics 162-08A laser had a beam width of around 1mm. The design of the film transport, and the layout of the stages required that the film be illuminated across its whole visible width. Thus the beam expander had to consist of an afocal telescope with a magnification of about 40. This was achieved using a Cooke microscope objective (f = 4mm, NA = 0.65), and a doublet lens of overall focal length f = 330mm and F-number 8.3. The doublet was an air spaced combination of a symmetric biconcave lens and a planoconvex lens. The air space was chosen to minimise the spherical aberration in the output beam. A spatial filter in the form of a 12.5 micron pinhole was placed near the focal point of the microscope lens. This acted as a low-pass filter, removing high frequency "noise" generated by dust in the objective. The microscope objective and the pinhole were mounted in adjustable mounts to enable them to be aligned to the laser beam and to each other. The output beam was collimated to within 250 microradians by adjusting the focus of the expander doublet.

4.4.3.2 The Imaging Optics

The design of the imaging system was constrained by the following factors. The desire for a minimum of surfaces has already been mentioned, the other major considerations were:

1) The need for a region in which the physical separation of two lenses would not affect the location of the object or image planes. This required the optical configuration discussed in section 4.4.3

2) The field angle subtended at each lens to be minimised

3) The existence of physically accessible planes containing the Fourier Transform of the object distribution.

4) Simplicity of mechanical mounting, combined with maximum rigidity and ease of adjustment.

Constraint 1) also allowed for the later introduction into the light path of a Dove prism. This allowed an optical kink detection technique inspired by Drevermann (1981) and Lutz (1982) to be used. The choice of focal lengths and diameters of the optical components was in part determined by considerations of vignetting of the image rays. The largest Dove prism available had a square entrance aperture of 20 by 20 mm. This led to the choice of a relatively long focal length for the first lens. To ensure unit magnification the lenses following the cubic beam splitter were of a similar focal length. Their diameters were larger to avoid vignetting the primary image. The optical system was designed to allow unobstructed viewing of a region 10 by 10 mm in the object space. The optical layout of CHIMAERA is shown in figure 4.2, and the ray paths and apertures in figure 4.3.

The object was imaged at infinity by the 175 mm lens. This lens and the first mirror were mounted on the vertical stage, which allowed the film to be scanned across its width. The lower fixed mirror returned the light path to the horizontal where it was divided by a cubic beam splitter of 30 mm aperture (Melles Griot 03 BSC 011) to form the low and high magnification paths. Close to the two exit faces of the beam splitter were 180 mm lenses forming real images of the object in their rear focal planes with a magnification of -1.03. The low magnification image at this plane could have been imaged directly onto the vidicon, but in order to allow for spatial filtering it was transfered at unit magnification by the 50 mm lens. This LAO achromat was no longer being used at its design conjugate ratio, but it did provide a better image than a symmetric biconvex lens, and produced a greatly superior Fourier Transform in its rear focal plane. In the high magnification light path a 21mm lens was used to magnify the image by a factor of about 7.5. The LAO 014 achromat worked well at this conjugate ratio.

All five lenses were coated with a single layer of MgF_2

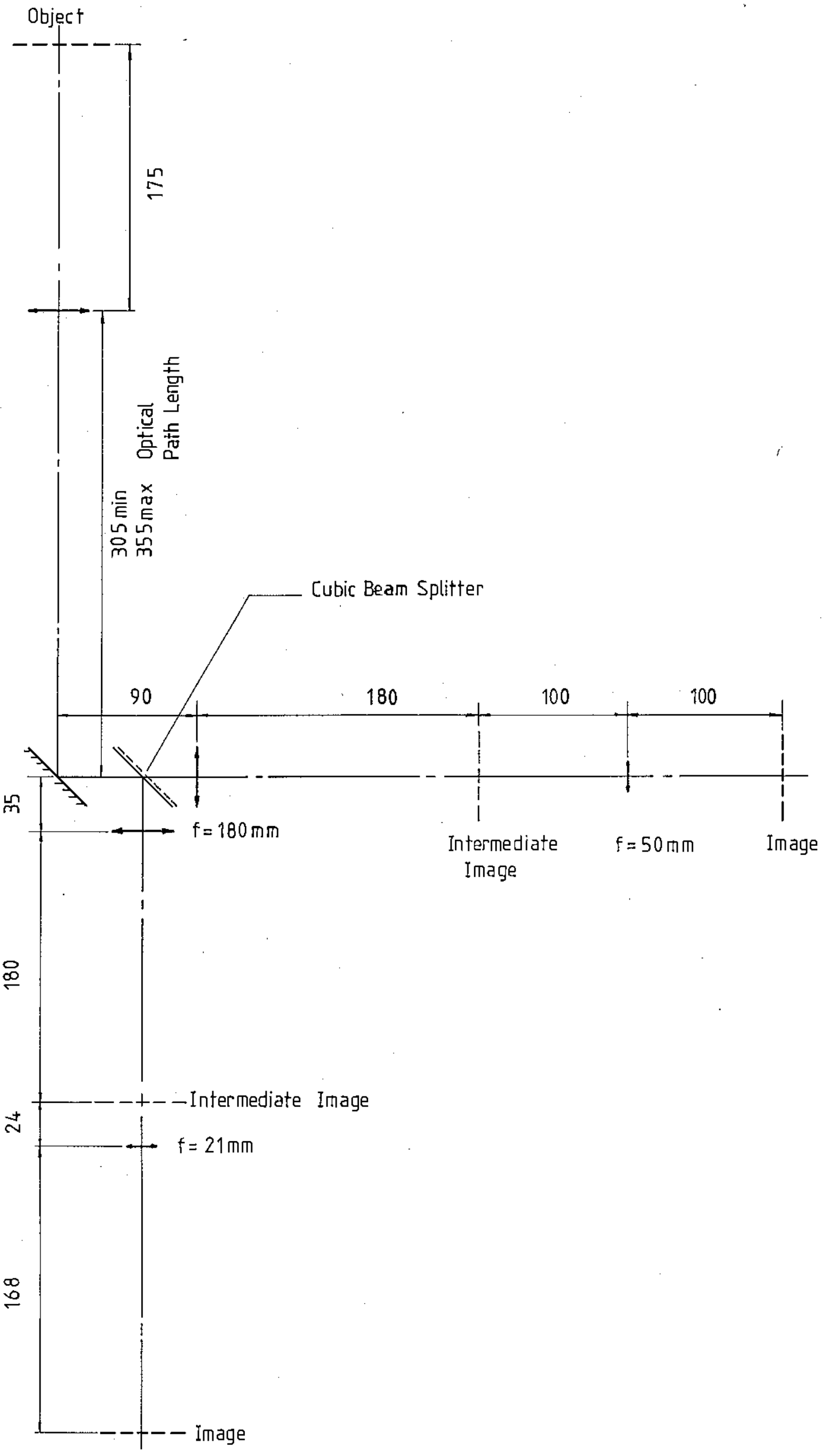

Figure 4.2 Plan View of the CHIMAERA Optical System

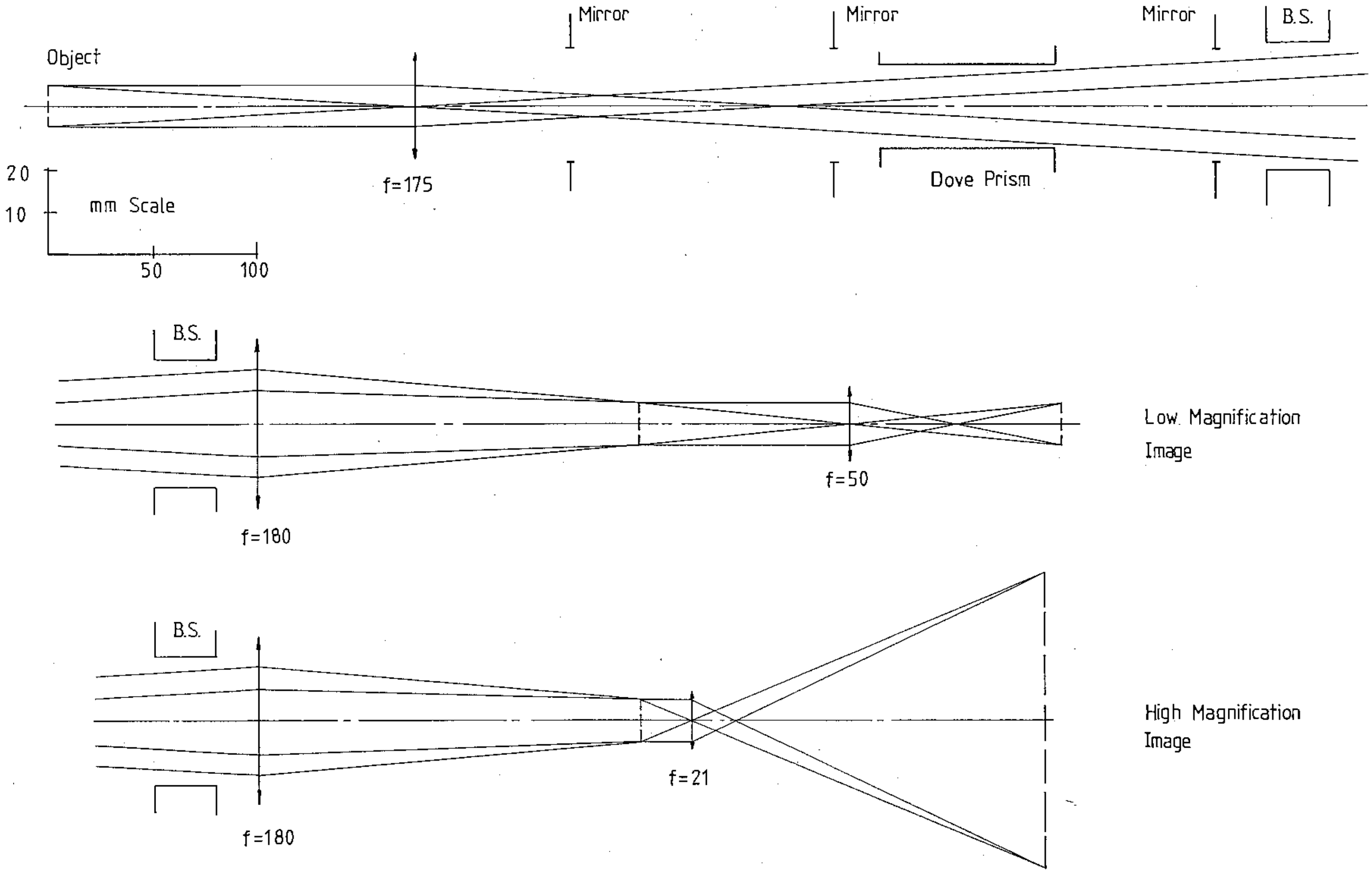

Figure 4.3 Ray Diagram of the CHIMAERA Optical System

whose thickness was optimised for minimum reflectance at 550 nm. The surface reflectance at 514 nm was 1.3% for normal incidence. The cubic beam splitter had a transmittance and reflectance of 44% and 52% respectively. The entrance and exit faces were HEBBAR coated, resulting in a reflectance of 0.4% at normal incidence. The Dove prism (20 mm aperture, Melles Griot 01 PDE 005) which could be inserted in the light path between the second mirror and the beam splitter, was also HEBBAR coated. The mirrors were 38 mm square, 10 mm thick with a Pyrex substrate. The surface was flat to $\lambda/4$. To maximise the reflectance the mirrors were coated with MAXBRITE, with a polarisation averaged reflectance of 99.3% at 45° and 514 nm. This coating was unusually robust, and possessed a high heat and moisture resistance. The overall light losses were 11%; of which 9% came from the lenses and beam splitter, and 2% came from the mirrors. Had ordinary aluminium coated mirrors been used the losses due to the three mirror reflections would have increased to 27%

4.4.3.3 Mounting the Optics

The LAO achromats had radii of curvature which were reasonably large, especially on the less curved face. This allowed the use of a fairly simple design of lens holder, in which the lens was located by its edges and held by a threaded brass ring. Figure 4.4 shows the lens holder for the LAO 167 lens. This design was entirely successful provided that the rear lens surface was not too steeply curved. The four stationary lenses were then mounted on Ealing miniature dual axis stages (35-1718), each with 10 mm of travel in two orthogonal directions. This allowed precise allignment of these lenses with ease. The cubic beam-splitter was mounted in a frame of my own design, which was fixed to a miniature rotating stage (Ealing 35-1742). The mirrors were fixed to mirror mounts which allowed angular rotation of the mirror about two axes lying near the plane of the mirror. The optical elements, other

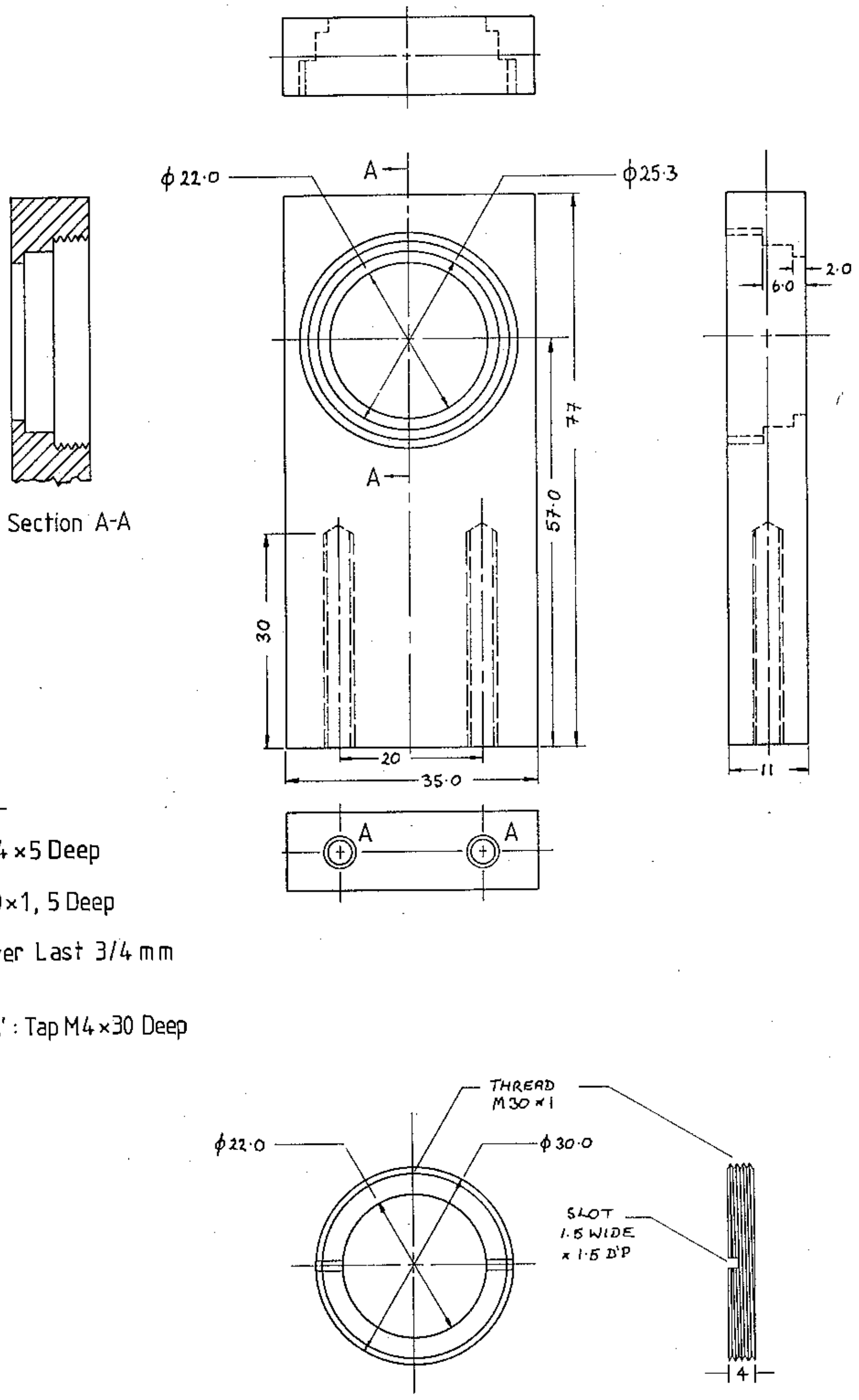

NOTES

1) Bore 28·4×5 Deep

Thread M30×1, 5 Deep

Run Out Over Last 3/4 mm

2) 2 Holes 'A' : Tap M4×30 Deep

Figure 4.4 LAO 167 Lens Holder

than two of the mirrors and the 175 mm lens, were then fixed to broad thick optical support rails which were screwed down at intervals of around 100 mm onto the table tops via thick bars. The two tables on which all the optics, the cameras, and the film transport were mounted were old film scanning table tops. These consisted of cast honeycomb frames supporting a top made of melamine filled with an inert material. This structure was strong and had good vibration damping properties.

Two LINK 109 A video cameras were secured by two locating pegs in their bases to aluminium plates of 10 mm thickness, whose dimensions matched the base of the cameras.

To minimise the effects of stray light, and to cut down the deposition of dust on the optical surfaces, various light shields and covers were incorporated into the design. An aperture located in front of the 175 mm lens cut out unwanted reflections from the film holder, and limited the angular view to that required for imaging. The cubic beam-splitter had a light absorbing shield around the unused face to eliminate spurious reflections. Both of the cameras were fitted with tubes screwed into their lens mounts to prevent stray light from falling onto the camera tubes. These light shields were made from Tufnol and painted with matt black lacquer. Over all the optical system, following the Y stage but excluding the cameras, was placed a metal dust and light cover. The inner surface was roughened and painted matt black.

4.4.3.4 Stage and Laser Mounting

The Z stage was directly fixed to the table top, and the X stage was fixed to the moving top surface of the Z stage. The Y stage was mounted vertically, supported by a specially designed mount. This mount was kinematically located on the table top under its own weight and adjusting screws allowed the precise rotation of the stage about the Z axis and the X axis. The 175 mm lens and one mirror was mounted on the moving surface of this stage, the second mirror was fixed to the stage mount. The laser and its associated optical system were mounted on an independent rail in front of the X-Z stage assembly. On the rail were mounted the microscope objective, pinhole, and the beam expander doublet. The whole assembly was completely enclosed by a metal cover. A plan view of CHIMAERA and an isometric view of the optical system are shown in figure 4.5.

4.5 Video Cameras and Monitors

Two LINK 109A cameras were chosen because they offered a high quality camera with several valuable features at a reasonable price. They could take any 1" tube: Vidicon, Newvicon, Ultricon, Plumbicon, etc., and allowed the use of fixed or variable target voltage. The highly stable video amplifier had a DC - 10 MHz (-3dB point) bandwidth, and the distortion and linearity were better than 1% in the inner scan region. The cameras used a 625 line 2:1 interlaced raster scan. The HOLMES project at CERN had shown that the defeat of the target Automatic Gain Control (AGC) was desirable for successful scanning.

4.5.1 Image Tubes

The quality of the final picture of the replayed hologram depended very strongly on the choice of image tube. Experience at CERN had also shown that running the laser at its full power considerably shortened the plasma tube life, thus the sensitivity of the camera tube was an important parameter.

Initially CHIMAERA was designed to use standard 1" Vidicon tubes in both the high and low magnification

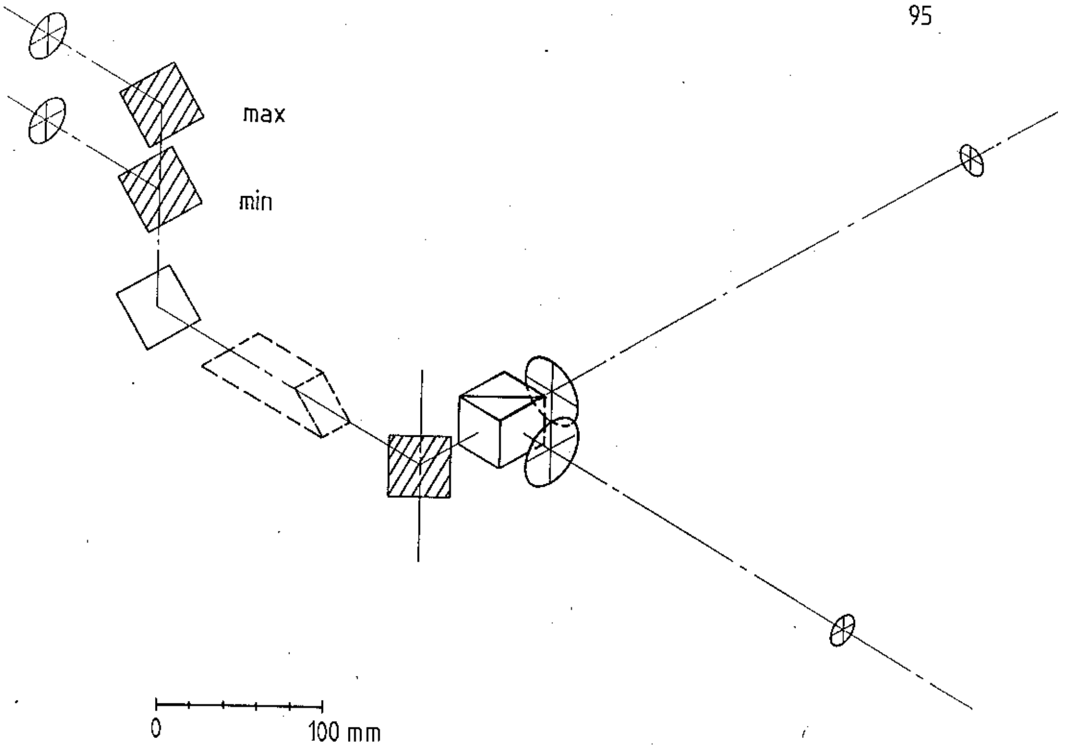

Optical System - Isometric View

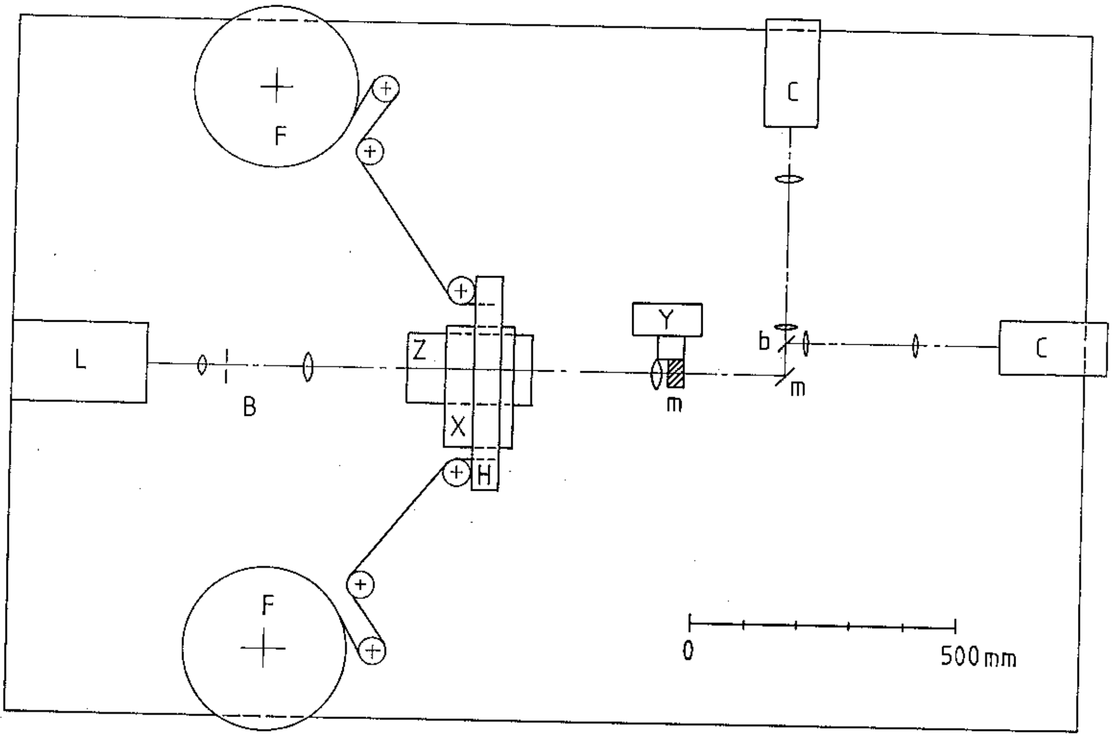

B	Beam Expander	H	Film Holder	b	Cubic Beam Splitter
C	Video Camera	L	ArgonIon Laser	m	Mirror
F	Film Transport	X,Y,Z	X,Y,Z - Stage		

Figure 4.5 Plan View of CHIMAERA, Isometric View of the Optical System

cameras. Tests had shown that the Industrial Grade EMI 9677C Vidicon performed well in the low-magnification camera. A satisfactory picture in the high magnification camera, with around 1/50 of the illumination, was only obtained at a direct laser power of 5-6 mW. This allowed operation of CHIMAERA at a total power of around 10-12 mW. In practice it was difficult to obtain a really good picture even at these power levels, as the dark current was high and non-uniform. This was in part due to the high target voltage being used; the dark current rises as the n'th power of the target voltage, where n is between 3 and 6. A high sensitivity long-lag Vidicon, the EEV P8034A was then tried in the high magnification camera. This tube was designed for slow scan operation. The image with this tube was markedly better, and with operator control of the target voltage, AGC defeated, acceptable scanning was performed at a total laser power of 5 mW. The major disadvantage of the P8034A was the long lag time, nearly 20% of the signal was still present 0.2 s after the illumination was removed. This was a considerable disadvantage when focussing,as the image appeared to change very slowly. The particular sample that I used, a tube that had already had several hundred hours use, possessed a highly non-uniform dark current, giving an uneven background in the absence of illumination. More sensitve tubes with lower dark currents were then considered. The Chalnicon, Newvicon, and Silicon-Target Vidicon all had a high sensitivity combined with low dark current. They are, however, all devices with a fixed sensitivity and operate at a preset target voltage, no target AGC being possible. Tests were carried out on CHIMAERA using a real hologram under realistic scanning conditions. Two tubes were tested, a 2/3" Phillips XQ1247 Newvicon in a Phillips LDH26 camera, and a 1" RCA 4532/U Ultricon in a LINK 109A camera. In both cases the picture quality was high, with very good contrast and a uniform background. The 1" Ultricon had a slightly higher resolution as expected. The RCA Ultricon (a form of Silicon Target Vidicon) was chosen for use in the high magnification camera in CHIMAERA. Table 4.3 presents the important features of the three 1" tubes tested in CHIMAERA.

TABLE 4.3

IMPORTANT FEATURES OF THE IMAGE TUBES TESTED

	Vidicon 9677C	Vidicon P8034A	Ultricon 4532/U
Manufacturer	EMI	EEV	RCA
Spectral Sensitivity			
Sensitivity (A/W)	0.36	0.4 *	0.45
at Peak λ (nm)	490	620	700
Sensitivity at			
λ = 514 nm (A/W)	0.32	0.2	0.35
λ = 633 nm (A/W)	0.14	0.38	0.42
Resolution			
Response at 400 TV Lines (%)	60	20	50
Resolution at 20% Response (TV lines)	650	400	550
Signal Current at ** 1 lux, with 10 nA Dark Current (nA)	50	120	700
Lag current after 100 ms with 100 nA signal (%)	6	30	7

* Personal Communication from EEV

** Tungsten lamp at a colour temperature of 2856 K

Sources: EMI Data Sheet DS.780, EEV Data Sheet Dec 1972,
RCA Data Sheet Feb 1983

The picture quality obtained with the RCA Ultricon was the best seen with any of the camera tubes at any laser power. Running the laser at 5 mW resulted in good pictures, and the large dynamic range helped to avoid any problems with the fixed sensitivity. The most important parameter in table 4.3 is the Signal Current for 10 nA dark current, it is in this parameter that the 4532/U excells. The Ultricon has a very high immunity to damage by high light intensities. This property is valuable in CHIMAERA where a dense film is punctuated by clear regions containing the frame numbers. The low and uniform dark current of this tube contribute to the high contrast of the picture over the entire scanning area.

One problem that it has not been possible to eliminate is the formation in coherent illumination of interference fringes on or near the photoconductive layer of the low magnification camera Vidicon. The photoconductive layer of a Vidicon is made of SbS_3, and Vidicon targets have a high reflectance in the visible region of between 10 and 30 %. The structure of the glass faceplate, transparent signal electrode, and SbS_3 layer can generate interference fringes in coherent light. As these are situated close to the target they have a high contrast, and cannot be eliminated. No interference effects were seen with the Ultricon tube.

The frame number camera was a Hitachi HV62 camera fitted with the 2/3" 20PE19 Vidicon. This camera used a 625 line random interlace scan, with a limiting horizontal resolution of 500 TV lines.

4.5.2 Anamorphism and AGC

Experience from the HOLMES I project suggested that some degree of anamorphic magnification was desirable. The primary interactions produced a narrow forward-going cone of particles. Separation of the individual outgoing tracks was made easier by increasing the magnification transverse to the beam axis (X - axis).

Anamorphic magnification can be obtained in two ways: optically using a cylindrical lens or prism train, or electronically by altering the size of the scanned area on the camera tube. The second method has the advantage of ease of adjustment of the magnification ratio and cost, as precision cylindrical lenses are expensive to make. The disadvantages of changing the scanning ratio are a loss of resolution and sensitivity, and the likelihood of permanently changing the photoconductive layer on the image tube In HOLMES a specially modified Hamamatsu C1000-16 camera was provided with variable anamorphic ratios of 1:1, 2:1, 4:1, and 8:1 (Y:X). The 4:1 ratio was found to be the most useful. With unmodified LINK 109A cameras it was possible to achieve a 1.5:1 anamorphism without modification, and this ratio was used in the low magnification camera in CHIMAERA. No anamorphism was used on the high magnification camera as I felt that it hindered the focussing without adding to the clarity.

Early experiments at CERN had shown the benefits of spatial filtering on the image, the resulting picture being essentially white dots on a black background. Using cameras with a normal AGC time constant resulted in the gain being increased too much and resolution suffering. I modified the AGC time constant on the low magnification camera, reducing it until it reacted to small areas of peak white. This has proved entirely satisfactory.

4.5.3 The Video Monitors

To fully utiilise the resolution obtainable from the camera, high quality monochrome monitors were needed. A bandwidth of greater than 10 MHz (-3dB point) was required, and small geometric distortions were advantageous. Two monitors were purchased, the Electrohome EVM-1220 (12") and the Electrohome EVM-1519 (15"). A brief specification of these monitors is given in table 4.4.

TABLE 4.4
BRIEF SPECIFICATIONS OF THE VIDEO MONITORS

General to both Monitors	Bandwidth 100 Hz - 18 MHz ± 3 dB Geometric Distortions $\leq$ 2% of height Linearity $\leq$ 2% of height Rise and Fall time $\leq$ 20 ns Phosphor P4

	EVM-1220	EVM-1519
Resolution		
Centre (TV lines)	800	1000
Corner (TV lines)	650	800

The 15" monitor was used to display the low magnification camera image, and, when selected by a switch on the monitor, the frame number camera image. The 12" monitor was used to display the high magnification image.

CHAPTER 5 THE CHIM SOFTWARE

The software for the CHIMAERA machine was split into two distinct areas. The control software, running mainly in the microprocessor, and the data-acquisition software residing in the PDP 11/44. The 11/44 software included a CAMAC driver, and routines written in MACRO-11 and FORTRAN 4, that allowed the FORTRAN guidance program to communicate with the CAMAC crate and via this the 8085 microprocessor.

The microprocessor program was written in 8085 machine code, and was stored in Programmable Read-Only Memory. The code occupied about 1300 bytes. The 11/44 code ran under the RSX-11M operating system, and was extensively overlaid in order to fit it into a 24 k-word partition. This allowed the use of an 8 k-word resident FORTRAN library. The FORTRAN code in the PDP 11/44 was known as "CHIM".

5.1 The Scanning Guidance Program

The scanning guidance formed a large part of CHIM, and was entirely new. Five "Processor" program modules were designed for the separate functions of reading and transforming the predictions, defining and measuring the fiducial marks, measuring an event, writing the data to the output file, and performing the check scan. Each Processor was independent of the others, although they shared some of the low level stage control subroutines.

The decision to use the HYDRA dynamic storage system was motivated by two considerations. Firstly it was the ideal data storage system for the events on the film, mirroring their tree structure, and secondly it allowed the use of a large number of the routines from the "COPPA" system written in the Bubble Chamber group at UCL.

The COPPA software was written as the control and guidance system for the conventional film scanning machines. It was designed to run on a PDP 11/44 computer with the RSX-11M operating system, and to use terminals from the Cifer 2600 series. In order that the large amount of FORTRAN code could be compiled and linked into a Task occupying less than 24 k-words, the COPPA system was designed as an overlaid task. Both the FORTRAN guidance and many of the operating system routines were overlaid.

5.1.1 The HYDRA Dynamic Data System

The HYDRA dynamic storage system uses "data banks" whose size is defined in the program when they are created (raised), and which are linked to each other in a way determined at the time of raising, but which could be changed later. The banks can be removed (dropped) from the tree structure as desired. This is done by setting the appropriate bit in the status word of the bank. When a large number of banks have been marked in this way and the remaining space is limited, the HYDRA system automatically instigates a "garbage-collection" and removes these banks. This garbage-collection may also be directly called from a subroutine if desired. The structre of a HYDRA bank is shown in Fig.5.1.

HYDRA banks are connected to each other by "links". There are two types, "structural" and "reference". A structural link points from the root of a tree structure towards the top; these links are mandatory. A reference link can point to any bank in the tree structure, in particular it can point towards the root of the tree. Using the reference links a tree (or part of a tree) can only be traversed from the root upwards . The links in link position -1 have a special meaning, they point to banks which are at the same level in the tree.

The HYDRA system used a large piece of blank Common to

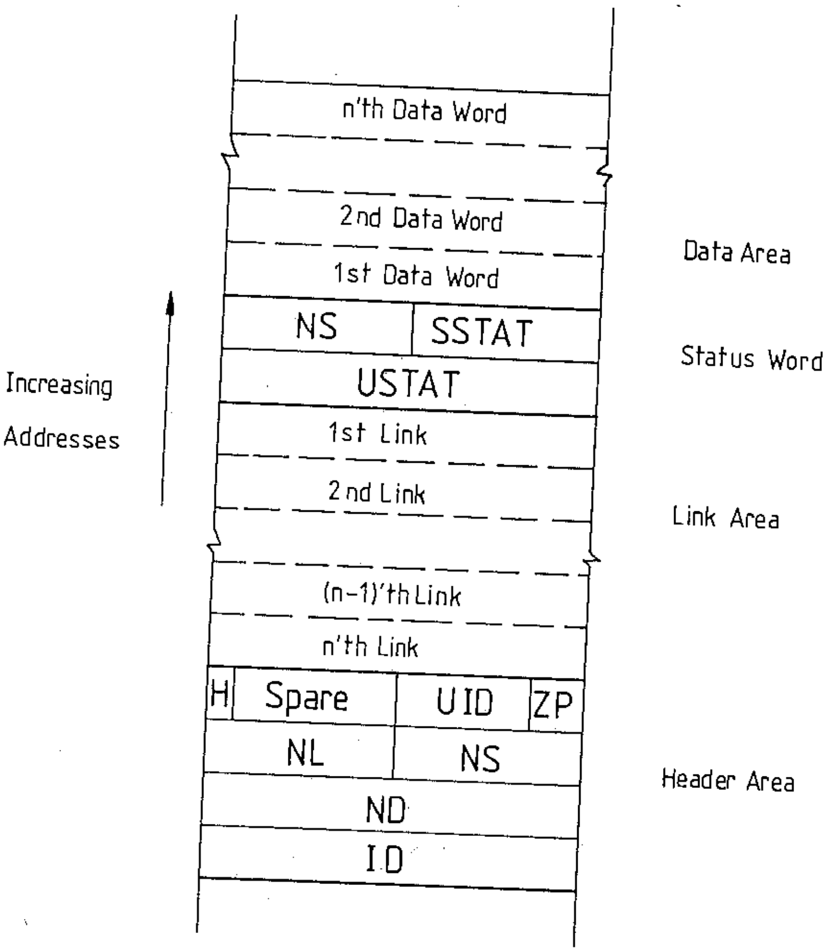

H = Header Flag

ID = Bank ID (2 ASCII)

ND = Number of Real Data Words

NL = Number of Links

NS = Number of Structural Links

SSTAT = System Status Bits

USTAT = User Status Bits

UID = User Identification

ZP = Zip Priority

Figure 5.1 Structure of a HYDRA Bank

store the links and data from each bank, the actual location in Common usually did not concern the programmer. Thus there were a number of Common blocks required by HYDRA. Folowing the practice of the COPPA system certain other Common blocks were introduced. All the file names, the CAMAC interface parameters, and various aspects of the I/O were contained in Common. All other dynamic variables were passed in the subroutine arguments, or, in the case of the "Event" Processor, a small HYDRA bank (DS) was used to store data required by many subroutines.

The HYDRA data structure in CHIM is shown in Fig. 5.2 The banks lying below the "Frame" (FR) bank mirrored the structure, and contained the coordinate data, of the measured event. These banks were only raised as the particular event being measured required. All the other banks existed for all the measurements. The "Title" banks were special banks containing formatted data which was read from the title files using the HYDRA TQ routines. There were two title banks in CHIM, one containg data from the first line of the prediction file and the other containing the estimated positions of the fiducials. Title banks allow data contained in external files to be directly read into the system. A brief description of each bank is given in table 5.1.

5.1.2 The CHIM Structure

The "Structure Charts" for CHIM are shown in Fig. 5.3 and 5.4. A Structure Chart shows (Yourdon 1979) the structural connections between subroutines and indicates their hierarchy, it does not in general indicate the logical ordering of the subroutines. Each box represents a subroutine and the lines show the links between routines. The level of a box indicates its hierarchical position. Lower level routines are dependent on the higher ones. The major loops in the program are indicated. A subroutine chosen by a decision taken in the routine above it has its

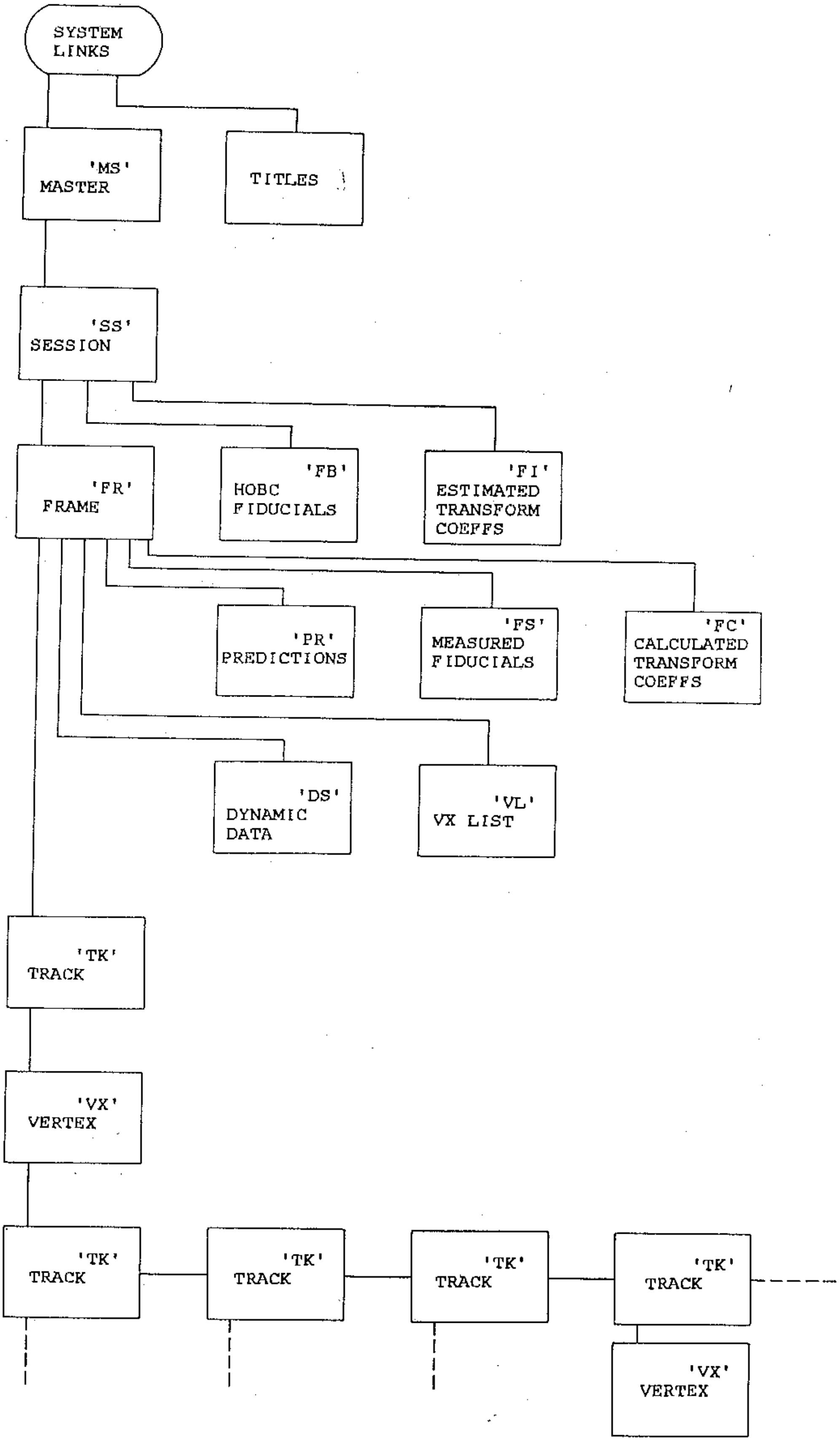

Figure 5.2 HYDRA Structure in CHIM

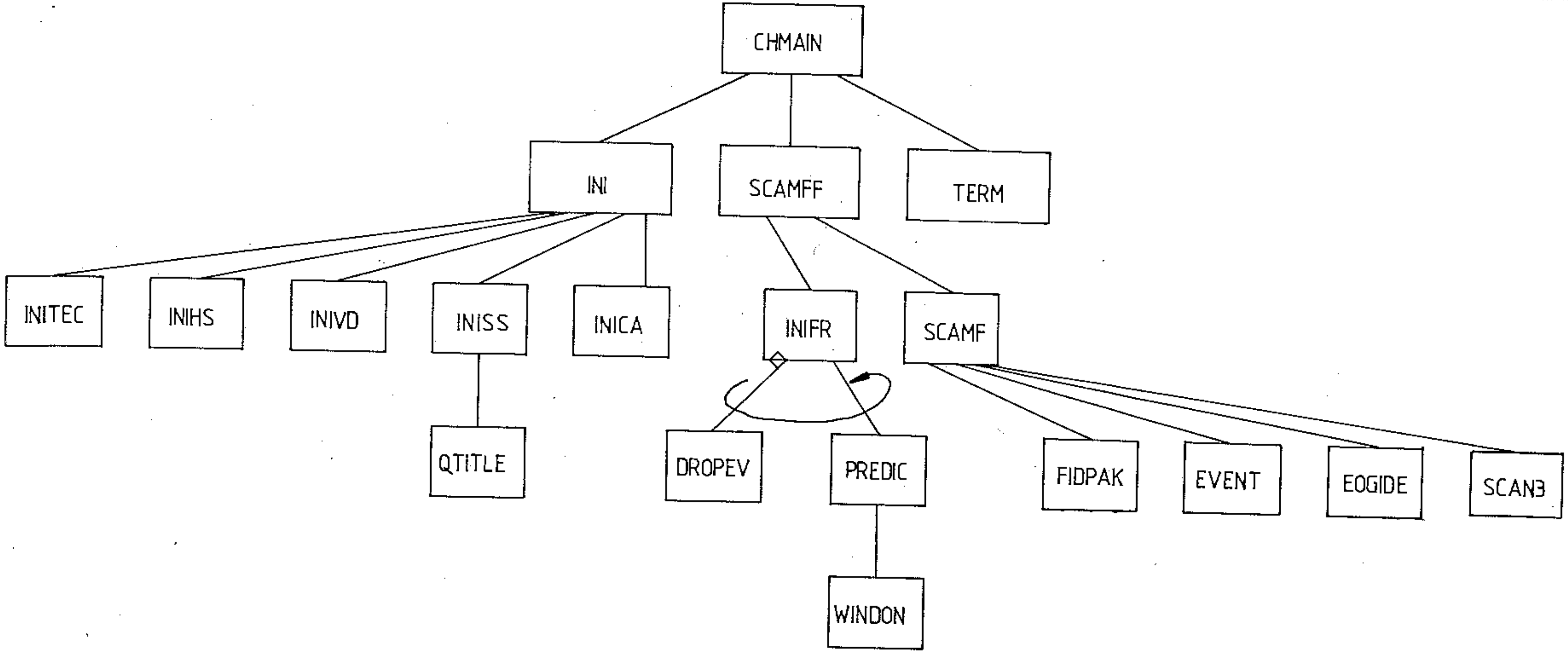

Figure 5.3 Structure Chart for CHIM

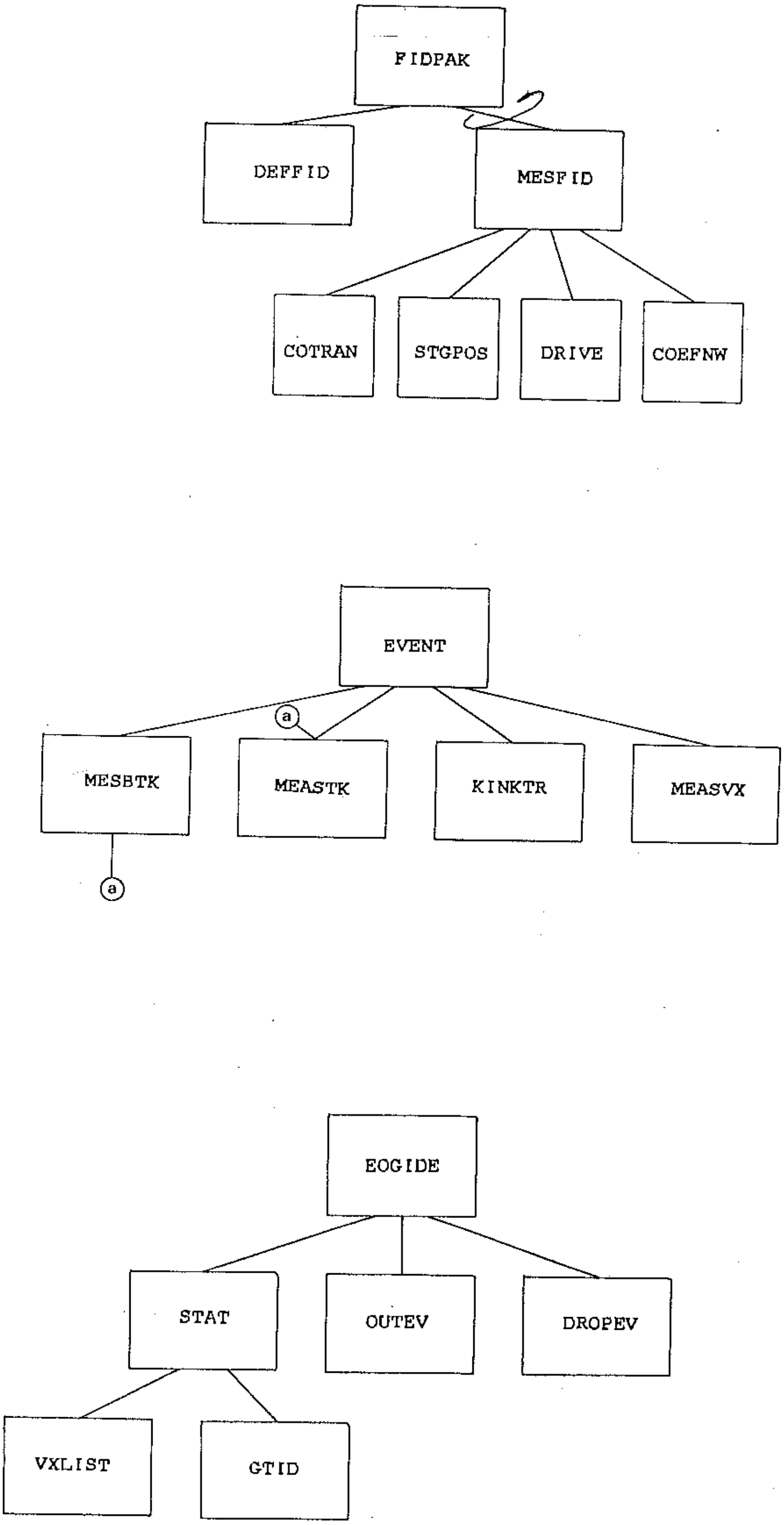

Figure 5.4 Structure Chart for CHIM Processors

link originate in a diamond. The three major Processors, originating in the subroutines FIDPAK, EVENT, and EOGIDE are expanded in greater detail in Fig.5.4. Small subroutines common to many program modules are not shown, these are mainly associated with I/O of data to the VDU, stage driving routines, and file handling.

TABLE 5.1
DESCRIPTION OF THE HYDRA BANKS

BANK	SIZE (Words)	DESCRIPTION
DS	6	Variables used in the event steering routines
FB	64	Coordinate triples of the fiducials in the HOBC system
FC	10	Fiducial coordinate transformation coefficients
FI	10	Initial estimates for the fiducial transformation coefficients
FR	8	General data (time, operator ID etc.) for each frame
FS	64	Measured coordinate triples for each fiducial
MS	4	Master session bank (no data)
PR	14	Predictions and transformed predictions of the beam track
SS	5	Session bank containing roll number, operator ID, winding direction
TK	>4	Measured coordinate points and alphanumeric code for a track
VL	40	List of vertex codes and link addresses for each vertex.
VX	6	Measured position and alphanumeric code for a vertex

TABLE 5.2
THE MAIN SUBROUTINES IN CHIM

Routine	Description
CHMAIN	The top level guidance
INI	Initialising routine guidance
INITEC	Sets up Error Code processing
INIHS	Initialises the HYDRA system
INIVD	Initialises the VDU handling
INISS	Initialises the session information
INICA	Initialises CAMAC, tests stages
SCAMFF	Main scan and measure guidance
INIFR	Gets information required for each frame
DROPEV	Drops a previous HYDRA data structure
PREDIC	Finds prediction information for the desired frame
WINDON	Moves the stages to the correct positions to allow film winding
SCAMF	Scan-and-measure-a-single-frame guidance
FIDPAK	Fiducials measurement guidance
EVENT	Event guidance routine
EOGIDE	Event output guidance
SCAN3	Edit-scan guidance
DEFFID	Defines set of fiducials to be measured
MESFID	Drive to fiducial poisition, prompt operator to measure it
COTRAN	Transform the approximate fiducial position
COEFNW	Update the transformation coefficients
MESBTK	Drive to prediction get beam track code
MEASTK	Measure tracks points,
MEASVX	Measure a vertex, get vertex code
KINKTR	On-line track kink guidance
STAT	Produces statistical data from FR bank
VXLIST	Performs a search of the event tree to produce list of vertices
GTID	Gets the next ID from a direct access file
OUTEV	Write out event tree to data file
DRIVE	Allows operator to control stages from keypad
KEYPAD	Interface routine for the operator's keypad
STGPOS	Drives one stage to a given coordinate
STGRD	Reads one stage position
STGMOV	Moves one stage in a given direction at a set speed
STGSTP	Stops one stage

Following the COPPA system certain functions in FORTRAN were accessed via subroutines that provided a buffer between the process and the specific FORTRAN code. The FORTRAN OPEN and CLOSE subroutines were both placed in separate routines that allowed file handling by mnemonic. I/O to the VDU was by ENCODE/DECODE statements and by specially written subroutines. These routines contained the code necessary to drive a specific output device. Although the output routine only allowed a maximum of 40 characters per line to be written to the VDU screen, it did enable positioning of the cursor anywhere on the screen and various highlighting options to be selected. These features allowed me to present the CHIMAERA operators with information on a fully formatted screen.

5.1.3 Input and Output via CAMAC

There were two communication paths between the CHIM task and the CHIMAERA table and operator. One was via the terminal driver and terminal interface routines, the other was via the CAMAC driver and crate. It would have been possible to communicate directly with CAMAC but it was convenient to use an interface routine.

5.1.3.1 The CAMAC Driver

The CAMAC crate was directly connected to the PDP 11/44 backplane via a UNIBUS cable. Although the crate could have been directly accessed, it was driven by a driver to avoid conflicts with other tasks running in the computer.

The driver used was supplied by GEC ,and was a version of the CERN CAMAC driver (Botteril, Lengaur, Silverman), modified by P.Clout in 1978. The driver provided individual programmed transfers, list operations, and block data transfers. CAMAC LAM interrupts could be booked and waited for using standard event flags. The driver was protected against more than one user accessing the same CAMAC module, unless this was allowed by the module's owner. Only privileged tasks could access system modules.

In CHIM only the direct programmed transfer, QIO, was used, as testing of a module's Q and X response was always required. Both 16 and 24-bit word transfers were used, each taking 2.8 ms to instigate and then process the response.

5.1.3.2 The CAMAC Interface

The interface subroutine was written in MACRO-11 assembly language by R.Cranfield at UCL, and performed the basic read and write operations on the modules in the crate. In CHIMAERA the only CAMAC module used was the 9017/2 24-bit I/O driver (Nuclear Enterprises). This unit contained a 24-bit output register whose contents could be changed, and 24-bit input register whose contents could be read. Writing data to the output lines generated an output strobe of 1 microsecond duration. A separate "look-at-me" (LAM) input was also provided. Routines within the interface handled the input and output of data and allowed asynchronous trapping of LAM's to take place. These routines were called directly from the FORTRAN subroutines controlling the movement of the stages.

Interrupts from the crate were handled by a routine MHWAIT which was called whenever an interrupt was expected. The main task would then idle until either an interrupt was received, or would (optionally) time-out after a preset time had elapsed. This routine returned the type of interrupt and associated parameters as arguments.

Asynchronous interrupts from the VDU were handled by AST traps, the interrupt handling being initialized by a call to the routine MHINKB which passed the FORTRAN logical unit number to the MACRO-11 directive.

The CAMAC crate contained more than one module and within CHIM each was identified by an integer between 1 and 5. The absolute position of each module was assigned by the routine MHCASS.

5.1.3.3 FORTRAN to CAMAC Routines

Control of the stages and interfacing of the special operator's keypad were performed by three FORTRAN subroutines: STAGE, DRIVE, KEYPAD.

The routine STAGE consisted of four independent routines for moving the stages; STGPOS, STGRD, STGMOV, STGSTP. Brief descriptions of each are given in table 5.2

The subroutine KEYPAD reset the keypad data latch by writing all zeros to the output lines of the keypad modules and using the data output strobe to reset the data latch. Immediately following this was a call to MHWAIT to process the LAM arrising from a key being depressed or released. During this waiting period any key pressed on the VDU keyboard would also have been received and this was distinguished from a keypad key by the value of a status word returned in MHWAIT. If a keypad key was depressed the data was read from the CAMAC data bus, and the key parameters passed in the arguments of KEYPAD.

The subroutine DRIVE called both KEYPAD and the routines in STAGE and enabled the operator to drive the individual stages and measure a sequence of points using the keypad. DRIVE contained three vectors of 4-byte integers, each capable of holding 100 words. This allowed the consecutive measurement of up to 100 coordinate triples. The arguments of DRIVE allowed the locking out of any stage, or could set a specified number of points to be measured. The operator could also correct measurement errors by means of two cancel keys which allowed the deletion of the last point measured or deletion of all the points measured.

5.2 The Processors

Each of the five major aspects of scanning and measuring a frame were designated as "Processors". Each Processor was designed to be used independently of the others to allow greater flexibility in the design of the overall guidance program, and to increase the versatility of the CHIM software.

The Processors in CHIM were the Prediction, Fiducial, Event, Output, and Edit Scan Processors. These are individually described in sections 5.2.1 to 5.2.5 .

5.2.1 The Prediction Processor

The flow chart of the Prediction Processor is shown in Fig.5.5 . This Processor was called if the beam-track predictions were to be used. Initially this Processor was given the first frame number in the prediction file, read in from the title bank TROL, and passed as a subroutine argument. The film winding direction, which was chosen during the initialisation of CHIM, was read from the Session (SS) bank. The operator could decide whether the prediction sought must have the correct muon category for muon-triggered frames. When the desired frame was found the operator was told to wind on the film and to enter the frame number. This served to check that the correct frame was being scanned and also to allow for missing frames or sections of film. After successfully locating the desired frame the prediction data, muon data and CEDAR (200 GeV/c film only) were stored in the PR bank.

ors by means of two cancel keys which allowed the etion of the last point measured or deletion of all the nts measured.

The Processors

Each of the five major aspects of scanning and suring a frame were designated as "Processors". Each cessor was designed to be used independently of the ers to allow greater flexibility in the design of the rall guidance program, and to increase the versatility the CHIM software.

The Processors in CHIM were the Prediction, Fiducial, nt, Output, and Edit Scan Processors. These are ividually described in sections 5.2.1 to 5.2.5 .

2.1 The Prediction Processor

The flow chart of the Prediction Processor is shown in g.5.5 . This Processor was called if the beam-track edictions were to be used. Initially this Processor was ven the first frame number in the prediction file, read from the title bank TROL, and passed as a subroutine gument. The film winding direction, which was chosen ing the initialisation of CHIM, was read from the ssion (SS) bank. The operator could decide whether the ediction sought must have the correct muon category for on-triggered frames. When the desired frame was found e operator was told to wind on the film and to enter the ame number. This served to check that the correct frame s being scanned and also to allow for missing frames or ctions of film. After successfully locating the desired ame the prediction data, muon data and CEDAR (200 GeV/c m only) were stored in the PR bank.

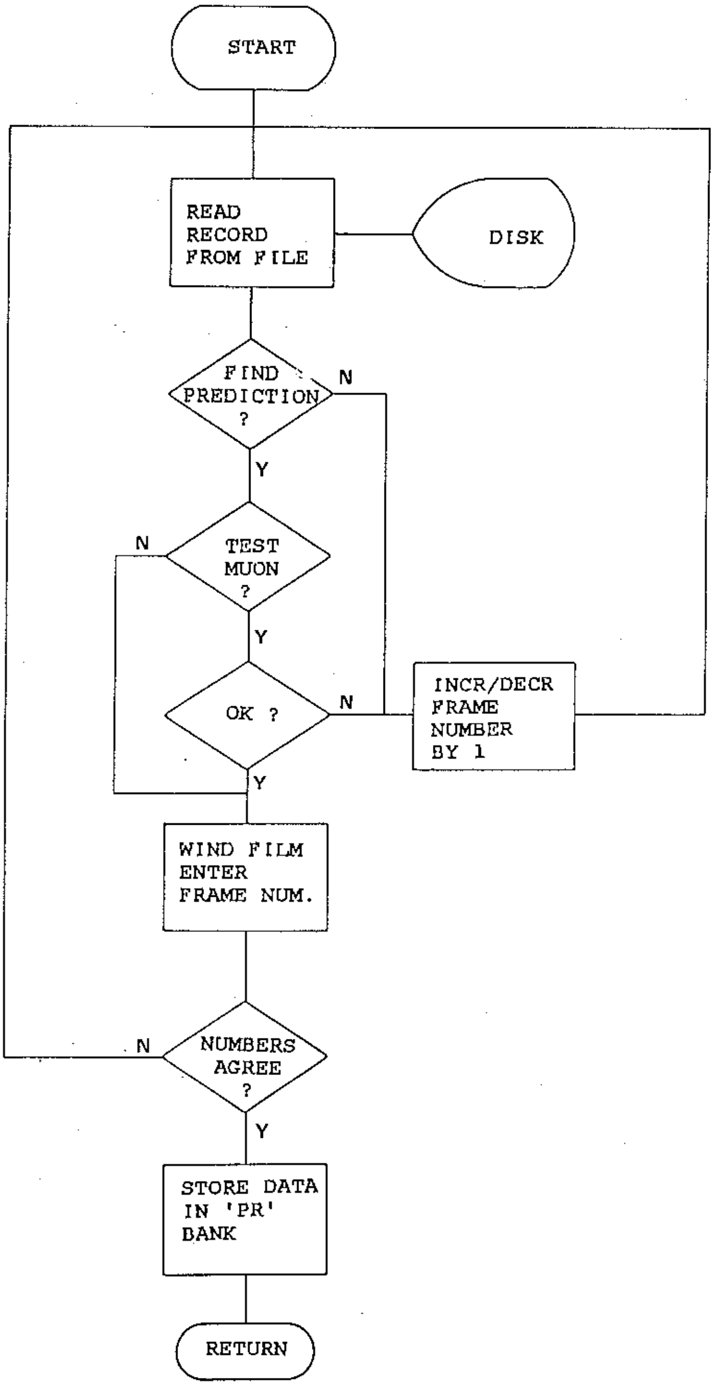

Figure 5.5 Prediction Processor Flow Chart

5.2.2 The Fiducial Processor

The flow chart of the Fiducial Processor is shown in Fig.5.6 The function of this Processor was to drive the stages to the positions of the fiducial reference crosses on the windows of HOBC. The set of fiducials to be measured could be defined by the operator, usually a default set of five was chosen. The approximate positions of the fiducials were stored in the FB bank. When a fiducial had been measured the approximate positions were corrected by adding offsets to the data in the FB bank. The measured positions of the fiducials were stored in the FS bank.

5.2.3 The Event Processor

This Processor was the main data acquisition part of CHIM, and contained an event scanning algorithm shown in Fig.5.7 . This algorithm guided the operator around the event displayed on the monitors, prompting him to acquire the structure of the event and then measure the coordinates of the tracks and vertices. The algorithm is general but the beam track has two unique features and was treated individually. Firstly there was the predicted position of the beam track to which the stages were driven, and secondly there were a variety of code letters identifying the type of frame being scanned (see appendix A). All the other tracks, originating from vertices, had only a single code letter. The principle rules of the algorithm were:

1) Every vertex was preceded by a track, this included neutral particles preceding visible vertices, whose track is not seen.

2) Each track from a vertex was followed until it left the chamber or ended in another vertex. If another vertex was found then it was measured and the tracks arising from it were followed.

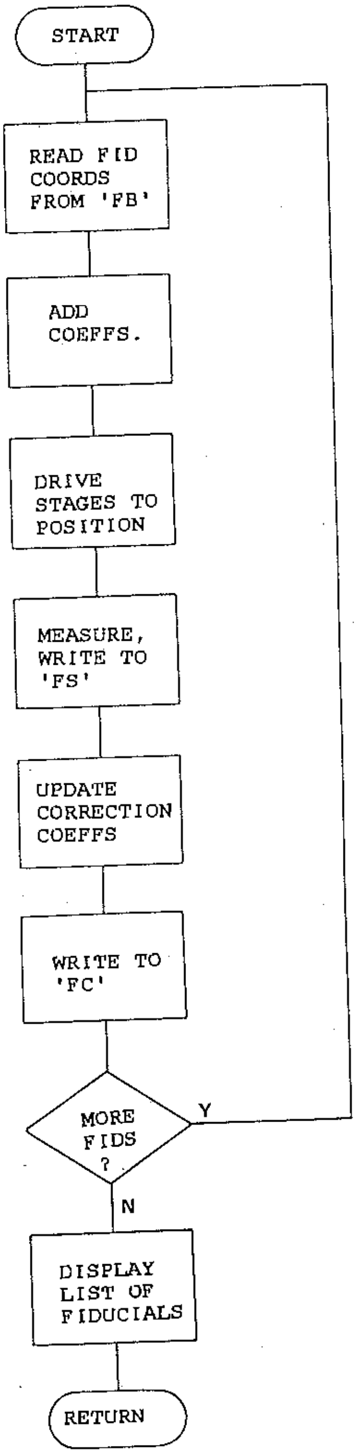

Figure 5.6 Fiducial Processor Flow Chart

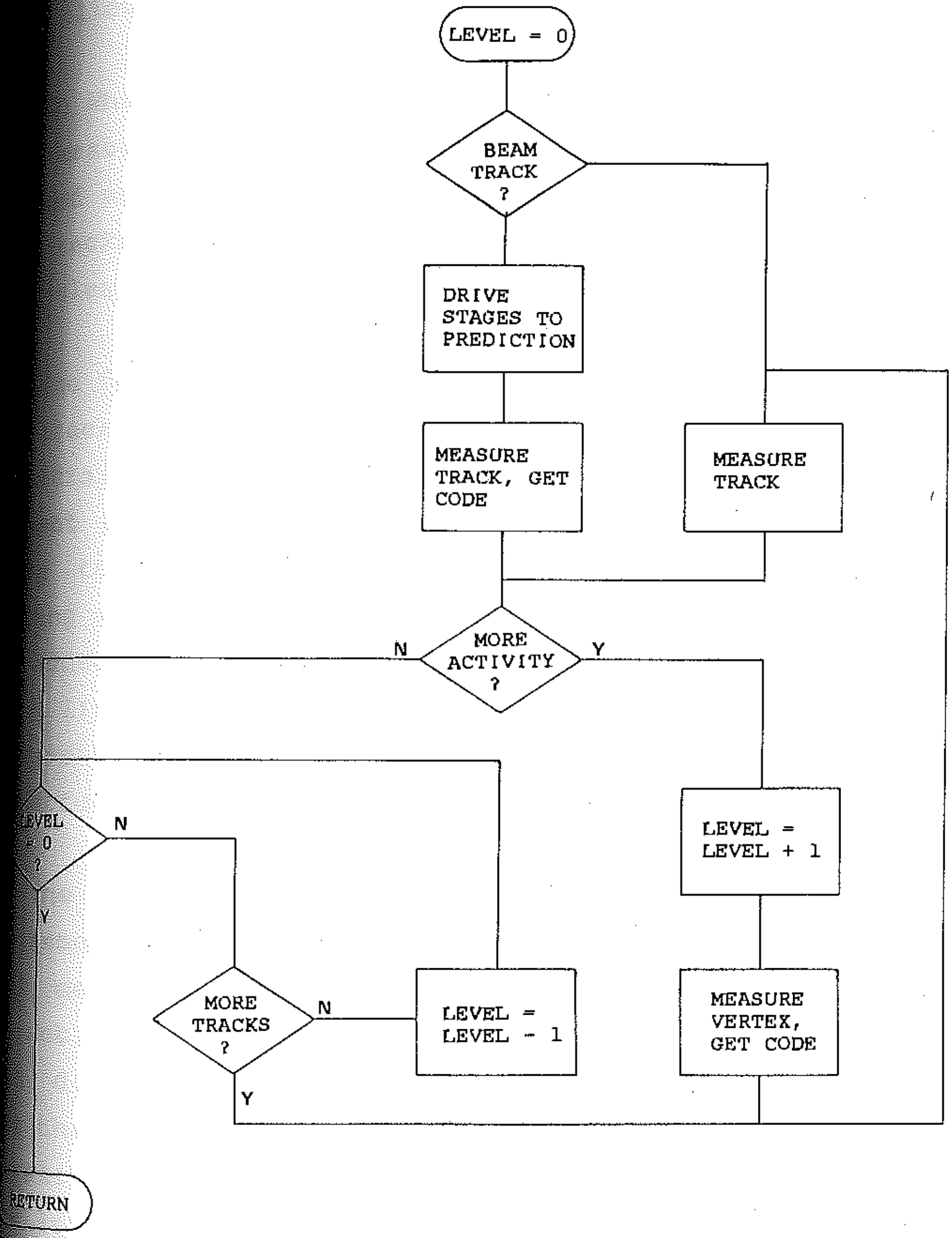

Figure 5.7 Event Scanning Algorithm Flow Chart

3) When a track was found not to decay or interact, any other tracks leaving the vertex that it originated from were followed and measured.

4) When all the tracks from a particular vertex had been measured, the tracks from the preceding vertex were followed and measured, until the operator had measured all the tracks and vertices of the event as required by the scan rules.

One feature of this scanning algorithm was the need to back track down branches of the tree structure. The HYDRA structural links that generated the tree only allowed movement in a direction away from the root. To avoid having to return to the bottom of the tree every time back tracking was required, backward pointing reference links were added to each track (TK) and vertex (VX) bank. Each of these links pointed to the vertex/track that the track/vertex originated from. Thus this part of the HYDRA data structure could be traversed in both directions.

The CERN scanning rules (appendix A) required the measurement of all the vertices in the event, but only track measurements from vertices which were clearly not interactions. Tracks that came from the primary vertex and which did not decay or interact were not recorded. In order that the tree structure and algorithm retained their generality, a track bank was raised for each "invisible" track leading to a neutral decay or interaction. Fig.5.8 shows a hypothetical, though possible, event and the resulting HYDRA bank structure that would exist after it had been scanned and measured.

5.2.4 The Output Processor

This Processor re-formatted the information in the Frame (FR) bank to provide an event header containing information on the size of the event in the blank Common.

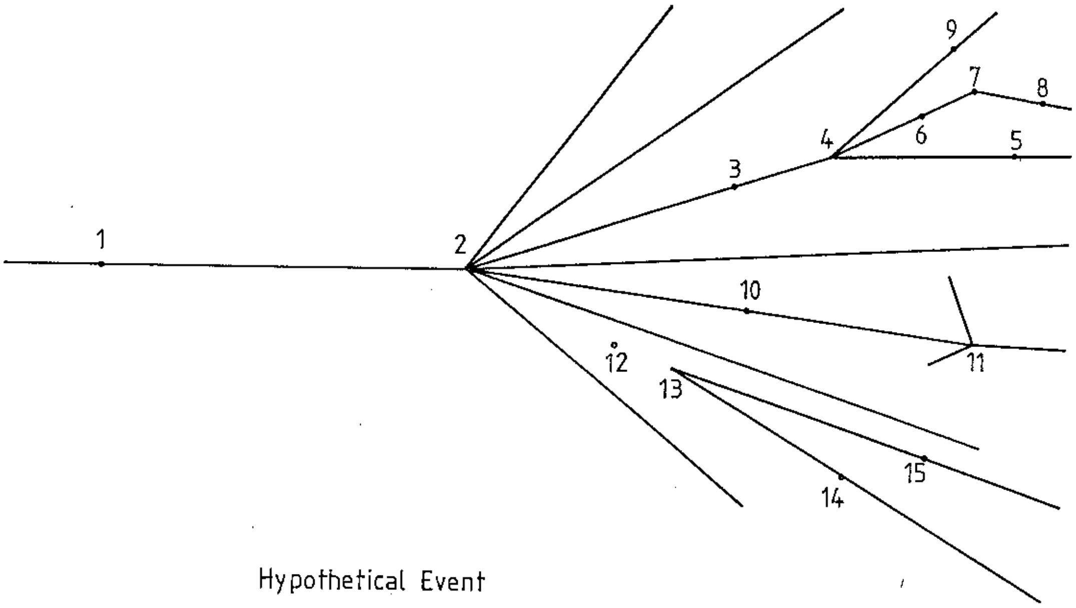

Hypothetical Event

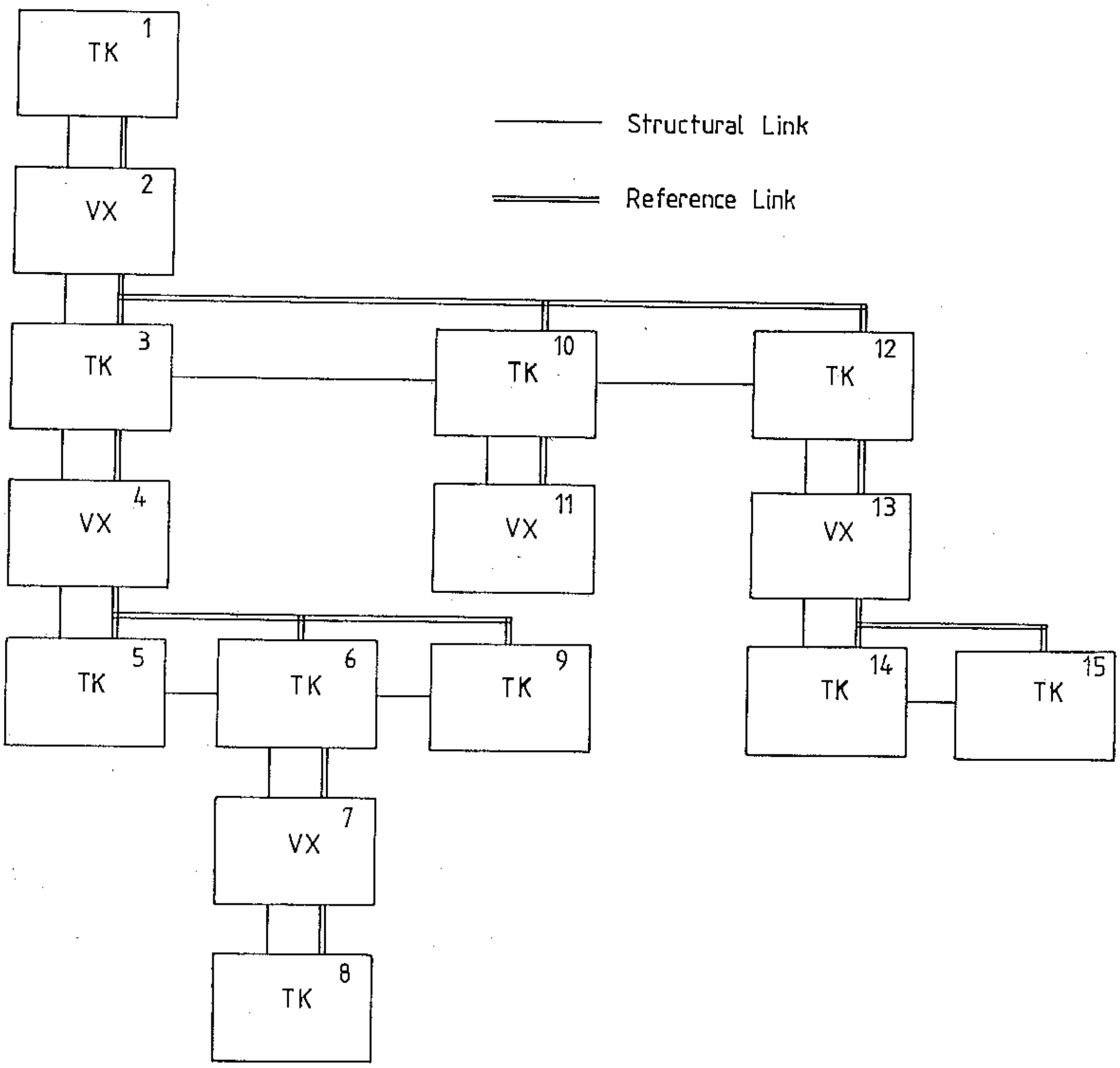

Figure 5.8 Hypothetical Event Showing the HYDRA Bank Structure

All the banks below the frame bank were then written to a disk file Following this all the banks hanging from the Frame bank were dropped. The main feature of the Output Processor was that the banks were written to disk in a form which allowed them to be read back in to the Common block. With the addition of an offset the entire tree structure could be recreated. This feature allowed the design of the Edit Scan Processor to be considerably simplified. The Output Processor also updated the statistics file and assigned a unique identifier to every event written to disk (see section 5.4.3).

5.2.5 The Edit-Scan Processor

This Processor, which is only used in the check-scan mode of operation, read a previously measured event into CHIM and rebuilt it. The operator could then either copy the event to a disk file or be led around the event to check the measurements. The Structure Chart for this Processor is shown in Fig.5.9.

The routines INSCAN and those below read in the selected event and rebuilt the tree structure from the data in Common. These routines were slightly modified versions of those used in the DUMP program (see section 5.4.2). The routine COPY and those below it allowed the operator to write the data back to disk without looking at it, or to examine the previous measurements on CHIMAERA. In the copy mode a calculated position for fiducial F32 was added (ADDF32) if this fiducial was not present in the original data. This option existed to allow data from the first scan of Roll 28 to be updated to the new data format agreed after the measurements had been made.

5.3 The Microprocessor Software

The program, written by Dr.G.Lush at UCL, consisted of two distict sections. The first part was an endlessly

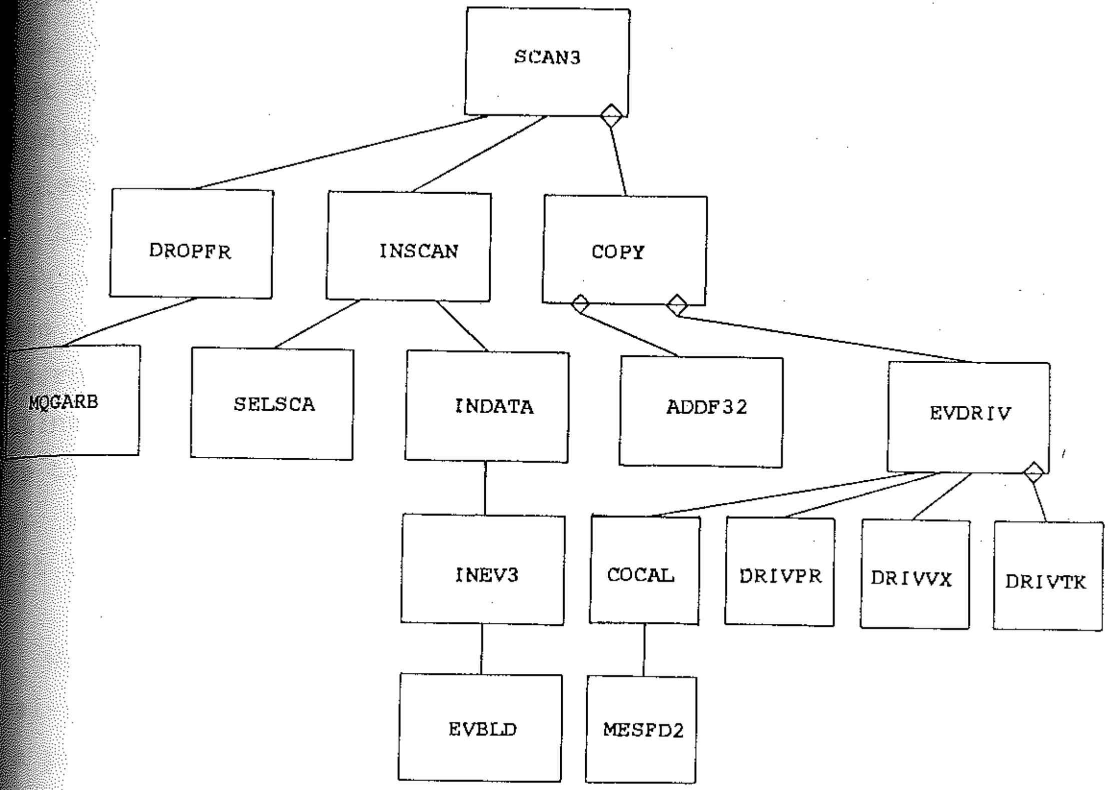

Figure 5.9 Structure Chart for the Edit-Scan Processor

executed set of instructions that followed an initialisation sequence. The routine IDLE in the loop part of the code read the position of each ANORIDE stage in turn, stored the data words and converted the 16-bit plus 4-bit BCD data format into a 16-bit number giving the stage coordinate in units of 2 microns. This number was complemented and sent to the appropriate 9017/2 I/O unit in the CAMAC crate. Following these write instructions a check on the status of each stage's Endstop flag was made. There were two ENDSTOP routines, one that sent a LAM interrupt to the relevant 9017/2 unit and an identical routine that did not send a LAM. This allowed the idle loop to continue, until the PDP 11/44 had processed the LAM, without sending a string of LAM pulses. The flow chart for this part of the code is shown in Fig.5.10 .

When an interrupt was received by the 8085, on the level-sensitive RST 6.5 pin, the program hardware vectored to a preset program location that directed control to the interrupt processing code. This part of the code (Fig.5.11) saved the registers and then read the data word from the 9017/2 I/O unit reserved for control. The program decoded this word and then accessed the 9017/2 units and ANORIDE crate as appropriate. If a coordinate move instruction had been received, a check was made on the absolute magnitude of the move, and if the required coordinate was less than 50 microns from the current stage position the move was not carried out. This jump in the code was introduced to elliminate problems encountered with moving the ANORIDE stages by very small amounts. After this operation had been completed the interrupt handling was restored and execution of the coordinate updating loop was continued.

5.4 Subsidiary Data Processing

Three independent programs were used to provide CHIM with a prediction file, produce a standard CERN formatted

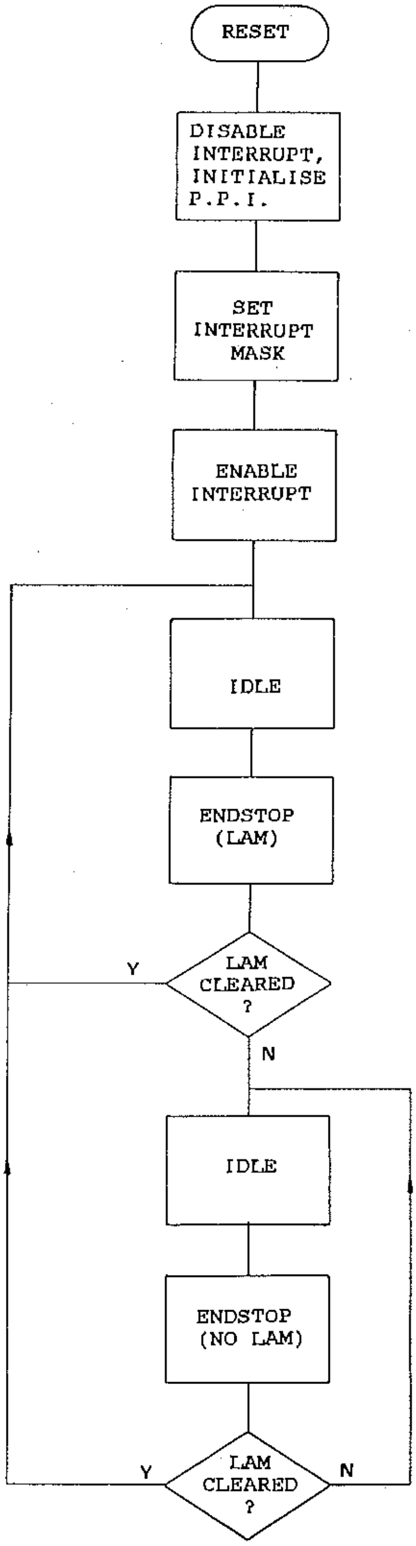

Figure 5.10 Microprocessor Flow Chart - Idle and Endstop Code

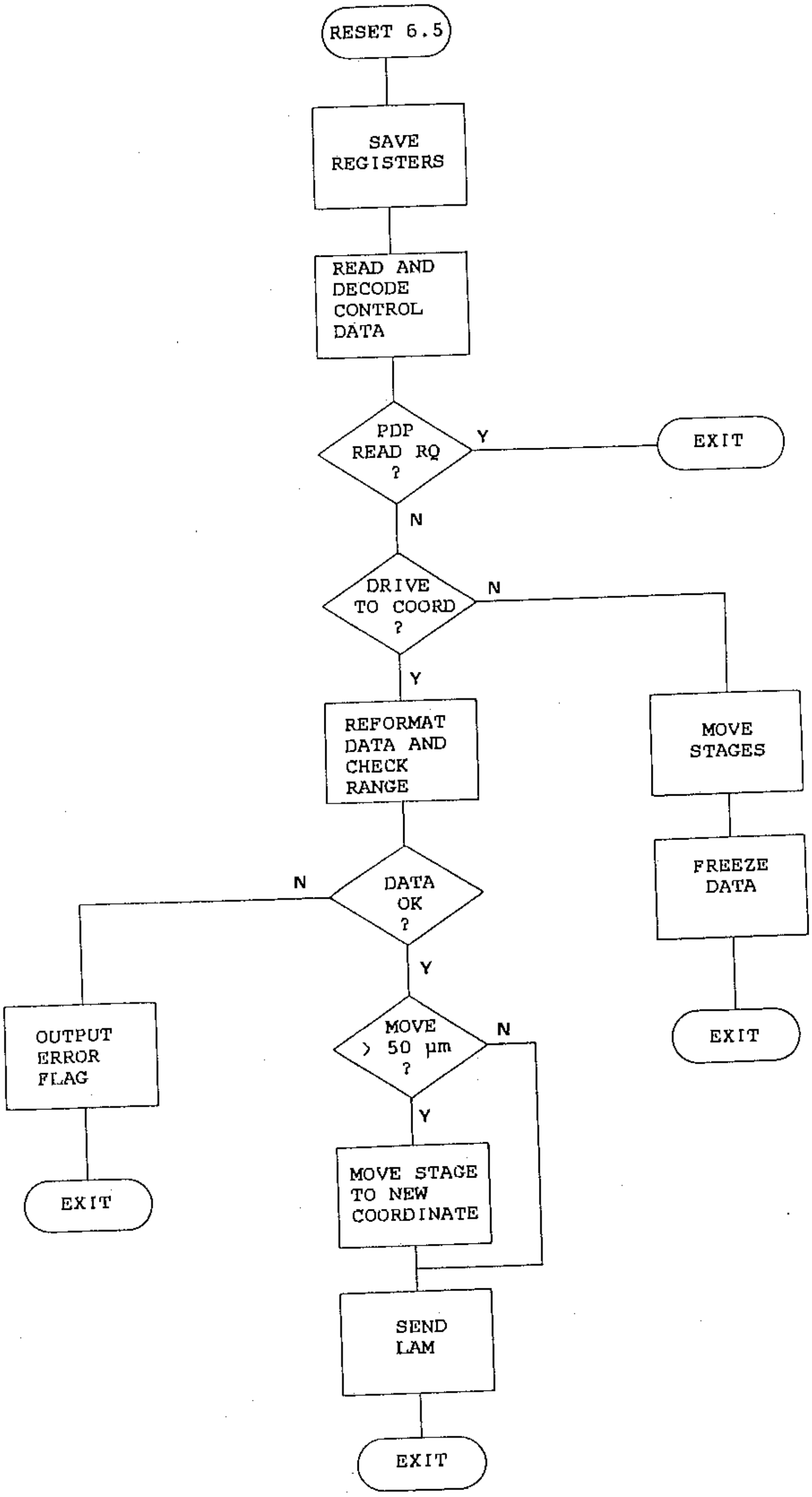

Figure 5.11 Microprocessor Flow Chart - Interrupt Processor Code

data file, and to allow a structured search of the statistics file. The second and third programs were written by P. Campbell-Burns at UCL.

5.4.1 The Prediction File Preprocessor

The prediction tape, produced at CERN, consisted of a header containing the number of the roll, the date, the first frame number, other information pertaining to the entire file, and a list of fiducials with their coordinates in the HOBC frame of reference. The remainder of the file contained the prediction, muon, and CEDAR information for each frame. It was neccessary to process this file before it was read by CHIM for two reasons. Firstly, for reasons of general compatibility, the prediction tape was written in 80 column card format. This file was sparsely filled and occupied about ten times as much space as the data contained in it required. Secondly it was neccessary to reject all the frames which did not have exactly one pair of predicted incident beam particle coordinates and it was easier to do this in the preprocessor than in CHIM. The files produced by the preprocessor were two HYDRA title files and a compact binary direct access file containing the prediction data.

5.4.2 The Output File Processor

This program converted the raw data from CHIM into the standard NA25 data format. The program (DUMP) rebuilt each event into its original HYDRA tree structure, and then selected the data required for the CERN file. After each event had been processed the event was dropped and the next event read in. DUMP selected track banks only if they arose from vertices with decay topologies; it rejected any data in the "null" track banks whose role was entirely structural.

5.4.3 The Statistics Enquiry Program

The requirement that every event carried a unique identifier led to the creation of a statistics file having the dual role of storing information on each event and holding the identity number of the last frame measured.

In CHIM a list of all the vertex topologies was made and held in the Vertex List bank (VL). This, along with other data (measurement time, operator ID, date etc.), was written to a separate sequential statistics file. An enquiry program, ENQUIR, enabled this file to be searched using logical and relational operators. Thus, for example, a search could be made for all vertices with the V2 topology measured by operator 41 in frames 100 to 450 inclusive. This facility proved to be very useful, especially in providing lists for the check scan. ENQUIR was an interactive program, the output being written to the VDU running the task or to a hard copy device.

CHAPTER 6 DATA ANALYSIS

6.1 Scanning and Measuring the Holograms

Every film distributed to members of the collaboration was scanned under a unifrom set of scan rules (Appendix A). However, as each table was a unique device, there will be differences in the data from each laboratory. The major part of the 360 GeV data was scanned at Brussels and CERN, and the differences between these data sets is discussed in section 6.5. The rest of the 360 GeV data was scanned in Bari, Mons, UCL, and Vienna. The status of the film at September 1984 is summarised in table 6.1. Only film in the SCAN 3 or SCAN 4 categories is used in this analysis.

TABLE 6.1
STATUS OF THE 360 GEV FILM

Roll Number	Frame Number	Laboratory	Status
9/10	ALL	CERN	SCAN 4
23	1104-2093	CERN	SCAN 4
24	31-1911	BRUS	SCAN 4
25	1-2000	BARI	SCAN 2
27	1-1200	VIEN	SCAN 3
28	1- 900	UCL	SCAN 3
29	1- 650	MONS	SCAN 3
29	651-2000	BRUS	SCAN 3
30	1000-2104	CERN	SCAN 4
31	50-1986	BRUS	SCAN 3
32	1-1592	CERN	SCAN 4
33	1-2066	BRUS	SCAN 3

The data in table 6.1 represents 70% of the scannable film. The scanning machines at Brussels, CERN, and UCL use the 514 nm line of the argon-ion laser, while all the other laboratories use the 633 nm line of the helium-neon laser. The coordinate data from the latter group is thus compressed in the Z-axis (depth) by a factor of 1.23 (see E324). The optical system used in the recording combined with the refractive index of the freon (1.25) introduces a magnification of 1.1 in the X-Y hologram plane, and a magnification of 1.0 in the X-Z and Y-Z planes. A correction for these factors was applied in the analysis program.

6.1.1 The Identification of Secondary Activities

The use of a dense liquid, with its short radiation length (280 mm), in the bubble chamber lead to a large number of gamma conversions arising from the decay of neutral pions. These conversions are only distinguishable from a neutral decay to two charged particles by the appearance of multiple scattering, or of a zero opening angle. Misidentified gamma conversions are assumed to be a serious contamination in the V2 decay category. The large number of gamma conversions make it possible for an electron-positron pair to overlap a track from the primary vertex so that it is identified as a K3 topology if the multiple scattering is not visible. The probability of this occuring is inversely proportional to distance from the production vertex.

Multiple scattering and single large angle scatters of low energy pions or delta electrons can be misidentified as K1 decays. For this reason it was important to follow the track from a K1 decay out of the "Charm box" (L < 1400 microns) to determine if there were any further scatters.

Secondary interactions occur in considerable number and are easily identified if a backward track or highly ionising stub can be seen. If the stub is missed and all the other tracks are minimum ionising and forward going then the interaction will be assigned to a decay topology. Interactions on neutrons in the chamber will result in an invisible recoil track.

Individual decay topologies can also be contaminated by overlaps of real decays upon minimum ionising tracks from the primary vertex. Thus V2 decays can appear in the K3 category, and V4 decays in the K5 category. For charm decays with their short decay length this is a significant problem as the narrow cone of tracks from the primary vertex results in a significant probability of overlap. In the decay of the $D^{*+}(2010)$, in its largest decay fraction to $D^0\pi^+$, the very small Q^2 of the reaction leads to the decaying D^0 overlapping the produced π^+ track. The D^{*+} decay length is too short for it to be seen.

6.2 Hologram Measurement Errors

There are several sources of error that can affect the accuracy of the data from the scanning table, some are table dependent such as stage alignment and laser beam collimation, some operator dependent, and some are common to all the holograms as they are a feature of the recording.

6.2.1 Stage and Optical Alignment Errors

These errors are independent of the operator or of the quality of the film being scanned and arise from imperfect alignment of the stages and misalignment of the optical system. The degree of stage misalignment in the Brussels table and HOLMES at CERN is not known to me, but it is assumed to be insignificant. Stage alignment in CHIMAERA posed several problems mainly due to the lack of external reference surfaces on the stages. The maximum misalignment errors in CHIMAERA were:

Z-Stage parallel to optical axis	1 mrad
X-Stage orthogonal to Z-Stage	2 mrad
X-Stage orthogonal to Y-Stage	250 μrad
Z-Stage orthogonal to Y-Stage	2 mrad

The much smaller error in the alignment of the X and Y stages is due to the adjustments built into the Y-Stage mount.

Imperfections in the collimation of the laser beam lead to a varying longitudinal hologram magnification, the CHIMAERA laser beam was collimated to within 250 μrad.

6.2.2 Measurement Errors

These can be split into two groups; measurements in the X-Y plane and measurements along the Z-axis.

The measurement errors in the X-Y plane were small and constant for all tracks where the bubbles could be clearly seen. Measurements of tracks at Brussels and at UCL showed that the r.m.s. spread of the residuals about a least-squares fitted line were comparable with a bubble diameter.

Brussels:	6 μm residuals (1 s.d.)
UCL:	7.3 μm residuals (1 s.d.)

This error is made up of two parts, one is the error in measuring the centre of a 10 micron bubble, the other is due to the spread in the bubble centres themselves.

The Z-axis errors are complicated by the presence of a large amount of field curvature introduced by the ERASME and field lenses. These distortions were parameterised by Tavernier (Personal communication (1983)) from measurements of 41 beam tracks. The measured points were assumed to be related to the true points by:

E601
$$x_m = x_t + D_{xy}.R.(x_t - x_a)$$
$$y_m = y_t + D_{xy}.R.(y_t - y_a)$$
$$z_m = z_t + D_{xy}R^2$$

where $R^2 = [(x_t - x_a)^2 + (y_t - y_a)^2]$

The optical axis was located at (x_a , y_a) where the origin was the position of fiducial F32 in a coordinate system where the X-axis lay along the beam direction increasing in the down stream direction, and the Y-axis was positive in going from fiducial F22 to F32.

From a simultaneous fit to all the measured tracks the values of the parameters were

$$x_a = 25416\ \mu m$$
$$y_a = -20054\ \mu m$$
$$D_{xy} = 1.42\times10^{-7}\ \mu m^{-1}$$
$$D_z = 1.00\times10^{-7}\ \mu m^{-1}$$

The equations in E601 must be solved iteratively, but they converge after two iterations in practice.

After correction the Z-axis residuals about a least squares fitted line in the X-Z plane were found to be:

Brussels:	120 μm	(1 s.d.)
UCL:	160 μm	(1 s.d.)

These much larger residuals are accounted for by the problems of accurately focussing on individual bubbles as discussed in chapter 3 section 3.4.1.

Some distortion remains after these corrections have been applied, but it is not significant in the analysis of the data. These distortion corrections are applied to the data sets appropriately scaled by the table least count and wavelength factor in the Off-line analysis program.

The positions of four or five fiducial crosses were attached to each frame. In most of the laboratories only one fiducial was actually measured per frame, the other fiducials being calculated by offsets derived from a measurement of all four at the start of the scanning session. At UCL five fiducials were individually measured for each frame; this eliminated the effects of film rotation between frames which would have affected the distortion corrections. At UCL I found that the accuracy of measurement of the fiducials was independent of their quality except in the case of very poor frames. The 1 s.d. error in Z taken from 500 frames measured by the operators under normal scanning conditions was 220 microns for the difference between fiducial F22 and F23, which are separated in depth by 650 microns. On CHIMAERA fiducial F32 was partially obscured by the edge of the film holder and was thus of very poor quality and only the X and Y position of this fiducial was measured the Z position being estimated from the other fiducials.

6.3 Kink Detection

The most dificult decay topology to detect systematically was the K1, that is a charged track which kinks. Large kink angles (> 100 mrad) can be easily seen by visual inspection during a general scan of the frame, but small angle kinks must be searched for systematically. The various scanning machines in the collaboration illustrate the differing approaches taken to kink detection.

1) Visual: Brussels
2) Electronic: CERN
3) Measurement: Vienna and UCL
4) Mechanical: Bari and CERN
5) Optical: UCL (Proposed)

6.3.1 Visual Detection

The direct projection Brussels table used the well tried and tested method of sighting along a track to detect kinks and multiple scatters. When a suspected kink was found the track segments before and after the kink were checked with a metal rule to confirm the kink vertex. This method of detection is sensitive and accurate, but only applicable to a direct projection table.

6.3.2 Electronic Detection

The HOLMES machine at CERN used two cursor crosses generated under computer control and mixed with the spatially filtered low magnification image. These moved with the image when the stages were moved by the operator such that any line going through both cursors also passed through a fixed origin, usually chosen to be the primary vertex. Any deviation in the track being followed showed up as an increasing misalignment when the track is compared with the cursors. This has proved to be a systematic, sensitive and rapid kink detection technique, which detects a kink and locates the kink vertex. The HOLMES machine could also use a mechanical variant of the above technique, which is descibed in section 6.3.4.

6.3.3. On-line Track Measurement

This is the most obvious improvement on visual scanning on a camera machine, but is time consuming. Every track has two or more points measured on it and a line is fitted through their projections onto the X-Y plane. If the track does not kink then the fitted line will pass close to the primary vertex. In the case of a track that has kinked a line fitted through points measured following the kink will have an impact parameter different from zero at the vertex. The impact paramter must be divided by the error on the impact parameter to allow for inaccuracies in the measurements. On CHIMAERA 5 or 6 points were measured on each track starting from 10 mm away from the primary vertex. The impact parameter at a plane 10 mm from the primary vertex was calculated and divided by the error. If the resulting value was greater than 3 the track was a kink candidate in the region 0 to 10 mm. From the results of several measurements on undeviating tracks I calculated that impact parameters at the primary vertex down to 25 microns could be detected. The errors on the impact parameters were normally distributed as expected, and the typical 1 standard deviation error was 7 microns. This technique has two disadvantages, firstly it is time consuming to measure five points on every track, and secondly it only locates the track which kinks, the kink vertex must still be searched for by eye.

6.3.4 Mechanical Detection

The Bari table used an interesting method of kink detection that relied upon the integrating effect of the camera tube and human eye. The entire X-Y stage assembly could be pivoted about its centre and translated along the original X-axis direction by hand. Thus a track at an angle to the beam track could be followed rapidly back and forth along its length. The integration effect of the viewing system allowed this track and any others parallel to it to be easily seen on the video monitor, but tracks at other angles became faint or invisible during the motion. This effect was the basis for a rapid and sensitive method of kink location. At the point where the track kinked the track would dissapear, or become much fainter.

The HOLMES table also used a mechanical method of kink detection, similar to the electronic two cursor technique discussed in section 6.3.2. In this case the cursor was fixed and the X and Y Stages were driven in a direction determined by a line fitted between two points on the track. This method complimented the two cursor method but was slower to use, due to the requirement of measuring two points on every track.

6.3.5 Optical Detection

The CHIMAERA machine was designed to incorporate a Dove prism to allow the image to be rotated about the optical axis. This will allow an optical method of kink detection to be used. In the intermediate image plane of the low magnification optical system following the 180 mm lens a cross-wire made of 10 micron gold-plated tungsten wire will be placed. This provides two reference straight lines. By suitable rotation and translation of the image every track can be compared against one of these lines. If the wire overlaps the track along its length then the track does not kink, otherwise a divergence will be apparent. Assuming that about 9 mm of track will be seen and allowing 4 mm of track to act as a reference kinks should be detectable down to around 5 mrad or a little better. The distortions introduced by the camera and monitiors are irrelevant as the cross-wires suffer the same distortions. This method should be much quicker than point measuring, and will additionaly locate the kink vertex.

6.4 The Off-line Analysis

The Off-line analysis program was written by O.R.Williams at UCL, and is described in detail in Williams (1984). A brief description is given in this section. The program was written in FORTRAN 77 and ran under VAX-VMS on the CERN "BESSY" VAX, and the VAX 11-750 in the Physics Department at UCL.

6.4.1 The Off-line Analysis Program

This program read in a number of data files written in the standard CERN data format. If there were no fiducials or the wrong muon category the frame was not analysed further. If the frame was accepted, the distance between the predicted beam track and the measured position was calculated in Y and Z so that the error in finding the prediction could be calculated. If a primary vertex was present the table coordinate system was transformed to a new system, rotated so that the new X axis lay along the beam track with the origin at the primary vertex. Figure 6.1 illustrates the event coordinate system. In this coordinate system the lengths and angles used in the analysis were calculated for all the secondary activity on the frame. The data was corrected for the lens distortions and for the different laser wavelengths used. Various geometrical cuts could be imposed upon the secondary topologies, these were chosen separately for the K1, V2, Kn, and Vn categories of decays. The parameters that could be varied were:

1) Lx(max): the maximum length projected onto the X-axis

2) Lt(max): = Lsin(θ_p) where θ_p is the production angle. For the events analysed Lt was approximated by Ly.

3) Lx.sin(θ_D) (max): the maximum projected impact parameter

4) θ_D (min): the minimum kink or decay angle

5) θ_D (max): the maximum kink or opening angle

Histograms of the interactions and the gamma topologies were also produced as well as other plots showing primary multiplicity, prediction accuracy etc. In addition to the histograms a complete output list was

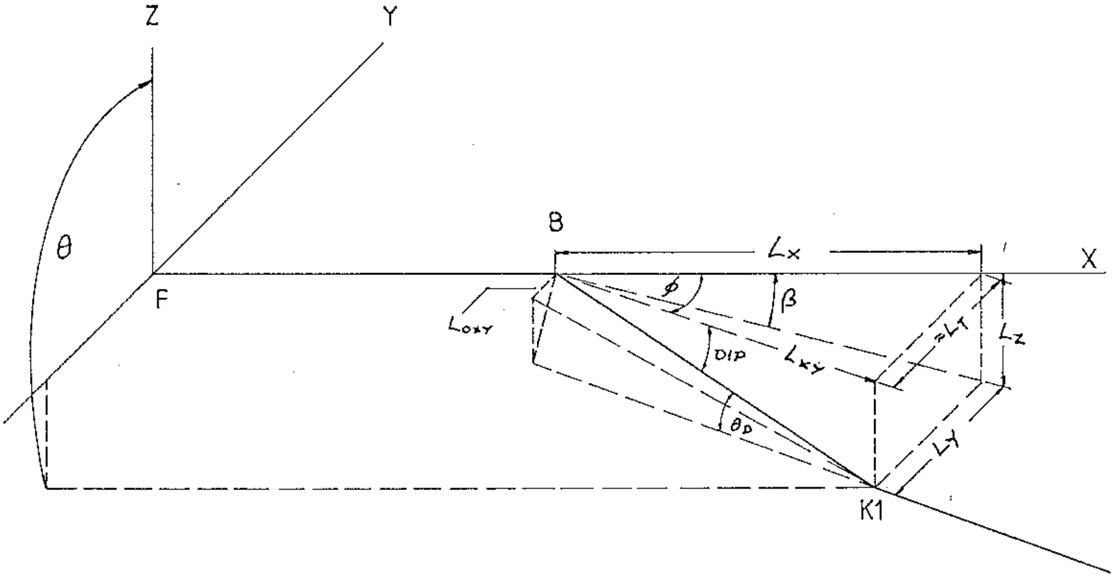

θ_D Decay Angle

θ_P Production Angle Projected Onto XY Plane: φ

XZ Plane: β

YZ Plane: θ

Offset Parameters: $L_0 = L\sin(\theta_D)$

$L_T = L\sin(\theta_P)$

Figure 6.1 Off-line Analysis Coordinate System available for every frame with all the lengths and angles tabulated, thus Lt(z) was available allowing a cut to be made on the transverse decay length projected onto the Z-axis. An overall cut of Lt < 1400 microns was applied to all the data in the absence of a more restrictive cut.

6.5 Results

The discussion of the results is preceded by a description of a Monte Carlo simulation of the expected charm production distributions. This Monte Carlo was written in Brussels by Cobbaert. The assumptions, sensitivity to the choice of production model, and the results from the simulation are discussed in section 6.5.1. The selection of the cuts which were applied to the data are also discussed in section 6.5.1. In section 6.5.2 the problems of the varying visibility of the decay topologies and methods of estimating the visibility function are discussed. Corrections to the data for the effects of the cuts in Lt and Lx are described. The backgrounds in each topology are discussed. In section 6.5.3 the data from CERN and Brussels are compared and the differences discussed. In section 6.5.4 a new method of calculating the charm production cross section is described and compared with the results of Williams (1984).

6.5.1 The Monte Carlo Simulation

A Monte Carlo simulation of the NA25 experiment was written by Cobbaert in Brussels. Two different production models were used and the effects of varying the parameters was investigated.

6.5.1.1 Production Models

In uncorrelated production the $C\bar{C}$ pair consists of two independently created particles. The differential cross section used was:

E602 $$\frac{d^3\sigma}{dx\,dp_T^2} = (1 - |x_F|)^a e^{-bp_T^2}$$

with a = 1.8, b = 1.1 $(GeV/c)^{-2}$

These values were obtained from a best fit to D meson data. A small amount of correlation does exist between the C and $\overline{C}$ due to energy and momentum conservation.

In the correlated production model, the C and C are assumed to arise from the decay of a virtual particle generated according to E602. The mass distribution of this paricle was given by:

E603 $$\frac{d\sigma}{dM} = e^{-8(M - \sum_{i=1}^{2} m_i)}$$

with M in GeV and m_i the masses of the two charmed particles. In this model the C $\overline{C}$ have a tendency to go out in the same direction.

The purely leptonic decay modes were neglected, and Trilling (1981) was the source of most of the branching ratios used. The muonic and electronic branching ratios were assumed to be equal. The other perticles produced in the interaction, which have an effect on the detectability of the charmed decays, were assumed to be pions. Their average multiplicity was reproduced using a K.N.O. scaling function and energy conservation.

6.5.1.2 The Experiment

The experiment was reduced to the beam dump, the Bari chambers, and H1 and H2. Neglecting multiple scattering in the dump, a muon was assumed to go through the tungsten if its production angle (α) was less than 54 mrad. A signal in the Bari chambers was defined as a muon if 8 out of the 9 planes were hit combined with a hit in H1 or H2 depending on the muon definition used. Cobbaert assumed only hits in H1 in his simulation. The threshold muon energies were:

6.11 GeV ($\alpha < 54$ mrad)
3.21 GeV ($\alpha \geqslant 54$ mrad)

The experiment triggered on muons, thus at least one of the produced charmed particles must decay semi-leptonically.

6.5.1.3. Results from the Monte Carlo

An investigation of the effect on the calculated acceptance of Λ_c^+ production was made. At 360 GeV incident proton energy the acceptance was 9.5% with no Λ_c^+ , 6.5% with 1 Λ_c^+ , and 3.5% with 2 Λ_c^+ produced. These values were calculated using the uncorrelated model.

The sensitivity of the Monte Carlo to variations in the production parameters was investigated at 200 GeV. Varying the parameters "a" by a factor of 2 and "b" by a factor of 2 changed the acceptance by a maximum of 3%.

Allowing decays of D mesons via the K*(892) channel resulted in a 3% increase in the acceptance over the reference model. The Monte Carlo generated distributions for the K1 and V2 topologies are shown in figures 6.2 and 6.3.

6.5.2 Background and Visibility Considerations

6.5.2.1 Topological Backgrounds

The backgrounds contaminating the charm decay sample arise from two causes. Firstly, as described in section

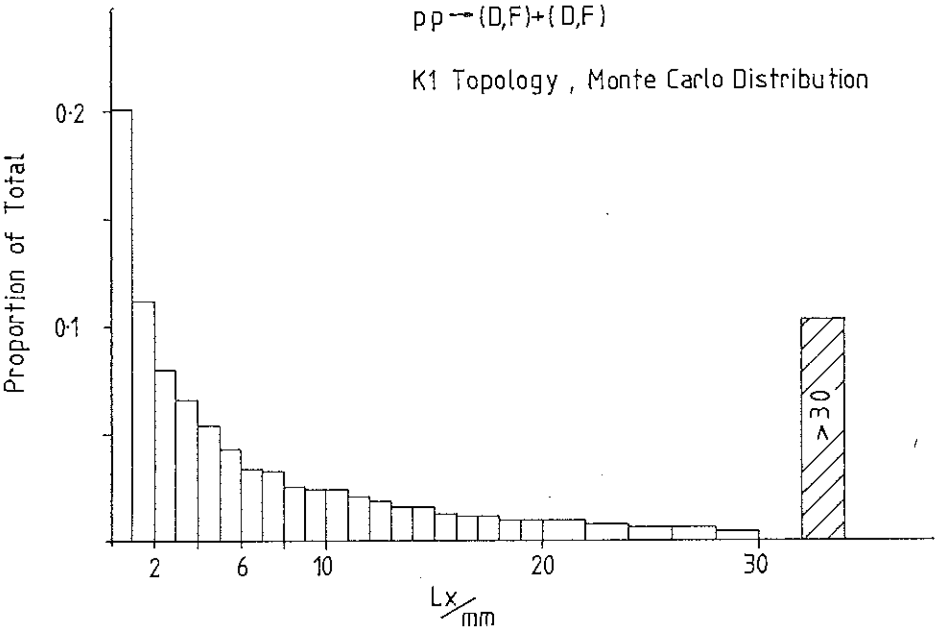

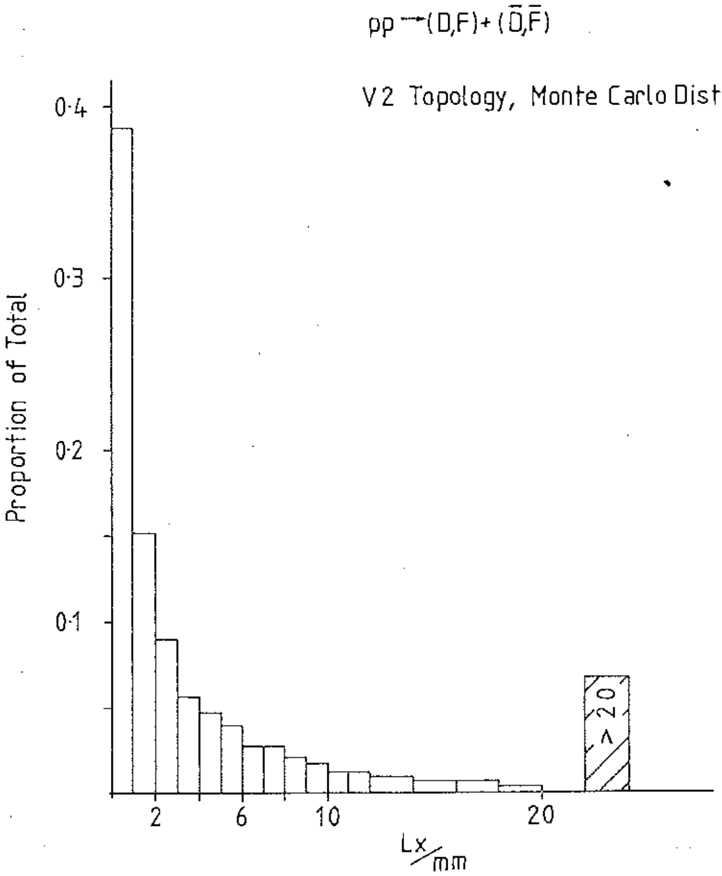

Figure 6.2 Monte Carlo Lx Distribution for K1, V2 Topologies

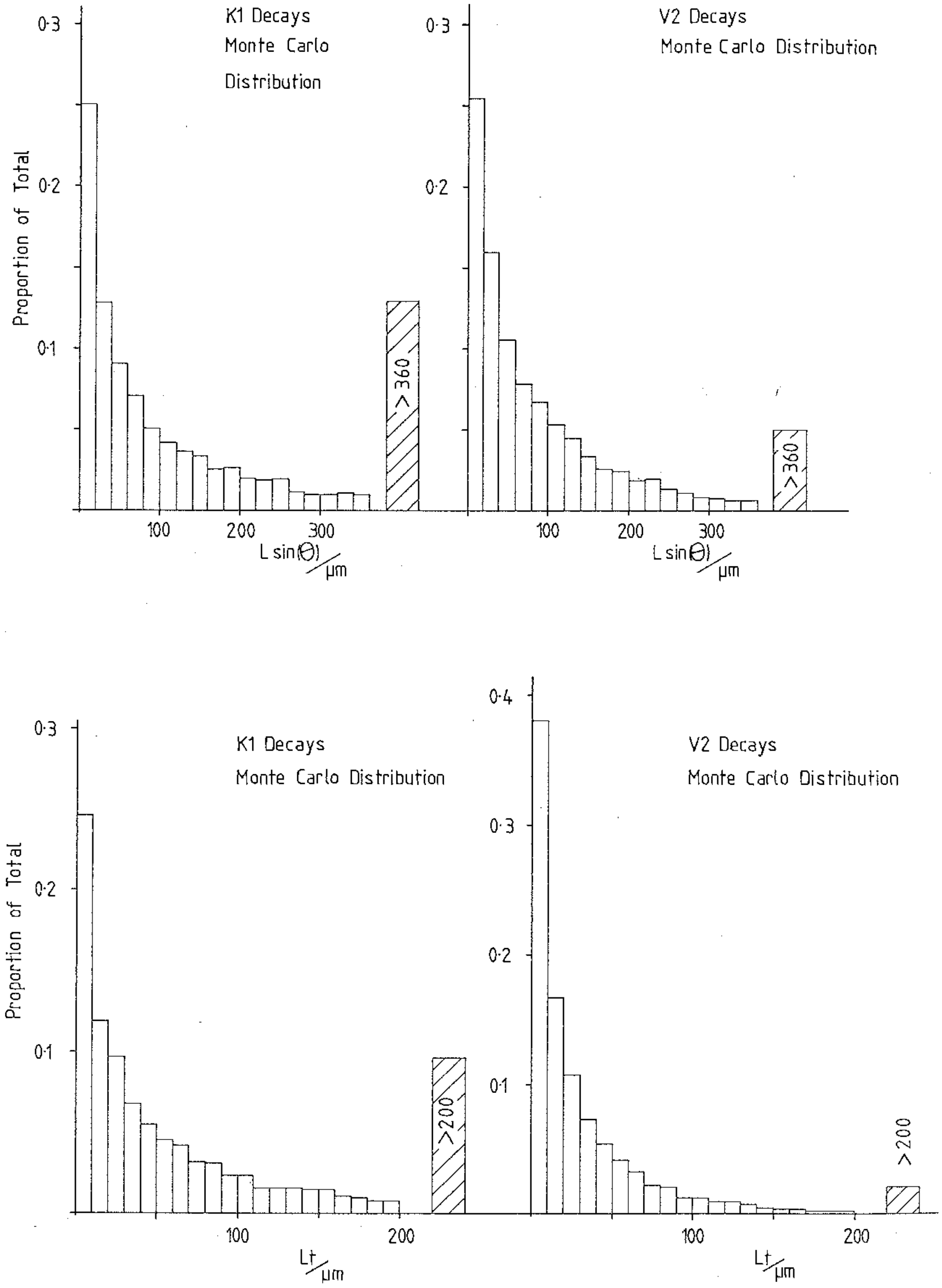

Figure 6.3 Monte Carlo Lsin(Θ) and Lt Distributions for K1, V2 Topologies

6.1.1, there are misidentified gamma conversions and interactions. Secondly there are genuine decays coming mainly from strange particles. Some of the decay topologies are more susceptible to contamination than others, and for this reason the backgrounds in each topology will be discussed separately.

2-prong Neutral Decays V2

A large number of the two prong decays are due to misidentified gamma conversions, and the decays of K^o_S and Λ^o particles. These backgrounds are expected to be unifromly distributed with Lx. The gamma conversions can be removed to a large extent by applying an opening angle cut, however this also removes a large fraction of the charm decays in this topology. Another source of background is due to a secondary interaction of a neutral particle (n, K, Λ) emitted from the primary vertex, where no nuclear recoil or nuclear fragments were seen.

4-prong Neutral Decays V4

Very few strange decays can contribute a background in this topology, although the rare process

$$K^o_L \;\text{-->}\; \pi^+ \pi^- \underset{\displaystyle \llcorner\!\rightarrow e^+ e^- \gamma}{\pi^o}$$

could contribute in principle. Misidentified interactions could provide some background. This topology is expected to be fairly clean.

1-prong Charged Decays K1

The backgrounds in this topology come from K decay, $\Sigma^{\pm}$ decay and scattering of slow pions. The strange decay background can be reduced by a cut in transverse decay length (Lt). Large angle single scatters are very rare, I estimate that only 1 primary interaction per 1000 will produce a pion which will single scatter with an angle greater than 10 mrad in the region Lt < 500 microns. Multiple scattering can be missed if the track is not scanned carefully enough, or is in a region of low visibility. A cut on kink angle will remove most of the contribution from scattering, but this does result in a considerable reduction in the number of charm decays accepted.

3-prong Charged Decays K3

The decays of strange particles into 3 charged particles are a small fraction of all strange decays, and are thus a smaller background in the K3 topology than in the K1. A background that is expected to be significant is that of V2 decays from Λ^0 or K^0_S particles overlapping a charged track from the primary vertex. The probability of this ocurring is inversely proportional to Lx. Overlying gamma conversions can also contribute, although these should be removed by a minimum opening angle cut. There will be some background from interactions in which the short prong was missed. Considered topologically there is a contamination from charmed decays coincident with a loss in the V2 category, arising from the decay

$$
\begin{array}{l}
D^{*+} \longrightarrow D^0 \; \pi^+ \\
\qquad\quad \hookrightarrow K^- \; \pi^+ \; \text{etc.}
\end{array}
$$

The decay of the D* has a very small Q^2 and the D^0 will continue in the same direction as the pion, thus the D^0 decay will overlap the pion track changing a V2 into a K3. The D* production cross section was measured by NA16 who found it to be of the same order as the D production cross section (see chapter 1, section 1.5.3).

5-prong Charged Decays K5

The only non-charmed background in this toplogy is due to interactions that have been misidentified. Charmed decays to V4 have a significant probability of overlapping a track from the primary vertex and becoming K5 topologies.

6.5.2.2 Corrections for Length Cuts

Applying geometric cuts to the data in Lt or Lx biases the data with respect to Lx or Lxy. A cut in Lx was inevitable due to the finite length of the chamber, and strict cuts in Lt were used for reasons outlined in section 6.5.2.1. The correction factors that should be applied to the data are discussed in this section.

The scanning rules demanded that every primary interaction that was scanned for secondary activity had at least 10 mm of scannable film (in Lx) following the primary vertex. This means that no Lx correction is needed for the region $0 \leqslant Lx \leqslant 10$ mm. The primary vertices were distributed more or less evenly throughout the fiducial length, thus imposing a maximum visible Lx length of about 95 mm. I have assumed that the number of events with a visible Lx > 10 mm decreased linearly until Lx = 95 mm, resulting in the following correction factor:

E604
$$\lambda(Lx) = \begin{cases} 1 & Lx < 10 \text{ mm} \\ \dfrac{100}{(112 - 1.18 \times Lx)} & Lx \geqslant 10 \text{ mm} \end{cases}$$

The effect on the noise data of cuts in Lt could only be determined once the angular distribution of the tracks coming from the primary interaction was known. Only charged tracks are visible and I assumed that the distribution of neutral particles was the same as for the charged particles This hypothesis was tested using interaction data. From measurements I made on CHIMAERA of 319 minimum ionising forward going tracks the angular distribution was calculated. The positive and negative angle data were combined. The angular distribution is shown in figure 6.4. From these measurements correction factors for any Lt cut can be calculated. The correction curves for Lt cuts of 1400 microns, 500 microns and 300 microns are shown in figure 6.5.

It was possible to test the validity of the Lx and Lt corrections by looking at the corrected distributions of the secondary interaction data. The corrected distribution is expected to be flat with length apart from a possible small loss at low Lx due to visibility considerations. Figure 6.6 shows the corrected number of interactions as a function of Lxy (Lx ≅ Lxy). The data from the CERN table is compared with the data from the other labs (mainly Brussels). The CERN data is scaled by the ratio of the number of primary interactions scanned. The plot shows the I + N topologies; these consist almost entirely of charged interactions as the most abundantly produced neutral particle, the pion, decays to photons leaving only the much smaller number of neutrons and neutral strange particles to provide neutral interactions. Figure 6.6 also shows the corrected length distribution of the N topology interactions, this confirms the hypothesis that the neutral particle production angle distribution is the same as the charged particle distribution.

Figure 6.6 also shows a significant loss in the CERN data sample compared to the rest of the data at Lx > 20 mm. This loss is also seen in the gamma distributions and the decay topology distributions. I attribute it to a loss of scanning efficiency at large Lx. A correction can be applied to the CERN data to compensate for this effect, the weighted average factors are:

Bin/mm	Percentage Loss (CERN)
20 - 26	9.2 ± 9.8
26 - 32	34.5 ± 9.6
32 - 40	25.0 ± 9.5
40 - 50	35.1 ± 10.0

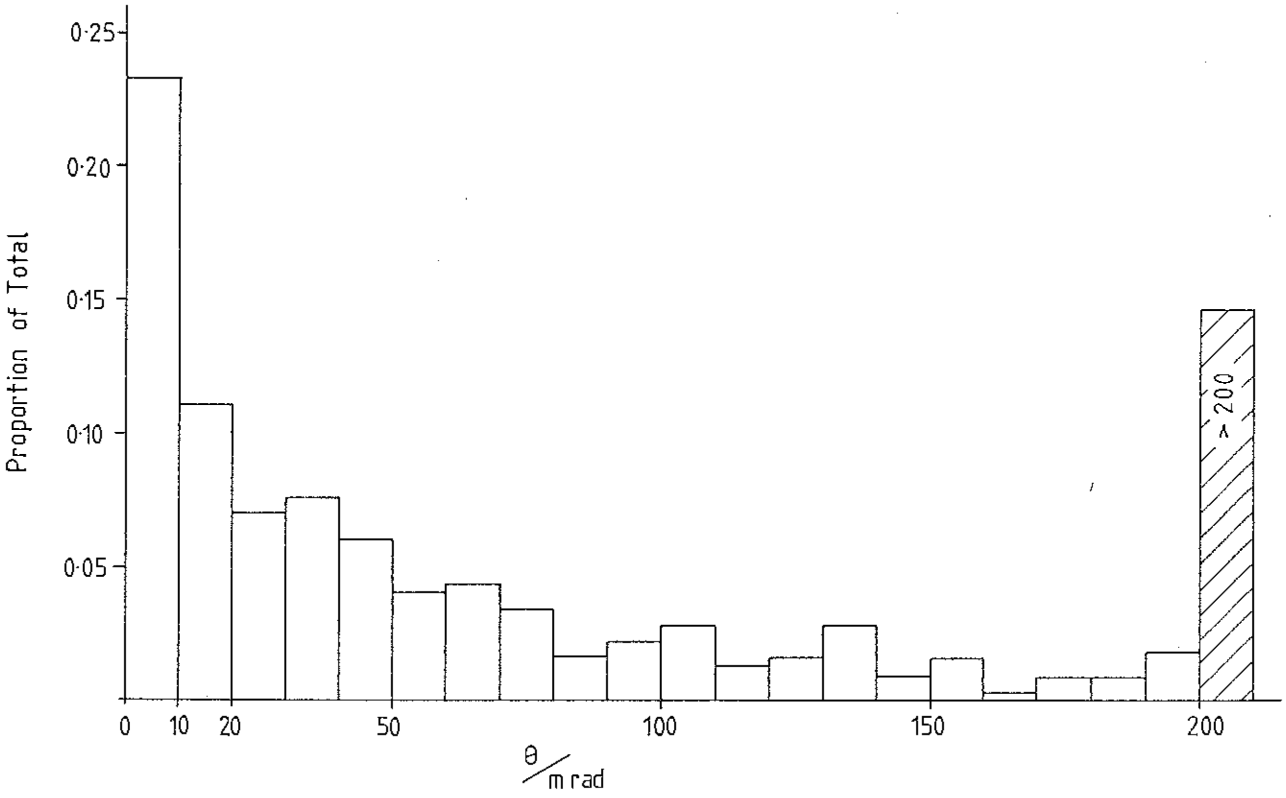

Figure 6.4 Angular Distribution of Tracks from Primary Vertices

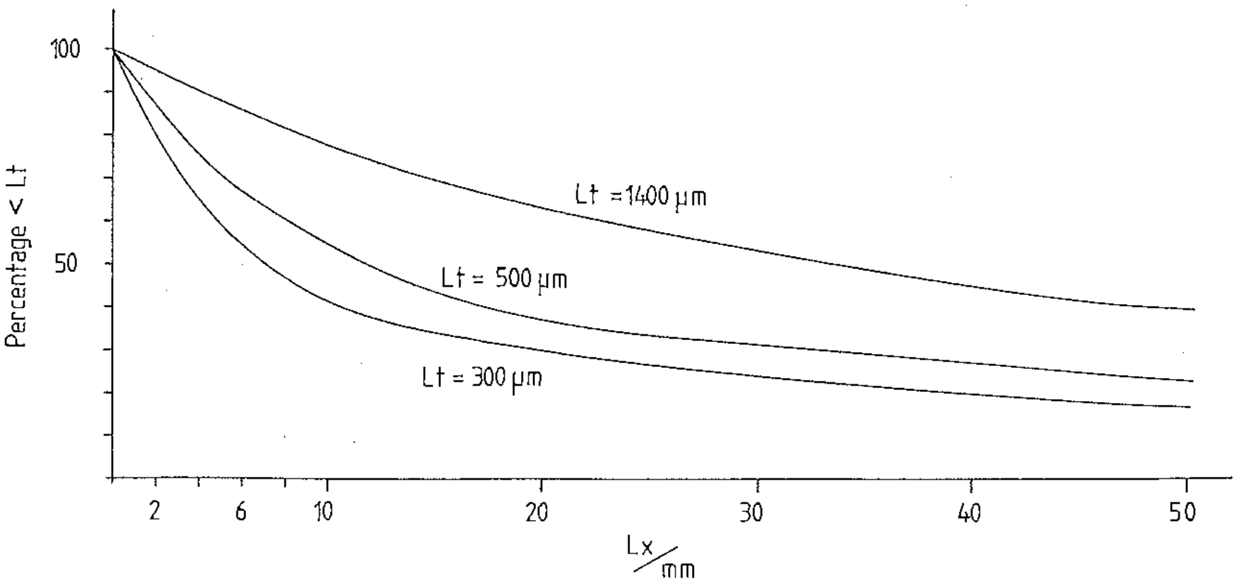

Figure 6.5 Correction Curves for Lt Cuts

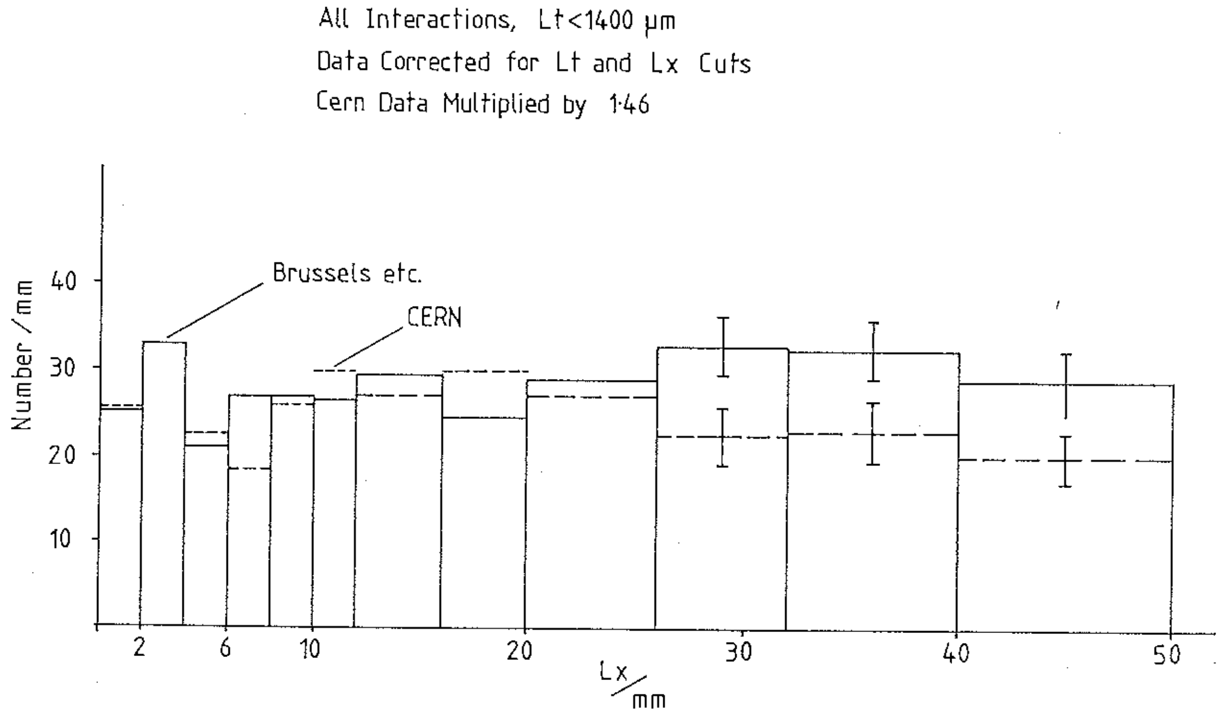

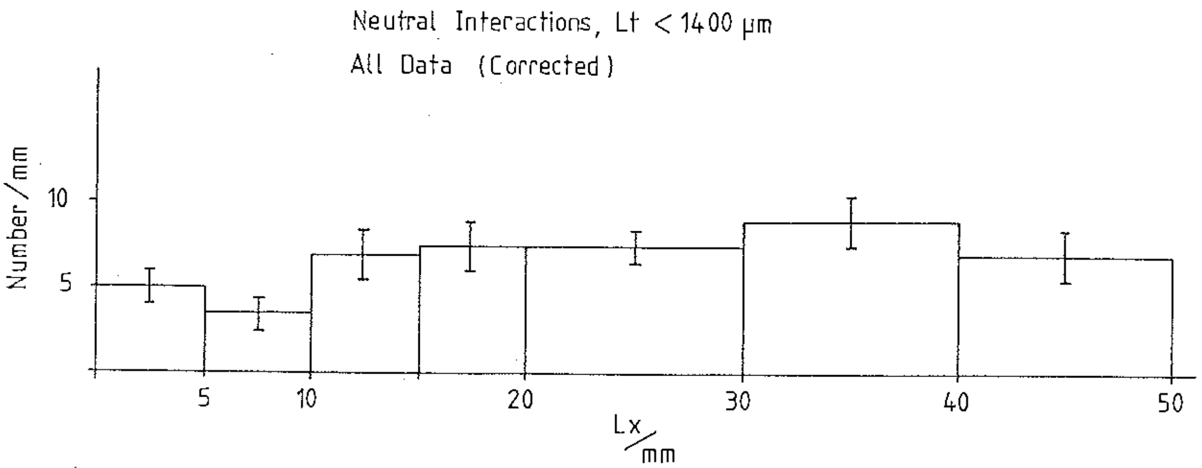

Figure 6.6 Corrected Lx Distributions for Interaction Topologies

In the case of the gamma distributions a further correction factor must be applied to correct for the finite pair conversion length (X_p). This correction is small because the pair conversion length ($9/7X_o$) is 360 mm for the freon. The correction factor is 1.13 at Lx = 45 mm.

6.5.2.3 Correction for Visibility

The high primary multiplicites at the incident hadron energies used in NA25 combined with the short proper lifetimes of charmed particles result in a loss of data at short distances due to the obscuration effect of other tracks. This obscuration varies with Lx and is negligible for Lx > 10 mm. This loss of data is not accounted for in a traditional estimate of scanning losses where the probability of seeing any event is assumed to be constant. It was important to correct for the visibility loss in the calculation of the charm production cross section. Tavernier and Giergat (Personal communication (1984)) have calculated a visibility parameter for the data scanned on the Brussels table and the first data (rolls 9/10) scanned at CERN. They took a very clean sample of events where two decays satisfying the cuts in table 6.2 were found.

They assumed that the visibility function was of the following form:

E605 $$V(Lx) = 1 - \exp(-\beta Lx)$$

where β [mm^{-1}] was determined by a maximum likelihood fit to the experimental distribution, and the comparison data was provided by the Monte Carlo. The likelihood function used was

E606 $$P_1(l_n , l_n , \ldots , l_n , \beta) = \prod_{k=1}^{37} f'_{n_k}(\beta)$$

TABLE 6.2
CHARM DECAY CUTS

Decay Topology	Cut
K1	Lt < 500 μm
K3, K5	Lt < 500 μm
V2	Lt < 300 μm
V4	Lt < 300 μm
K1	L $\sin(\theta_D)$ < 1000 μm
K3, K5	L $\sin(\theta_D)$ < 2000 μm
V2, V4	L $\sin(\theta_D)$ < 1000 μm
K1	θ_D > 10 mrad
K3, K5	θ_0 > 5 mrad
V2	θ_0 > 10 mrad
V4	θ_0 > 5 mrad

---

where n_k = bin number of decay k ($1 \leq n_k \leq 100$)

$$f'_{n_k}(\beta) = \frac{f_{n_k}(1 - \exp(-\beta l_{n_k})}{\sum_{n_k=1}^{100} f_{n_k}(1 - \exp(-\beta l_{n_k})}$$

where l_{n_k}= Lx value in the middle of bin n_k , and f_{n_k} = Monte Carlo Lx distribution of the charm single decays. The upper limit of 37 in the product in E606 comes from the 18 "double" decays containing 37 individual decay events. Maximising $\ln(P_l(\beta))$ gives the best estimate of the parameter β . To account for the small background still present in the doubles data, Tavernier and Giergat estimated the background from the single decay topologies after subtraction of the decays found in the double decay category:

$$\text{E607} \qquad N_{ch,s} = 2N_{c\bar{c}}.A_s - 2N_{c\bar{c}}.A_s^2$$

where $A = \overline{C}.\overline{V}.V_\infty$ is the scan acceptance, $\overline{C}$ = the average cuts acceptance, $\overline{V}$ = the average visiblity, V_∞ is the scanning efficiency, and $N_{c\bar{c}}$ = the real number of produced charm pairs. The first term in E607 represents the number of single charm decays and the second number gives the number of charm pairs seen in the doubles sample, thus:

E608 $N_{ch,s} = 2N_{ch,d}(1 - A_s)/A_s$

This correction term was subtracted bin by bin from the normalised Monte Carlo distribution and a new maximum likelihood calculation was performed for various values of β (A is a function of β). The result of this calculation, using a Monte Carlo taking the cuts on the data into account, was

β =	0.613	(0.260,2.105)	mm^{-1}	1-unit support
	0.613	(0.188,6.00)	mm^{-1}	2-unit support

where the values quoted are the value of maximum likelihood and the 1-unit and 2-unit support values (Edwards (1972)). These are the parameter values astride the evaluate at which the support function is 1 and 2 units less than its maximum value.

There is a significant difference in the number of decay topologies found in the CERN scanned data from the second data taking run and the other data. When the number of decays is compared with the data from film scanned at Brussels and the other laboratories significant losses can be seen in the CERN data. Table 6.3 compares the two data sets after the cuts of table 6.2 have been applied (No Lsin(θ) cut).

Even after scaling the CERN data by the ratio of primary interactions scanned there are significant losses in the K1 and V2 decay topologies. V2 decays could be wrongly assigned to the gamma decay category, but the CERN data shows no corresponding enhancement. The number of gamma conversions and secondary interactions is entirely compatible between the two data sets, the slight loss in the CERN data can be attributed to a loss at large Lx. The number of decays in the K3, K5 and V4 categories are equal in the two samples. The losses in the K1 and V2 categories

TABLE 6.3

COMPARISON OF BRUSSELS AND CERN DATA

Toplogy	Brussels etc.	CERN	CERN×1.46
V2	30	11	16
V4	3	1	1.5
K1	70	29	42
K3	11	9	13
K5	4	4	6
Gamma	390	257	376
Interaction	399	248	367
Doubles	13	2	3

can be attributed to the poorer visibility of the primary interactions when scanned on HOLMES at CERN. The halving of the average visibility is confirmed by the observation of only a quarter as many double decays. The higher multiplicity decays are more visible and consequently show no losses.

The calculation of a visibility parameter for the CERN data is complicated by the presence of real charm decays in any sample of data that can be used. This will lead to an overestimation of β. A direct scaling between the two data samples by comparing the visibility of the gamma conversions has proved to be impossible due to the higher gamma visibility compared to V2 decays in the Brussels data. In the CERN data sample these two categories show similar loss characteristics. In the Brussels sample the losses are not similar, probably due to the Brussels table showing a larger fraction of the event than HOLMES. This might enable gamma conversions that originate close to the primary vertex to be detected at long distances and followed back to their vertex.

An estimate of β for CERN data was obtained by considering a sample of K1 and V2 decays with Lt < 1400 microns, Lx < 20 mm, and with no other cuts. This sample contains charm but has a low signal to noise ratio. The data was corrected for the Lt cut and the Lx cut, and then each bin was divided by the visibility function V(Lx) given in E605. The parameter β was varied until a weighted least squares fit resulted in a straight line with zero gradient. This flat distribution is what is expected if all the decays are noise. The value of β obtained was:

$$\beta(\mathrm{CERN}) = 0.299 \pm 0.026$$

As an estimate of the charm visibility this value will be too large due to a fit on data with Lt < 1400 microns, when charm is confined to the regions Lt < 500/300 microns for charged/neutral decays. The additional decays in the data sample used to calculate β have a higher visibility than charm decays. The presence of real charm decays will also tend to over estimate β. Fitting to data with no angle cuts but with the "charm" Lt cuts is also unreliable due to the presence of charm and the small number of decays in the sample. The effect of this visibility correction on the CERN data is shown in figure 6.7 It can be seen that a peak has appeared at small Lx lying above a roughly flat background. There is still some residual loss in the first bin, which should contain the most charm suggesting that the visibility parameter is too big. It has not been possible to estimate a better value for β from the CERN data. The value of β = 0.299 should be regarded as an upper limit.

The considerable uncertainty in an appropriate value for the CERN visibility parameter lead me to reject the

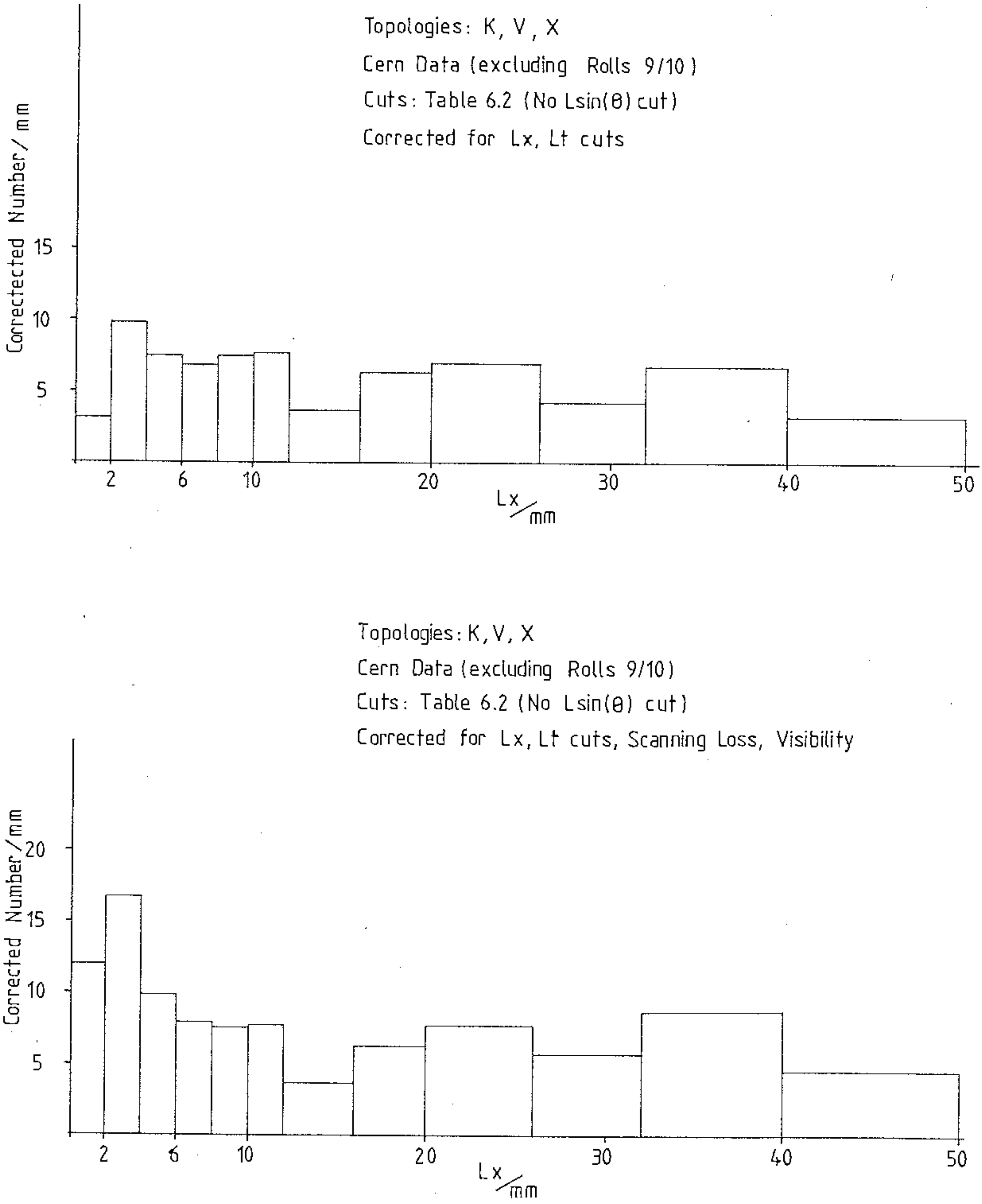

Figure 6.7 Corrected Lx Distribution for Decay Topologies - Cern Data

CERN data (30% of all measured film) from further consideration.

6.5.3 Charm Production Cross Section

The calculation of a charm production cross section requires an understanding of the losses in the data due to the effect of the geometric cuts and the losses due to the visibility. These have been discussed in sections 6.5.2.2 and 6.5.2.3. The conversion of the number of charm decays found, N_c, in a total of N_t analysed, into a cross section is described in section 6.5.3.1. In section 6.5.3.2 a total charm production cross section is calculated from an analysis of the single decays, and this is compared, in section 6.5.3.3, with the cross section calculated by Williams (1984) who used only the double decays.

6.5.3.1 Conversion of Decays into Cross Section

The charm production cross section is given by:

E609 $$\sigma = \frac{\sigma_t \times I.N_c \times R \times A^{(\alpha_I - \alpha_c)}}{N_t \times A_\mu \times A_s} \quad \text{for single decays}$$

$$\sigma = \frac{\sigma_t \times I.N_{c\bar{c}} \times R \times A^{(\alpha_I - \alpha_c)}}{N_t \times A_\mu \times A_s^2} \quad \text{for double decays}$$

where

σ_t is the trigger cross section

$N_c, N_{c\bar{c}}$ are the number of charmed single/double decays

N_t is the total number of primary interactions

R is the ratio of muon triggers to interaction triggers

A_μ	is the acceptance of the muon trigger
A_s	is the scanning acceptance
A	is the average atomic number of the freon (17.1)
α_I	is the exponent for the inelastic cross section
α_c	is the exponent for the charm cross section
I	is a correction factor for non-triggered interactions (I = 1.02)

The trigger cross section is almost identical to the inelastic cross section, which is 33 mb at 360 GeV/c. Each interaction trigger should have greater than 3 minimum ionising particles in S3, and thus there will be some loss of low multiplicity events. In principle one should compare the multiplicities of random triggered events with those in the sample data. The losses for small multiplicities can be estimated from measurements of the toplological cross sections at 360 GeV/c (Bailly et al. (1984))

Topology	σ/σ(total)
2-prong (inelastic)	0.053
4-prong	0.111
6-prong	0.133

We will loose most of the 2-prongs, some of the 4-prongs and a few of the $\geqslant$ 6-prongs. I estimate that the trigger cross section is 30 mb.

The ratio R was calculated (Tavernier personal communication) from scaler data taken during the 1982 run. The effect of back scatter from the dump was taken into account. R(360 GeV) = 0.00457

The acceptance of the muon trigger (A_μ) was calculated using Cobbaert's Monte Carlo; assuming no Λ_c^+ production the acceptance was 0.095. This result is dependent on the average semi-leptonic branching ratio, which was taken as 0.095.

The scanning acceptance, A_s ,consists of three parts. It is the product of the average visibility, the average cuts acceptance for charm, and the scanning efficiency. For the cuts in table 6.2 the cuts acceptance $\overline{C}$ = 0.74 (Muciaccia et al (1984)). For these cuts but omitting the impact parameter cut $\overline{C}$ = 0.77. The average visibility was calculated as described in section 6.5.2.3, this value must be multiplied by a further factor to take into account the conventional Geiger and Marsden scanning efficiency. This factor, V_∞ , was determined from the CERN and Brussels data, in both cases it was found to be 0.95 for Lx > 5 mm, giving

$$\overline{V} = 0.618$$

The exponential factor in the atomic number dependence accounts for the fact that the atomic number dependence of the inelastic cross section (α_I) is different from the atomic number dependence of the charm cross section (α_c). Taking α_I = 0.72 (Carrol et al. (1979)) and α_c = 1.0 then

$$A^{(0.72\ -\ 1)} = 0.452 \quad \text{for } A = 17.1$$

Combining all these factors one arrives at the following cross sections for single and double decays:

E610 $$\sigma_c = \frac{665 \times N_c \times 1}{N_t \quad A_s} \qquad \text{for single decays}$$

$$\sigma_{c\overline{c}} = \frac{665 \times N_{c\overline{c}} \times 1}{N_t \quad A_s^2} \qquad \text{for double decays}$$

6.5.3.2 Cross Section from the Single Decays

My method of calculating the cross section takes the single decay data, which contains a significant amount of noise and is much less clean than the double decay sample, correcting the data for the effects of visibility and the cuts and subtracting the background. The corrections allow a background which is in principle flat over all Lx to be calculated from the decays at large Lx and to be extrapolated into the small Lx region. The assumption that the background is flat is related to the long lifetimes of the strange particles that form the major source of background decays. The hypothesis is that after correction, when the number of decays is plotted against Lx, a decaying charm peak overlying a flat background should be seen. In this analysis no impact parameter cut can be used as this would introduce an unknown bias into the data which I cannot correct for. The region $18 \leq Lx \leq 50$ mm is assumed to be entirely background and contain no charm. A small amount of charm is present, but this is an insignificant bias to the background when averaged over the region. However a correction must be made for the lost charm at $Lx > 18$ mm. A correction factor of 1.07 was calculated from the Monte Carlo distribution of charm decays versus Lx, taking all the decay modes into consideration. The corrections for the Lt cuts, which must be separately applied to the charged and neutral decays, overcorrect the charm which is unaffected by the Lt cuts. Thus the excess above the background must be multiplied by the inverses of the weighted correction factors.

The data sample used consists of all the film scanned at Brussels, the film scanned at Mons, Vienna and UCL, and rolls 9/10 scanned at CERN. This sample contained 2412 primary interactions with a good muon. Using the cuts in table 6.2 (no impact parameter cuts) the distribution of the decays used in the analysis are shown in figure 6.8. The X category decays have an Lt cut of 500 microns and are added to the charged decays. Figure 6.9 shows the distribution of decays after corrections have been applied.

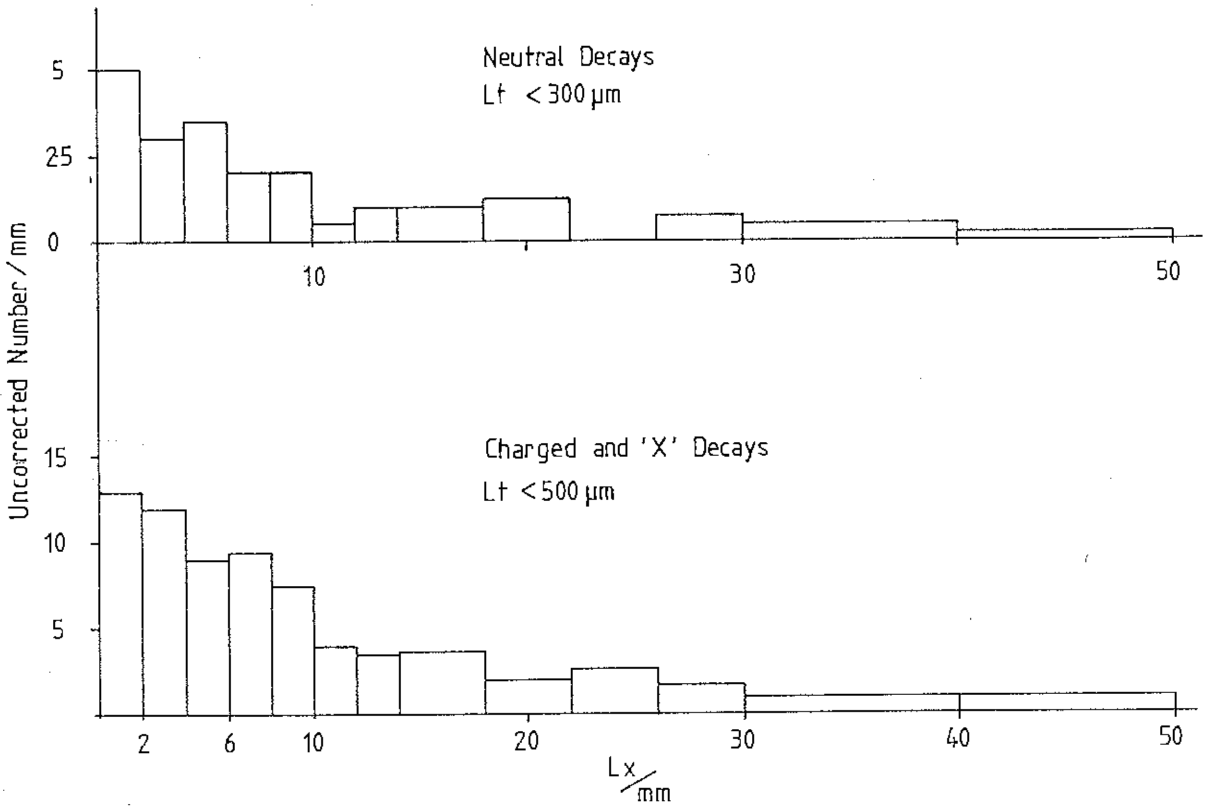

Figure 6.8 Uncorrected Lx Distributions for Decay Topologies – Brussels etc.

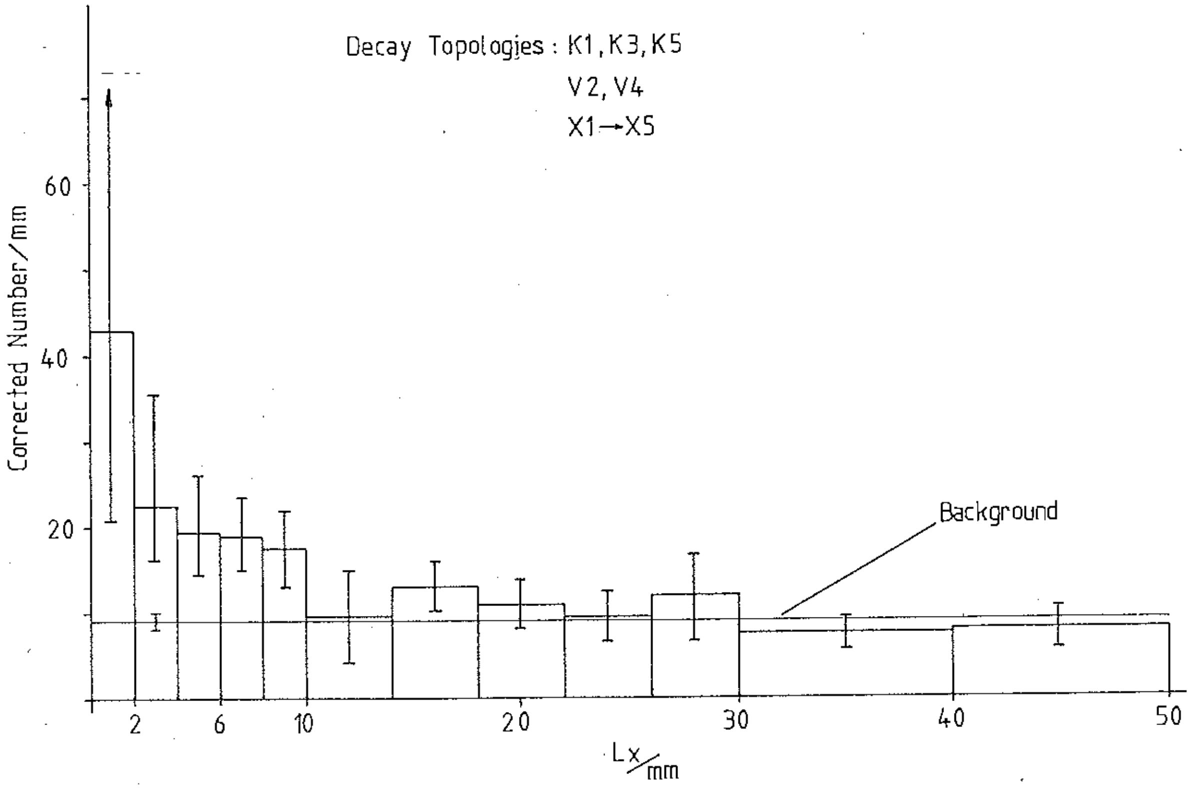

Figure 6.9 Corrected Lx Distributions for Decay Topologies – Brussels etc. Data

The error bars are the transformed 1-unit support limits on the visibilty correction plus the much smaller Poisson errors on each bin added in quadrature.The background was estimated from the decays in the region $18 < Lx < 50$ mm, the value obtained (weighted average) was

8.84 ± 1.28 events/mm

It was assumed that the background was flat over all Lx. Extrapolating to $Lx = 0$ it can be seen that a significant excess above the background exists in the region $0 < Lx < 10$ mm with the shape that one would expect for charm decays. The excess in each bin above the background is shown in table 6.4

TABLE 6.4

UNCORRECTED EXCESS ABOVE BACKGROUND

Bin (mm)	Excess per mm	(1-unit support)
0 - 2	33.98	(77.22 , 12.26)
2 - 4	13.76	(26.83 , 8.13)
4 - 6	10.80	(18.08 , 6.56)
6 - 8	10.17	(15.51 , 6.03)
8 - 10	8.60	(13.20 , 4.42)
10 - 14	0.81	(6.25 , -4.97)
14 - 18	3.91	(5.97 , 0.21)

The excess is assumed to be due to charmed decays. These excesses above background must be multiplied by the inverse of the Lt corrections, because the charm decays are essentially unaffected by the Lt cuts. The Lt factors must be weighted by the relative numbers of neutral and charmed decays present in our data. Assuming that all the charmed particles are D mesons and taking into account the effect of the muon trigger, there are 1.23 neutral D mesons produced to each charged D meson. Weighting the Lt correction factors for each bin by this ratio results in the corrected excesses shown in table 6.5

TABLE 6.5
CORRECTED EXCESS ABOVE BACKGROUND

Bin (mm)	Weighted Lt factor	Corrected Excess / mm	
0 - 2	0.91	30.92	(70.27 , 11.16)
2 - 4	0.75	10.32	(20.12 , 6.10)
4 - 6	0.64	6.92	(11.57 , 4.20)
6 - 8	0.55	5.59	(8.53 , 3.32)
8 - 10	0.49	4.2	(6.47 , 2.17)
10 - 14	0.43	0.3	(2.69 , -2.14)
14 - 18	0.37	1.4	(2.21 , 0.08)

Summing the excesses over all the bins results in a total weighted number of charm decays of

$$N_c = 119.50 \qquad (243.72 , 24.89)$$

These results are insensitive to variations in the ratio of produced neutral to produced charged charmed mesons. Varying the ratio of neutral to charmed decays over the range 0.75 to 1.75 changes the weighted number of events by

± 1.4% with respect to the value obtained with the ratio 1.23.

Inserting the number of events in equation E610 gives the total inclusive charm production cross section. The scanning acceptance A in E610 is just the cuts acceptance in this analysis, as the correction for visibility has already been applied to the data. The resulting cross section is:

$$\sigma = 45.8 \quad (93.4\ ,\ 9.54) \qquad \mu b$$

where 45.8 is the best supported value, and the numbers in parentheses are the transformed 1-unit support limits. These are analogous to the square root of the variance. This method of calculating the errors on the result is the most appropriate for this analysis (Personal communication B. Birkhead U.C.L. (1984)). It is difficult to determine the variance of the population from which β was calculated, and these support limits are an approximation to the variance of the population.

The only assumption inherent in this method of analysis that is difficult to test is that the visibility of the noise decays is the same as the visibility of the charm decays. If the visibility of the noise events was greater than that of the charm, then using the visibility parameter calculated in section 6.5.2.3. would generate a peak at small Lx even in the absence of any charm decays. One feature of a decay that increases its chance of being seen is a large kink or opening angle. In figure 6.10 the distribution of K1 decay kink angles and V2 opening angles with the Lt cuts used in the analysis is compared with the distribution for all decays. The distributions are similar supporting the hypothesis that the excess observed is due to real charm decays and not just due to the effect of the visibility correction.

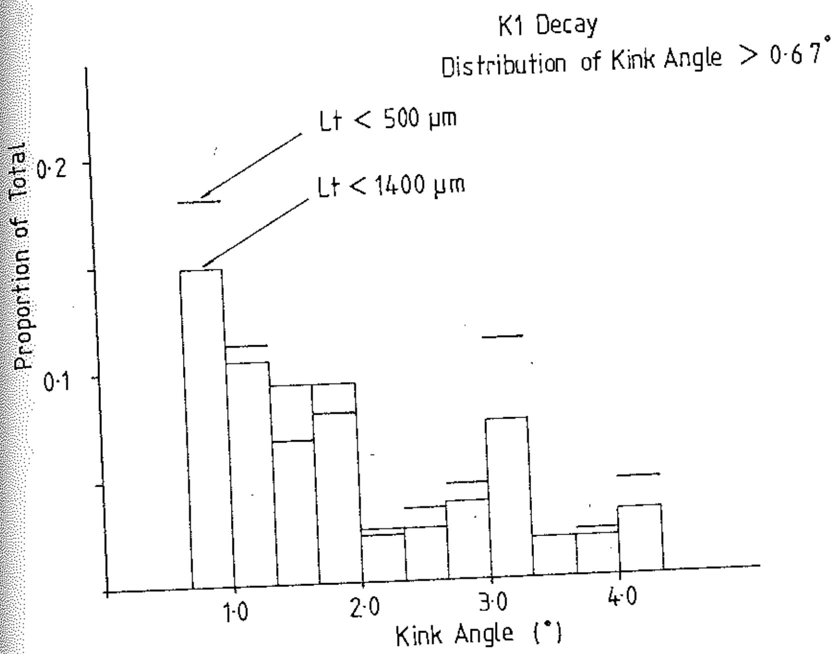

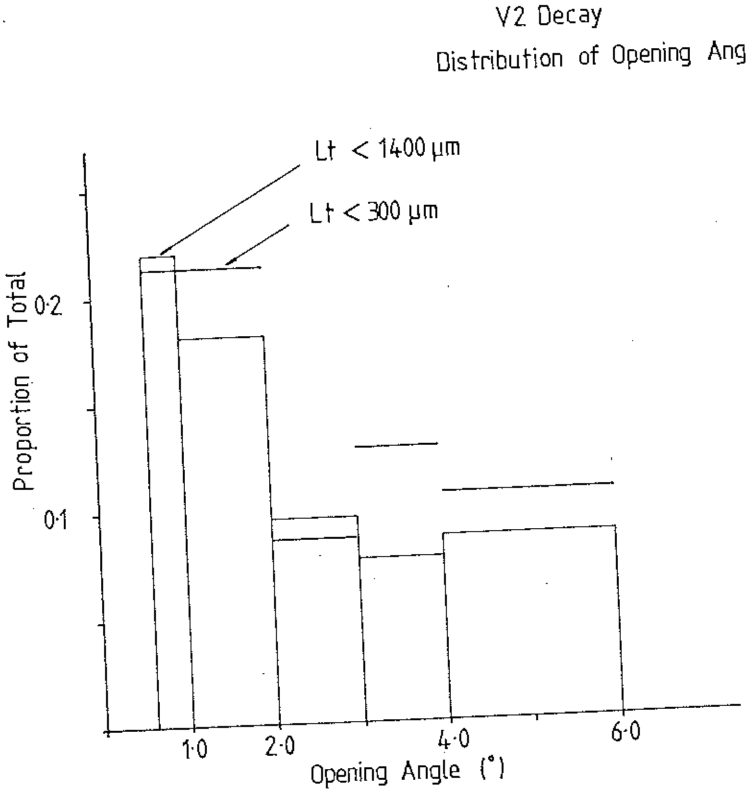

Figure 6.10 Comparison of K1 and V2 Topologies for Different Lt Cuts

6.5.3.3 Cross Section from the Double Decays

This analysis is due to Williams (1984), and is briefly discussed here for completeness.

Williams took the same data sample as I used, that is excluding all the film, other than Roll 9/10, scanned at CERN. He applied the cuts of table 6.2, and used the sample of frames containing two or more decay topologies. These were assumed to be due to associated charm production.

Williams subtracted the background in this sample as follows. If one assumes that all the single decay candidates are due to non-charmed decays and interactions, then the number of double and triple decays expected from random coincidences will be:

E611 $$N_n^2(E - N_n)/2E^2 \qquad \text{Double Decays}$$

$$N_n^3(E - N_n)/6E^3 \qquad \text{Triple Decays}$$

where E is the number of primary interactions in the sample, and N_n is the number of 'noise' singles. Williams tested the validity of equation E611 on interactions found in the region Lt > 1000 microns, Lxy < 30 mm. In a data set containing 2030 primary interactions, 415 secondary interactions were found. In this region there were 32 double interactions and 5 triples. The formulae E611 predict 34 doubles and 2.5 triples.

Some of the single decays are due to charm, the other partner having been missed. Thus the background was recalculated using the following equation:

E612 $$T_t + T_d = C_d + \frac{N_n^2}{2E} + \frac{N_n C_s}{E} + \frac{N_n^2}{6E^2}$$

where

T_d = number of double candidates

T_t = number of triple candidates

C_d = number of charmed doubles detected

C_s = number of charmed singles detected (not in a double)

N_n = number of single decays that are not charm

E = number of primary interactions

Equation E612 must be solved iteratively. The result was that 4.1 of the 12 double candidates were assumed to be due to random coincidences of backround decays.

The cross section was calculated using equation E610, where A was equal to C.V.V∞ . The overall cross section was also multiplied by a further correction factor M.

The factor M accounted for the possibility that some charm decays, which would otherwise have been detected, were missed because the decay was outside the visible chamber volume. M = 1.04

The resulting cross section was

$$\sigma(c\bar{c}) = 13 \pm 8 \quad \mu b$$

Figure 6.11 shows the Lx distribution of the decays in the double candidates used in the above analysis.

Lx Distribution of Decays in Double Candidates
(Williams 1984)

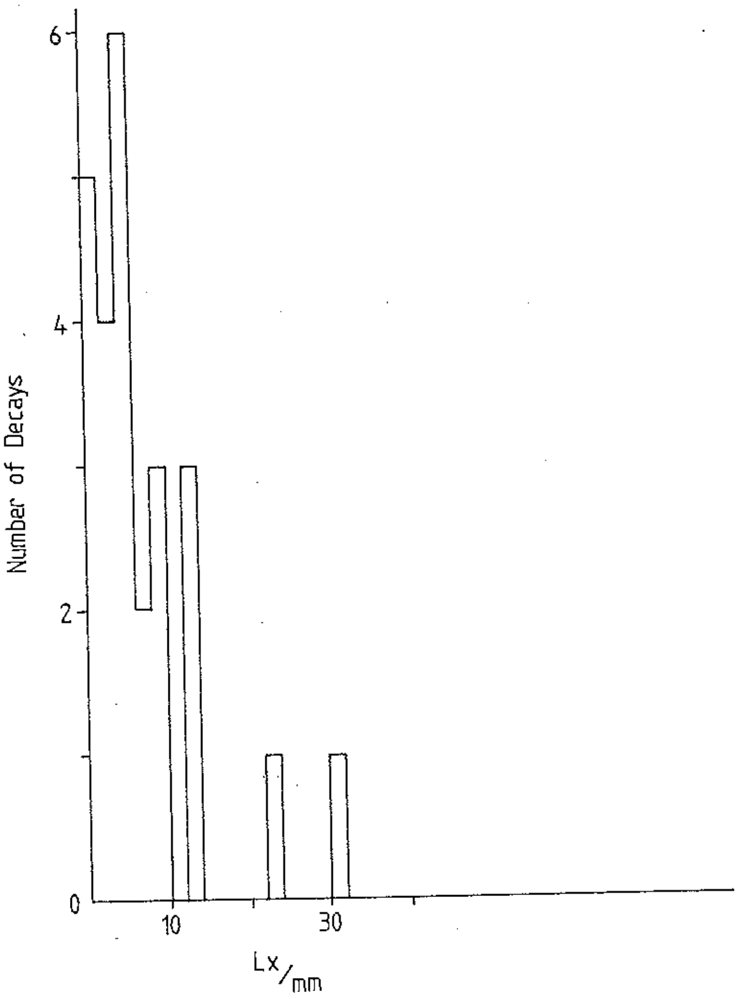

Figure 6.11 Lx Distribution of Decays used in the Doubles Analysis

CHAPTER 7 SUMMARY AND CONCLUSIONS

7.1 Holographic Recording and Film Scanning

7.1.1 HOBC

The Experiment NA25 has shown that a small heavy-liquid bubble chamber can be made to work successfuly with a holographic recording scheme. The initial problems with turbulence and the dissipation of heat from old tracks, which limited the repetition rate to 1Hz (Benichou (1983)), were solved, although the bubble density was halved as a consequence. Had more time been available to modify and test the chamber, bubble densities approaching 150 per centimeter might have been achieved. The pulsed dye laser used for recording and the film transport were entirely successful. An improvement in the quality of the field lens would have allowed 5 micron bubbles to be recorded, which I believe would have increased the visibility of events at small Lx even with no increase in the bubble density. Further improvements to the chamber since the last data taking run have enabled holograms to be taken at a chamber repetition rate of 20 Hz. Using holography in a hydrogen chamber should work very well, as the problem of turbulence due to the heat from old tracks is much reduced as a result of its different thermodynamic properties.

7.1.2 Holographic Film Scanning

The major disadvantage of using holography, from the point of view of the data analysis, was the need to design new types of film scanning machines. Several different approaches were taken and no individual approach emerges as ideal.

The direct projection technique used in the Brussels table has the advantage of simplicity, high resolution and few optical elements to introduce noise into the image. It also allows the scanner to rapidly and sensitively detect kinks and multiple scatters. However this method does require a powerful laser, and in my opinion suffers from problems connected with short and long term safety.

The HOLMES (I) machine at CERN was the prototype for all the other scanning machines. Drevermann demonstrated the need for anamorphic magnification and at least two co-axial views with different magnifications. He also showed the beneficial effects of simlple binary amplitude filtering upon the object. This was of considerable use with the film from the first data taking run, where old large tracks were a considerable problem. The recently completed HOLMES (II) machine incorporates many features that were not available on HOLMES (I), and has overcome some of the limitations of that machine, which were imposed by the original "Spiral Reader" design. HOLMES (II), like the old machine, has a complex optical system with many mirrors and multi-element lenses. I feel that these introduce a noticeable degredation into the image quality, especially with regard to ease of focussing. It was clear from a comparison of the data scanned on the Brussels table and on HOLMES (I) that the focussing error was significantly greater in the data scanned on the HOLMES machine. The use of anamorphic magnification on the high magnification camera may have been responsible in part for this. On CHIMAERA I used anamorphic magnification only on the low magnification view. The use of computer generated graphics has proved to be of considerable value in allowing the rapid and sensitive location of small angle kinks. The CHIMAERA machine has demonstrated the value of simplicity in optical design, showing that a high quality image can be obtained with few lenses if the individual elements are of the highest quality and anti-reflection coated. Data scanned on CHIMAERA has a similar error in Z to data scanned on the Brussels table The choice of a suitable camera tube for the high-magnification camera required the testing,under scanning conditions, of various types of image tube, the final choice was solved by the choice of a silicon target vidicon. The uniform and low dark current of this tube contributed significantly to the image quality. It was found that the fixed sensitivity was not a problem, probably in part due to the large dynamic range of the tube. Lack of time has prevented any proper testing of the rotating Dove prism kink detection idea. All the neccessary electronics to drive the stepping motor prism rotator have been designed and built, and a preliminary test has shown that the high-magnification image does not deteriorate when the prism is in the optical system. I intend to use the Dove prism in the scanning of the 200 GeV film.

The problems of focussing accurately came initially as something of a surprise to the collaboration. I have shown in this thesis that the use of in-line holography inevitably leads to a three dimensional image structure of a bubble which changes slowly in depth. Edge enhancement by spatial filtering (high-pass or differentiation) may be a useful technique resulting in a reduction in focussing errors, but limited tests have not proved conclusive. I have investigated the possibility of assisted focussing, using an oscilloscope to display the video line running through the centre of the bubble. Focussing so that the initial amplitude slope at the bubble edge is largest has proved to be repeatable, and more tests will be carried out in the near future. In general focussing for maximum edge "sharpness" has proved to be the most consistent approach.

The collaboration has shown that it is possible to scan and measure holograms in a way that is not significantly different from conventional scanning, other than in the machines used. The average scanning times (one scan) on CHIMAERA for 360 GeV/c film were:

Frames with a primary interaction: 20'/frame
Frames with no primary interaction: 3'/frame

7.2 Charm Production Cross Section

7.2.1 Comparison of Inclusive and $D\overline{D}$ Cross Sections

The inclusive cross section as determined in chapter 6 section 6.5, is higher than the $D\overline{D}$ cross section determined by Williams (1984). I attribute this difference to $\Lambda_c^+\ \overline{D}$ production, where most of the Λ_c^+ decays will be missed due to their short lifetime (2.3×10^{-13}s). Thus these associated decays will contribute little to the cross section determined from the double decays. My analysis technique uses single decays, and the short Λ_c^+ lifetime will not affect the probability of detecting the D meson partner. This will result in the cross section determined from the single decays being higher than twice the cross section determined from the double decay sample. The experiment NA16 calculated a $\Lambda_c^+\ \overline{D}$ cross section of 8 microbarns. Further analysis of the NA25 single decay data may allow an estimate of the fraction of the $\Lambda_c^+\ \overline{D}$ production in the total charm production cross section.

7.2.2 Comparison with other Determinations

Figure 7.1 compares the two NA25 cross sections with some of the recently measured charm production cross sections at similar energies. The CHARM collaboration and BEBC measurements which are only valid for $x_F > 0.5$ have been omitted. It can be seen that the cross section calculated from the double decay sample (Williams (1984)) agrees with the NA18, CCFRS, LEBC and FFMOW results. The NA25 double decay cross section may include a small fraction of the $\Lambda_c^+\ \overline{D}$ cross section but this will be small because of the short Λ_c^+ lifetime, and the reduced experimental acceptence for these events. The total charm cross section calculated in this thesis is comparable with the LEBC result, and is higher than the double decay cross section as expected. A strict comparison between the

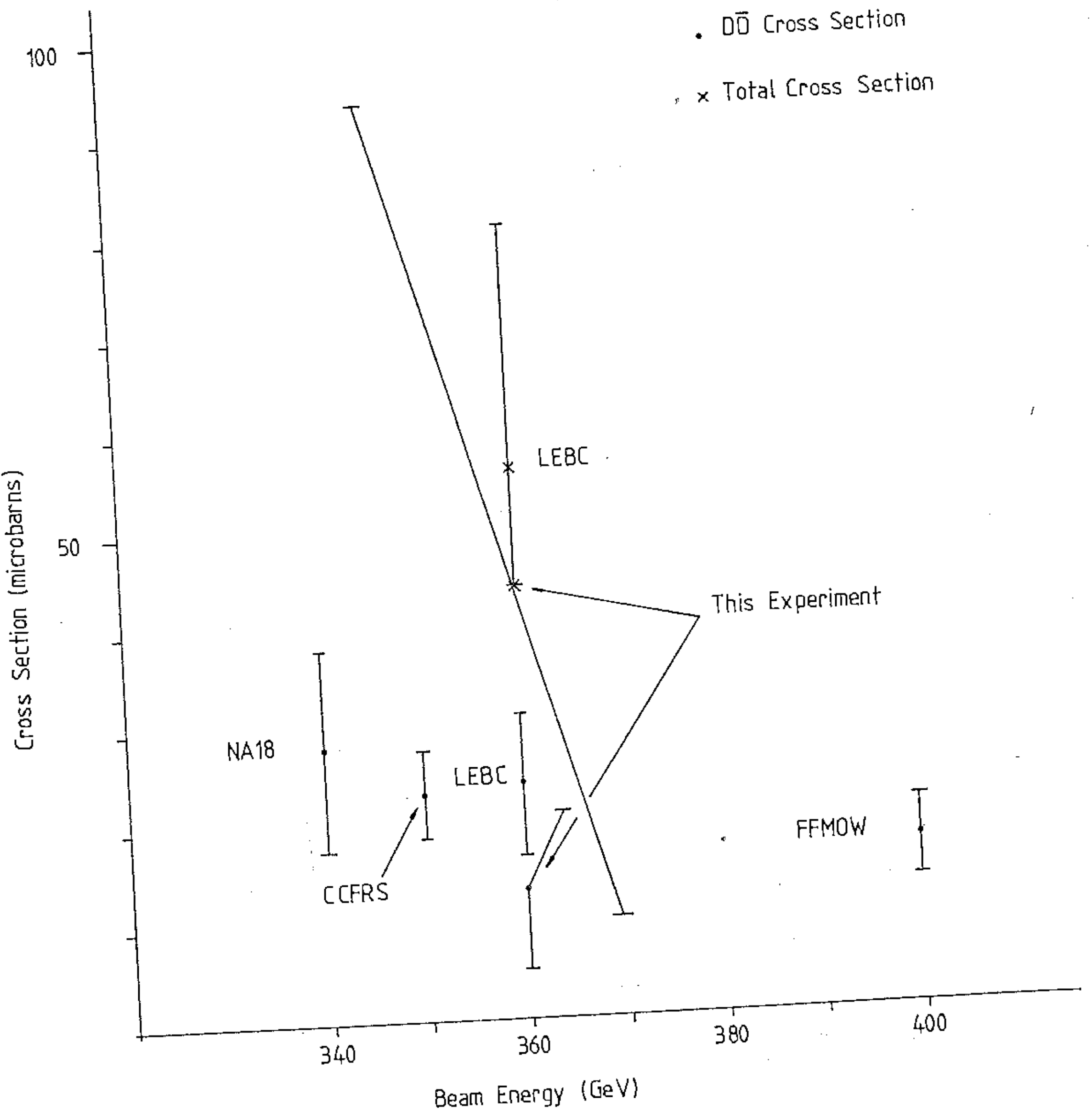

Figure 7.1 A Comparison of Charm Production Cross Sections

experiments in figure 7.1 is difficult due to the variety of techniques used. The LEBC and NA18 experiments both used high resolution bubble chambers with conventional photography. The NA18 experiment used the BIBC chamber filled with the same freon as we used in HOBC, and the two cross sections are comparable. The use of a muon trigger in NA25 also complicates direct comparisons.

The large errors (1-unit support values) on the cross section determined from the single decays are heavily influenced by the data in the region Lx < 2 mm, where the effect of the uncertainty in β is greatest. A calculation of the cross section for Lx > 2mm might have smaller relative errors, but a further Monte Carlo dependent correction would have to be made. The visibility correction is the major source of error in the analysis of the NA25 data. If the time were available, random in-time interactions that had not given a muon trigger could be scanned and measured. These frames would contain essentially no charm decays, but in all other respects they would be identical to the triggered frames. The Lx distribution of the decays topologies, assumed to be due entirely to "noise" decays and therefore flat, would allow a direct determination of the visibility function, independent of the Monte Carlo simulation.

7.3 Future Developments

The film scanning and data analysis of the 360 GeV film is now almost complete. The statistical significance of the cross section will be slightly improved by the addition of a further 2000 frames that were not available for this analysis. It is unclear if we will be able to make any use of the film scanned at CERN for reasons explained in chapter 6. By the end of 1984 sufficient 200 GeV film will have been analysed to allow a calculation of the charm production cross section at this energy. The ratio of cross sections at 360 and 200 GeV will be more accurately determined than either cross section individually due to the cancellation of some systematic errors. This ratio should allow some discrimination between the various production models discussed in chapter 1.

The CHIMAERA scanning machine will have the rotating Dove prism installed, and this will allow me to evaluate its effectiveness as a kink detector using the 200 GeV film.

The outlook for HOBC and holographic bubble chambers in general is bleak. The financial constraints on High Energy Physics in Europe have lead to the closing down of all the large chambers, and the current emphasis on colliding beam experiments has left little beam time or money for fixed target experiments. HOBC could be used successfully with a down stream spectrometer, allowing a considerable reduction in the background in a charmed particle experiment High resolution holographic bubble chambers could also be used in other experiments, especially in low energy experiments using strange particles, for example K^-p experiments below 200 MeV/c.

APPENDIX A NA25 SCAN RULES

A systematic set of scan rules was drawn up for the collaboration by O.R.Williams of UCL. These are a set of rules allowing all of the data neccessary to reconstruct the secondary decays and interactions of interest to be collected.

Each roll of film was scanned twice independently, a third scan (SCAN 3) resolved the differences between the first two scans. A fourth (SCAN 4) scan of interesting decay topologies was carried out on frames selected after cuts had been applied to the data. By collaboration agreement Brussels will carry out the fourth scan of the films scanned at all labs other than CERN.

To reduce the scanning load only frames possessing a good muon and a unique set of predictions were scanned. About 10% of all the frames had missing or multiple prediction coordinates.

A.1 Scanning Procedure

Each frame carried the measured positions of at least four fiducials. The set had to include F22 and F32, and should include F2 and F23. At UCL the fiducial F12 was also measured. The frame was then scanned in the X-axis direction alone, starting from the predicted beam track position in Y and Z. If a primary interaction was found the beam track carried the code "F". If no primary interaction was found the appropriate code was added to the beam track (see section A.2). If a single primary interaction compatible with the prediction was found then all the secondary decays and interactions were measured. Any tertiary activity arising from a secondary decay was also measured.

A.2 Topologies of Primary Interactions

1) Beam track leading to an interaction. (Beam code F)

In this case one of two codes are attached to the measured vertex position.

a) If the vertex is scannable, more than 10mm from the end of the film, and the number of tracks coming from the vertex is 30 or less then the code "Bnn" is given, where nn is the number of tracks.

b) In other cases the code "Ynn" is used and the frame is not scanned for secondary activities.

2) Beam track Missing or not Interacting

Code = "P"
A beam track corresponding to the prediction has been found but it left the chamber without interacting.

Code = "W"
An upstream (window) interaction has been found

Code = "D"
The predicted beam track postion lies outside the chamber

Code = "R"
Nothing on the frame corresponds to the prediction

Code = "Z"
The whole frame is unscannable or full of tracks

A.3 Topologies of Secondary Activities

a) Decay Topologies

A secondary vertex is identified as a decay if all the tracks arising from it are minimum ionising and forward going. Charged decays are given the code "Knn" where nn is the number of tracks arising from the decay, neutral decays are given the code "Vnn". Decays which topologically must be interactions, such as V3 or K4 are included. If the decay vertex is obscured, such that the nature of the particle leading to the decay cannot be determined, the decay is given the code "Xnn".

b) Gamma Conversion Topologies

A vertex is assigned the code "G1" or "G2" if it is judged to be a gamma conversion. If both tracks are visible and either show signs of multiple scattering the decay is called "G2". If the opening angle is zero, thus the track appears doubly ionising, it is given the code "G1".

c) Interaction Topologies

A secondary vertex is identified as an interaction if any of the tracks are more than minimum ionising or are backward going. A charged interaction is given the code "Imn" and a neutral interaction the code "Nmn". The integer m is the number of heavily ionising or backward going tracks, and the integer n is the number of forward going tracks that are minimum ionising. If m > 9 then it is recorded as 9. If the vertex is obscured, but it is clearly not a decay due to the presence of backward or heavily ionising tracks, the code "Amn" is used, with m,n as before.

Figure A.1 shows idealised examples of primary and secondary vertices

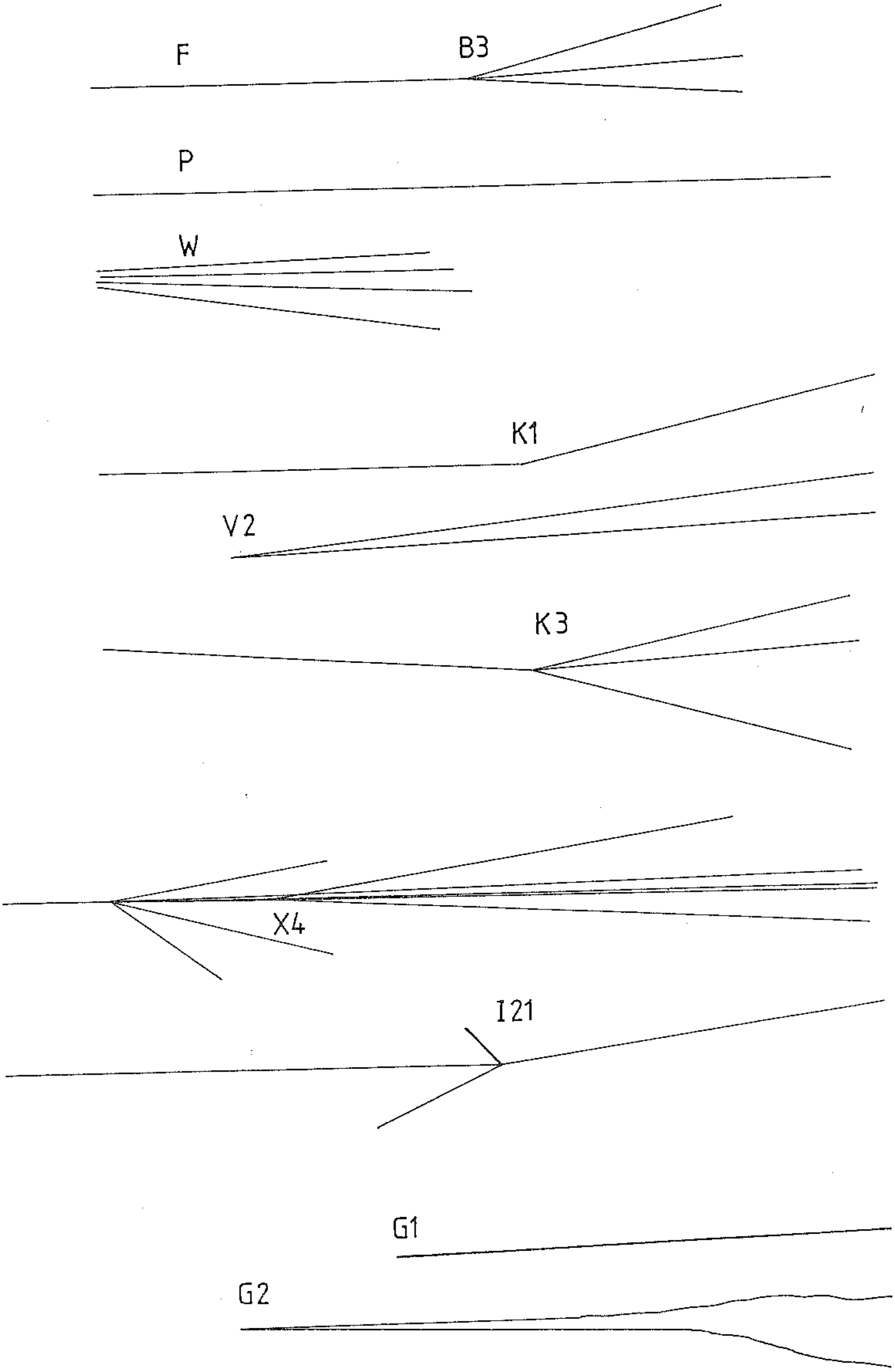

Figure A.1 Illustrative Examples of Primary and Secondary Topologies

LIST OF REFERENCES

Abe K. et al., Phys.Rev. D30, 1 (1984)

Adamovich M.I. et al., Phys.Lett., 140B, 119 (1984)

Adamovich M.I. et al., Phys.Lett., 140B, 123 (1984)

Aguilar-Benitez M. et al., Phys.Lett., 122B, 312 (1983)

Albini E. et al., Phys.Lett., 110B, 339 (1982)

Anelli E.F. et al., Rev.Sci.Instrum., 49, 1054 (1978)

Barger V., Halzen F., Keung W.Y., Phys.Rev., D25, 112 (1979)

Barth M. et al., IIHE-83.11 (1983)

Bedertscher A. et al., Phys.Lett., 123B, 471 (1983)

Bellini G., CERN-EP/84-69 (1984)

Belz R.A., Shofner F.M., Appl.Opt., 11, 2215 (1972)

Benichou J.L. et al., Nucl.Instr. and Meth., 214, 245 (1983)

Beuselinck R. et al., Nucl.Instr. and Meth., 154, 445 (1978)

Blankenbeckler R., Brodsky S.J., Phys.Rev., D10, 2973 (1974)

Bjorken J.D., Drell S.D., Relativistic Quantum Mechanics, McGraw-Hill, New York, 1964

Boret C., Milner S., Placci A., CERN/Lab II/EA/74-4 Rev.ed. (1975)

Born M., Wolf E., Principles of Optics, 6th ed., Pergamon Press, Oxford, 1980

Bourquin M., Gaillard J.-M., Phys.Lett., 59B, 191 (1975)

Bourquin M., Gaillard J.-M., Nucl.Phys. B114, 334 (1976)

Brand C. et al., Nucl.Instr. and Meth., 136, 485 (1976)

Brodsky S.J. et al., Phys.Rev., D23, 2745 (1981)

Carrol A. et al., Phys.Lett., 80B, 319 (1979)

Champagne E.B., J.Opt.Soc.Am., 57, 51 (1967)

Chau L-.L., Phys.Rep., 95, 3 (1982)

Coet P., Doble N., Reucroft S., CERN 82-01, 163 (1982)

Collier R.J., Burkhardt C.B., Lin L.H., Optical Holography, Academic Press, 1971

Combridge B.L., Nucl.Phys., B151, 429 (1979)

DeVelis J.B., Reynolds G.O., Theory and Applications of Holography, Addison-Wesley, 1967

Drevermann H., RL-81-042, Rutherford Appleton Laboratories, Didcot, 1981, p.118

Drevermann H., Geisler K.K., CERN 82-01 (1982)

Dunn P., Thompson B.J., Opt.Engng., 21, 327 (1982)

Dykes M. et al., CERN/EF/EHS/TE 80-4, 1980

Edwards A.F.W., Likelihood, Cambridge University Press, Cambridge, 1972

Gaillard M.K., Lee B.W., Rosner J., Rev.Mod.Phys., 47, 277 (1975)

Goodman J.W., Introduction to Fourier Optics, Mc-Graw Hill, 1968

Gunion J.F., Phys.Lett., 88B, 150 (1979)

Halzen F., Journal Physique, 43(C3 suppl.12), C3-381 (1982)

Hanson G.G., Proceedings of HEP83, Rutherford Appleton Laboratories, England, 1983, p.147

Hutzler P.J.S., Appl.Opt., 16, 2264 (1977)

Kalmus G., Journal Physique, 43(C3 suppl.12), C3-451 (1982)

Kernan A., VanDalen G., Phys.Rep., 106, 299 (1984)

Klanner R., XXII International Conference on High Energy Physics Leipzig, Session A12, July 1984

Lecoq P., Olivier P., CERN/EF/EHS/TE 81-2 (1981)

Lutz J.R., CERN 82-01 (1982)

Maiani L., Journal Physique, 43(C3 suppl.12), C3-631 (1982)

Meier R.W., J.Opt.Soc.Am., 55, 987 (1965)

Muciaccia M.T. et al., XXII International Conference on High Energy Physics Leipzig, Session B10, July 1984

Odorico R., Phys.Lett., 107B, 232 (1981)

Particle Data Group, Rev.Mod.Phys, 56, S1 (1984)

Royer H., RL-81-042, Rutherford Appleton Laboratories, Didcot, 1981, p.80

Schneider H. Proceedings of HEP83, Rutherford Appleton Laboratories, England, p.336, 1983

Sekulin R.L. (ed.), Proceedings of a Meeting on the Application of Holographic Techniques to Bubble Chamber Physics, RL-81-042, Rutherford Appleton Laboratories, Didcot, 1981

Shindler R.H. et al., Phys.Rev., D24, 78 (1981)

Trilling G.H. Phys.Rep., 75, 57, (1981)

Tyler G.A., Thompson B.J., Optica Acta, 23, 685 (1976)

Ushida N. et al., Phys.Rev.Lett., 48, 844 (1982)

Ushida N. et al., Phys.Lett., 121B, 287 (1983)

Ushida N. et al., Phys.Rev.Lett., 51, 2362, (1983)

Vander Lugt A., Proc.I.E.E.E. 62, 1300 (1974)

Williams O.R., 'A Measurement of the Charm Production Cross Section for 360 GeV Protons Incident on Freon using the Holographic Bubble Chamber', Ph.D. dissertation, University of London, 1984

Yourdon E., Constantine L.L., Structured Design, Prentice-Hall, New Jersey, 1979

Yu F.T.S., Introduction to Diffraction, Information Processing, and Holography, MIT Press, 1973

Yura H.T., Appl.Opt., 10, 1154 (1973)

ACKNOWLEDGEMENTS

I am very grateful to my supervisor Dr D.C.Imrie for his advice and encouragement during the course of this research, to my other colleagues in the NA25 Collaboration, especially S.Tavernier, E.Johansson, H.Drevermann R.Cranfield, and especially to O.R.Williams without whom it would have been more difficult and much less fun.

I would also like to thank all the technicians in the Physics Department at UCL who turned my engineering drawings into reality, the film scanners without whom we would have no data, and Mr B.Anderson for his help and advice.

Finally I wish to thank my parents and Justine for all their encouragement, help, and support.

This research was supported by an S.E.R.C. studentship for 3 years.

The text of this thesis was prepared using the "LEX" word processor and printed on a Sanders S/700 Printer.